

Thesis presented to the Instituto Tecnológico de Aeronáutica, in partial fulfillment of the requirements for the degree of Doctor of Science in the Program of Physics, Field of Atomic and Molecular Physics.

**Ivan Guilhon Mitozo Rocha**

**THERMODYNAMICAL, ELECTRONIC, AND  
OPTICAL PROPERTIES OF 2D HEXAGONAL  
DISORDERED SYSTEMS**

Thesis approved in its final version by signatories below:



Prof. Dr. Lara Kühl Teles

Advisor

Prof. Dr. Pedro Teixeira Lacava

Pro-Rector of Graduate Courses

Campo Montenegro  
São José dos Campos, SP - Brazil  
2017

**Cataloging-in Publication Data  
Documentation and Information Division**

Rocha, Ivan Guilhon Mitozo  
Thermodynamical, electronic, and optical properties of 2D hexagonal disordered systems / Ivan  
Guilhon Mitozo Rocha.  
São José dos Campos, 2017.  
147f.

Thesis of Doctor of Science – Course of Physics. Area of Atomic and Molecular Physics –  
Instituto Tecnológico de Aeronáutica, 2017. Advisor: Prof. Dr. Lara Kühl Teles.

1. Semicondutores. 2. Ligas. 3. Teoria do funcional da densidade. I. Instituto Tecnológico de  
Aeronáutica. II. Title.

**BIBLIOGRAPHIC REFERENCE**

ROCHA, Ivan Guilhon Mitozo. **Thermodynamical, electronic, and optical properties of 2D hexagonal disordered systems**. 2017. 147f. Thesis of Doctor of Science – Instituto Tecnológico de Aeronáutica, São José dos Campos.

**CESSION OF RIGHTS**

AUTHOR'S NAME: Ivan Guilhon Mitozo Rocha

PUBLICATION TITLE: Thermodynamical, electronic, and optical properties of 2D hexagonal disordered systems.

PUBLICATION KIND/YEAR: Thesis / 2017

It is granted to Instituto Tecnológico de Aeronáutica permission to reproduce copies of this thesis and to only loan or to sell copies for academic and scientific purposes. The author reserves other publication rights and no part of this thesis can be reproduced without the authorization of the author.

---

Ivan Guilhon Mitozo Rocha  
Av. Eng. Francisco Jose Longo, 622  
12.245-000 – São José dos Campos–SP

# THERMODYNAMICAL, ELECTRONIC, AND OPTICAL PROPERTIES OF 2D HEXAGONAL DISORDERED SYSTEMS

Ivan Guilhon Mitozo Rocha

Thesis Committee Composition:

Prof. Dr. Homero Santiago Maciel	President	-	ITA
Prof. Dr. Lara Kühl Teles	Advisor	-	ITA
Prof. Dr. Francisco Bolivar Correto Machado	Internal Member	-	ITA
Prof. Dr. Lucy Vitoria Credidio Assali	External members	-	USP
Prof. Dr. Cecília de Carvalho Castro e Silva	External members	-	Mackenzie
Prof. Dr. Luiz Fernando de Araújo Ferrão	Internal substitute	-	ITA
Prof. Dr. Adalberto Fazzio	External substitute	-	USP

To all teachers and professors that contributed to my academic formation.

# Acknowledgments

First of all, I would like to thank God for the gift of life and the amazing opportunity to behold and study the nature.

I acknowledge my dear parents, Norma and Fábio, for the tender love, unconditional support, careful attention, dedication, and trust. I would never come so far without you. I hope I can make you proud by honouring all your self-sacrifice and teachings.

I deeply acknowledge my advisor professor Lara K. Teles, for all the teachings since the beginning of college, for the pleasant discussions, advices, laughs and affection. You inspire me to be a good student, teacher and researcher.

I acknowledge professors Friedhelm Bechstedt and Silvana Botti for accepting me as visitor student in Jena, Germany. I am thankful for all discussions, remarkable contributions to my research work and great hospitality.

I acknowledge professors Marcelo Marques, Ronaldo Pelá, and Dr. Jürgen Furthmüller for all the great lessons, fruitful discussions, and teachings during the last years. You all have a significant contributions to my development as a student and researcher.

I acknowledge my work colleagues from ITA and FSU: Daniel Koda, Felipe Freitas, Antônio Marques, Filipe Matusalém, Pedro Bittencourt, Pedro Borlido, Sun Lin, Claudia Rödl, Valerio Armuzza, Christoph Otzen, Wenwen Cui, and Jingming Shi. Thank you all for the pleasant and fruitful (non-)scientific discussions.

I also deeply thank all my entire family and close friends. You have both motivated hardship times and celebrated my victories and achievements with me. You make my life more delightful just for letting me knowing that I can count on you guys.

Finally, I would like to acknowledge CAPES and CNPq agencies for the financial support.

*“Mas a Fama, trombeta de obras tais,  
Lhe deu no Mundo nomes tão estranhos  
De Deuses, Semideuses, Imortais,  
Indigetes, Heróicos e de Magnos.  
Por isso, ó vós que as famas estimais,  
Se quiserdes no mundo ser tamanhos,  
Despertai já do sono do ócio ignavo,  
Que o ânimo, de livre, faz escravo.*

*E ponde na cobiça um freio duro,  
E na ambição também, que indignamente  
Tomais mil vezes, e no torpe e escuro  
Vício da tirania infame e urgente;  
Porque essas honras vãs, esse ouro puro,  
Verdadeiro valor não dão à gente:  
Melhor é merecê-los sem os ter,  
Que possuí-los sem os merecer.”*

— LUIS DE CAMÕES

# Resumo

O estudo de materiais bidimensionais (2D) tem atraído grande atenção tanto da academia como da indústria. Nos últimos anos, a comunidade científica investigou diversos materiais 2D, entre os quais podemos destacar o grupo de materiais semelhantes ao grafeno compostos por elementos da família IV-A, como siliceno e germaneno, ou estruturas de favo de mel feitas de átomos que pertencem a famílias III e V-A, como o nitreto de boro hexagonal, ou mesmo os dicalcogenetos de metais de transição. Uma grande diversidade de comportamentos eletrônicos pode ser observada nesses materiais e novos dispositivos baseados neles encontram-se em fase de desenvolvimento.

Pode-se produzir materiais com propriedades ajustadas para otimizar o desempenho de novos dispositivos. As ligas semicondutoras tridimensionais (3D) foram amplamente aplicadas nesse sentido como forma de obter *bandgaps* de energia ajustáveis, o que é conhecido como engenharia de *bandgap*. Da mesma forma, o uso de ligas de materiais 2D poderia aumentar o potencial de aplicações destes materiais, oferecendo a possibilidade de modulação de suas propriedades eletrônicas. Contudo, sob certas condições as ligas podem sofrer efeitos de separação de fase, levando a diferentes propriedades eletrônicas e ópticas. Dessa forma, o estudo de ligas semicondutoras 2D e de sua estabilidade termodinâmica é de grande valia. Neste trabalho, realizamos importantes estudos pioneiros sobre as propriedades estruturais, eletrônicas, ópticas e termodinâmicas das ligas binárias com base em elementos da família IV-A, bem como da liga feita de grafeno e nitreto de boro hexagonal. Exploramos também a possibilidade de ajuste das propriedades de materiais 2D através de funcionalização parcial da folha de grafeno com grupos adsorventes, como no caso do óxido de grafeno.

Para realizar essas investigações, combinamos os cálculos *ab initio* baseados na teoria funcional da densidade com uma abordagem estatística baseada em uma expansão de *clusters*, conhecida como aproximação quase-química generalizada (GQCA, do inglês *Generalized Quasi-Chemical Approximation*), para levar em conta a desordem estrutural e química do sistema. Propomos ainda um método de cálculo da entropia que não requer argumentos combinatórios e permite que a aplicação da GQCA para camadas atômicas funcionalizadas.

O comportamento das propriedades físicas dos materiais estudados, tais como *gaps* de energia, é descrito como uma função de suas composições químicas médias e das condições de crescimento. Quando disponível, comparamos as previsões do nosso modelo com os resultados experimentais disponíveis. Diferentes condições de estabilidade termodinâmica foram verificadas em cada um desses sistemas e suas consequências para as suas respectivas propriedades físicas são entendidas à luz de efeitos de flutuação da composição e separação de fases.

# Abstract

The study of two-dimensional (2D) materials have attracted great attention from academia and industry. In recent years, the scientific community has investigated several 2D materials, among which we can highlight graphene-like materials made of IV-A family elements, like silicene and germanene, or honeycomb structures made of atoms that belongs to III-A and V-A families, like the hexagonal boron nitride, or even the transition metal dichalcogenides (TMDC). A big diversity of electronic behaviors can be observed and novel devices based on these novel materials are being developed.

One may produce materials with tailored properties to optimize the performance of new devices. Three-dimensional (3D) semiconducting alloys have been widely applied as a way to tune the energy band gaps, which is known as bandgap engineering. Similarly, the use of 2D materials alloys may expand application possibilities of these materials by allowing property modulation. However, under certain conditions the alloys may experience phase separation effects, leading to different electronic and optical properties. In this way, the study of 2D semiconductor alloys and their thermodynamical stability owns a great value. In this work we performed important and pioneers studies on the structural, electronic, optical and thermodynamic properties of binary alloys based on IV-A family elements, as well as the alloy made from graphene and hexagonal boron nitride. We also explored tailoring of 2D materials properties by partial functionalization of the graphene sheet with adsorbent groups, as in case of graphene oxide.

To perform these investigations, we combine *ab initio* calculations based on density functional theory (DFT) with a statistical approach based on a cluster expansion, known as generalized quasi-chemical approximation (GQCA), to account for the system structural and chemical disorder. We proposed an approach to entropy calculation that does not require combinatoric arguments and enables the GQCA application to functionalized sheets.

The behavior of the physical properties of these materials, such as energy gap, is described as a function of their average compositions and growth conditions. When available, experimental results are compared with our model predictions. Different thermodynamic stability conditions have been verified in each one of these systems and their consequences

on the alloy physical properties are understood in the light of composition fluctuation and phase separation effects.

# List of Figures

FIGURE 1.1 – Planar honeycomb structure of graphene. . . . .	26
FIGURE 2.1 – Flowchart of the algorithm used in the self-consistent solution of the Kohn-Sham equations. . . . .	38
FIGURE 2.2 – Half occupation scheme of DFT-1/2 considering self energy corrections on valence and conduction bands. Half electron is removed from VBM, while half electron is added to CBM, to corrections on electronic affinity and ionization energy, respectively. . . . .	43
FIGURE 2.3 – Mixing excess energy of an alloy calculated at an arbitrary temperature. The concentrations $x_1$ and $x_2$ are determined by the common tangent method and the $x'_1$ and $x'_2$ are calculated by the change of curve concavity. . . . .	53
FIGURE 2.4 – Arbitrary example of $T$ - $x$ phase diagram. The stable, metastable, and instable regions are represented by the white, grey, and red colors, respectively. . . . .	54
FIGURE 3.1 – Eight-atom supercell considered in the calculation. The atomic sites are labelled by 1,2,3,4,5,6,7,8. . . . .	65
FIGURE 3.2 – Plot of the excess energies (2.75) of each $\text{Si}_{8-n_j}\text{C}_{n_j}$ (a), $\text{Ge}_{8-n_j}\text{Si}_{n_j}$ (b) and $\text{Ge}_{8-n_j}\text{C}_{n_j}$ (c) configuration. In addition, the tie line representing the internal energy $\Delta\varepsilon_j$ of $\text{Si}_{1-x}\text{C}_x$ at $T = 0$ K, calculated through 2.75, is shown as function of the concentration $x$ . The inset figure corresponds to configuration 11, i.e. $sp^2$ -bonded SiC. . . . .	68
FIGURE 3.3 – (a) The probabilities $x_j$ of all $\text{Si}_{n_j}\text{C}_{8-n_j}$ configurations versus temperature at $x = 0.50$ . Configurations 1, 6, 11 and 22 are highlighted. (b) Degree of ordering in $\text{Si}_{1-x}\text{C}_x$ for $x = 0.5$ , quantified as SRO parameter $L$ , as a function of temperature. . . . .	69

- FIGURE 3.4 – The  $T$ - $x$  phase diagram of (a)  $\text{Ge}_{1-x}\text{C}_x$ (black) and (b)  $\text{Si}_{1-x}\text{Ge}_x$ (red). Solid lines: binodal curves; dashed lines: spinodal curves. . . . . 70
- FIGURE 3.5 – The lattice parameter as a function of the composition for  $\text{Ge}_{1-x}\text{C}_x$ (black),  $\text{Si}_{1-x}\text{Ge}_x$ (red) and  $\text{Si}_{1-x}\text{C}_x$ (blue). The symbols represent the lattices parameters of an individual cluster configuration with the corresponding composition. . . . . 72
- FIGURE 3.6 – The mean first-nearest neighbor distance of  $\text{Ge}_{1-x}\text{C}_x$ (black),  $\text{Si}_{1-x}\text{Ge}_x$ (red) and  $\text{Si}_{1-x}\text{C}_x$ (blue) as a function of the composition with respective mean values associated with the configuration in each cluster class. The  $A-A$ ,  $A-B$ , and  $B-B$  bond lengths are shown with triangles, circles and squares, respectively. . . . . 73
- FIGURE 3.7 – Perspective views on (a)  $\text{Ge}_4\text{C}_4$  (configuration  $j = 14$ ), (b)  $\text{Si}_6\text{C}_2$  (configuration  $j = 20$ ), (c)  $\text{Si}_4\text{Ge}_4$  (configuration  $j = 11$ ), and (d)  $\text{Si}_4\text{C}_4$  (configuration  $j = 11$ ). C (Si, Ge) atoms are presented as brown (bright blue, dark blue) dots. . . . . 74
- FIGURE 3.8 – Buckling amplitude of an arbitrary configuration. . . . . 75
- FIGURE 3.9 – Averaged buckling amplitude of  $\text{Ge}_{1-x}\text{C}_x$ (black),  $\text{Si}_{1-x}\text{Ge}_x$ (red) and  $\text{Si}_{1-x}\text{C}_x$ (blue) as a function of the composition. The red diamonds represent previously reported results for  $\text{Si}_{1-x}\text{Ge}_x$  alloys within SQS methodology (PADILHA *et al.*, 2013). . . . . 75
- FIGURE 3.10 – The gap curves of random alloys of  $\text{Ge}_{1-x}\text{C}_x$  (black),  $\text{Si}_{1-x}\text{Ge}_x$  (red) and  $\text{Si}_{1-x}\text{C}_x$  (blue) as a function of the composition for  $T = 800\text{K}$ . Full line (dashed) curves correspond to results obtained within the GGA-1/2 (GGA) approach. . . . . 79
- FIGURE 3.11 – (a) The gap curves of  $\text{Si}_{1-x}\text{C}_x$  for different temperatures. The black line corresponds to ordered phase 11. (b) The maximum energy gap obtained for the  $\text{Si}_{1-x}\text{C}_x$  alloy as a function of the growth temperature. The full line represent the best fit of the data using Eq. (3.6). . . . . 82
- FIGURE 4.1 – An example of a 2D periodic system derived from one supercell configuration. B, C and N atoms are represented as green, brown and gray dots, respectively. Each configuration is labelled according to the represented numeration. The represented configuration is labelled as BCCCN CB following the order of the atoms that stay in the 12345678 sites, respectively. . . . . 85

- FIGURE 4.2 – (Color online) Excess energies  $\Delta\varepsilon_j$  of each atomic configuration as function of the number of carbon atoms  $n_j$ . The black diamonds represent the configurations with mainly B-B and N-N bonds, while the light blue diamonds represent the complementary subset of the possible configurations. . . . . 87
- FIGURE 4.3 – The  $T$ - $x$  phase diagram of  $(\text{BN})_{1-x}(\text{C}_2)_x$ . The binodal (spinodal) curve is represented by the full (dashed) line. . . . . 87
- FIGURE 4.4 – The probability histogram of all cluster configuration classes of  $(\text{BN})_{1-x}(\text{C}_2)_x$  alloy with  $x=0.5$  at 800 K (a), 1600 K (b) and 5200 K (c) within GQCA formalism. Histogram obtained from a random alloy, more precisely an ideal solid solution, is depicted in (d). The black bars represent the configurations with B-B and N-N bonds, while the light blue bars represent the complementary configuration subset S. . . . . 88
- FIGURE 4.5 – Kullback-Leibler divergence between the random alloy and GQCA probability distributions as a function of temperature for different compositions  $x=0.25, 0.5,$  and  $0.75$ . Small divergence values indicate similar probability distributions. Adopted growth temperature  $T$  for alloy property estimations and critical temperature  $T_c$  are highlighted. 89
- FIGURE 4.6 – The lattice parameter as a function of the carbon concentration for the  $(\text{BN})_{1-x}(\text{C}_2)_x$ . The black diamonds represent the configurations with B-B and N-N bonds, while the light blue ones represent the complementary configuration subset S. These calculations considered the growth temperature  $T=1600$  K. . . . . 90
- FIGURE 4.7 – Cluster configurations CBBNBNCN (a) and BBBNBNNN (b) of  $(\text{BN})_{1-x}(\text{C}_2)_x$  alloys are depicted in perspective. A lateral view of configuration CBBNBNCN is provided in (c) and one of BBBNBNNN configuration is provided in (d). . . . . 91
- FIGURE 4.8 – The layer buckling amplitude as a function of the concentration for the  $(\text{BN})_{1-x}(\text{C}_2)_x$ . The black diamonds represent the configurations with B-B and N-N bonds, while the light blue ones represent the complementary configuration subset S. . . . . 92

- FIGURE 4.9 – The energy band gap as a function of the composition for the  $(\text{BN})_{1-x}(\text{C}_2)_x$  alloys obtained with the GGA functional (dotted black curve) and within the HSE06 approach with and without phase decomposition effects (full and dashed blue lines, respectively). The vertical grey shades indicate the  $x$  compositions where the alloy is stable and the horizontal ones corresponds to the energy gap tune range at the stable composition conditions. The black and light blue diamonds represent the energy band gap obtained by GGA and HSE06 calculations for the investigated clusters. Available experimental data are represented by red circles (UDDIN *et al.*, 2014; UDDIN *et al.*, 2015) and squares (CHANG *et al.*, 2013). . . . . 94
- FIGURE 4.10 – Optical absorbance as a function of the wavelength for  $(\text{BN})_{1-x}(\text{C}_2)_x$  alloys with different carbon compositions. The red (black) full line stands for the carbon-rich (BN-rich) phase for comparison with intermediate compositions  $x=0.65$  and  $x=0.84$ , represented by green and blue lines. The absorption spectra predictions are calculated considering local composition fluctuations (a) and complete phase segregation (b). . . . . 95
- FIGURE 5.1 – (a) The atomic sites (carbon-carbon bonds) are labeled with integer numbers from 1 to 8 in black (1 to 12 in white). Sites without oxygen groups are represented as 0, oxygen groups above the graphene layer as ‘u’ and oxygen groups down the graphene layer as ‘d’. The configuration label is obtained by the combination of atomic site labels followed by the carbon-carbon bond ones. (b) An example of a cluster configuration. Carbon, oxygen and hydrogen are respectively illustrated by brown, red and white spheres. According to the labeling system described in (a), the configuration of the represented atomic arrangement is 00ud00ud-d0000u000000. . . . . 99
- FIGURE 5.2 – Illustration of cluster configurations of graphene with a maximum number of oxidant groups: (a)  $n_{\text{OH}} = 8$  alternately bonded hydroxyl groups and (b)  $n_{\text{epo}} = 4$  epoxy groups. Carbon, oxygen and hydrogen atoms are respectively represented by brown, golden and grey spheres. In case that only hydroxyl (epoxy) group adsorption is considered, the configuration label described in Fig. 5.1 can be simplified to 8 sites (12 C-C bonds) label. Consequently, the represented atomic arrangements are (a)  $+ - + - + - + -$ , and (b)  $-0000++0000-$ . . . . . 100

- FIGURE 5.3 – Electronic band structures for fully oxidized cluster configurations ( $x = 1$ ) obtained from HSE06 calculations: (a) carbon sheet completely oxidized with  $-\text{OH}$  groups is described within the  $1 \times 1$  unit cell in order to avoid band folding associated with the use of the  $2 \times 2$  supercell, and (b,c,d) thermodynamically favorable epoxy-oxidized systems studied within  $2 \times 2$  supercells used in the cluster expansion of the disordered system. The valence band maximum (VBM) is chosen as energy reference. . . . . 101
- FIGURE 5.4 – Optical absorbance  $A(\omega)$  of graphene (black curve), and carbon sheets fully decorated with hydroxyl (blue curve) or epoxy (red curve) groups as a function of the incident photon energy. The statistical weights of the different arrangement of configurations with  $n_{\text{epo},j} = 4$  are calculated considering a preparation temperature of  $T = 300$  K. . . . . 103
- FIGURE 5.5 – Excess energies  $\Delta E_j$  of cluster configurations functionalized with hydroxyl groups as function of the number of oxygen groups per cluster  $n_{\text{OH},j}$ . The cluster configurations with  $\Delta E_j < 1.5$  eV/cluster are represented as golden diamonds, while the complementary set is represented in black. . . . . 105
- FIGURE 5.6 – Energetically favored ( $\Delta E_j < 2$  eV) graphene oxide cluster configurations with partial hydroxyl decoration: (a) 000000+-, (b) 00000+--+, (c) 0000+-+-, (d) 000+-+--+, (e) 00+-+--+, and (f) 0+-+--+. The indicated cluster numbering  $j$  refers to Table 5.1. Carbon, oxygen and hydrogen atoms are respectively represented by brown, red and grey spheres. . . . . 106
- FIGURE 5.7 – The  $T$ - $x$  phase diagram of graphene functionalized with hydroxyl groups  $\text{C}_{1-x}(\text{COH})_x$ . The binodal (spinodal) curve is represented by the full (dashed) line. . . . . 107
- FIGURE 5.8 – Electronic band structures for cluster class configurations decorated with an odd number of hydroxyl groups per cluster obtained from spin-polarized PBE calculations. The Fermi energy level is chosen as the reference. One observes that (a) 0000000+ ( $j=2$ ) cluster arrangement exhibit for each different spin channel fully (un)occupied bands, showing an insulating electronic structure; (b) 000+0+0+ ( $j=10$ ) cluster class exhibits half occupied bands, being therefore a metallic atomic arrangement. . . . . 108

- FIGURE 5.9 – Energy gap curve of graphene functionalized with hydroxyl groups as a function of the oxidation level within HSE06 framework. The diamonds represent the HSE06 energy gaps of all the cluster configurations considered, the set of cluster configurations with  $\Delta E_j < 1.5$  eV/cluster are represented as golden diamonds, while the complementary set is represented with black diamonds. Metallic behavior is identified with a zero energy gap. . . . . 109
- FIGURE 5.10 – Average optical absorbance as a function of the photon energy for GO systems decorated with  $-OH$  groups with oxidation levels  $x=0.25$ ,  $0.50$ , and  $0.75$ , represented as red, green and blue curves, respectively. The average spectra are calculated at  $T = 473$  K (full lines) and  $1373$  K (dashed lines). The adsorption spectra predictions are calculated considering only local composition fluctuations, i.e. a homogeneous alloy (a), and complete phase segregation (b). . . . . 110
- FIGURE 5.11 – The most energetically favored ( $\Delta E_j \leq 0.03$  eV) graphene oxide cluster configurations with complete epoxy decoration ( $n_{\text{epo},j} = 4$ ): (a)  $00++00000-0$ , (b)  $00+-00000+-0$ , and (c)  $00+00+0000-$ . The indicated cluster numbering  $j$  refers to Table 5.2. Carbon and oxygen and hydrogen atoms are respectively represented by brown and red spheres. . . . . 112
- FIGURE 5.12 – Excess energies  $\Delta E_j$  of cluster configurations functionalized with hydroxyl groups as function of the number of oxygen groups per cluster  $n_{\text{epo},j}$ . The cluster configurations with  $\Delta E_j < 0.8$  eV/cluster are represented as golden diamonds, while the complementary set is represented in black. . . . . 112
- FIGURE 5.13 – The  $T$ - $x$  phase diagram of graphene functionalized with epoxy groups. The binodal (spinodal) curve is represented by the full (dashed) line. 113
- FIGURE 5.14 – Energy gap curve of graphene functionalized with epoxy groups as a function of the oxidation level within HSE06 framework. The diamonds represent the HSE06 energy gaps of the all the cluster configurations considered, the set of cluster configurations with  $\Delta E_j < 0.8$  eV/cluster are represented as golden diamonds, while the complementary set is represented with black diamonds. Metallic behavior is identified with zero energy gap. . . . . 114

- FIGURE 5.15 –Average optical absorbance as a function of the photon energy for GO systems decorated with  $-O-$  groups with oxidation levels  $x=0.25$ ,  $0.50$  and  $0.75$ , represented as red, green and blue curves, respectively. The average spectra are calculated at  $T = 473$  K (full lines) and  $1373$  K (dashed lines). The adsorption spectra are calculated considering local composition fluctuations, i.e., homogeneous alloys (a), and complete phase segregation (b). . . . . 115
- FIGURE 5.16 –Important cluster configurations representing (a) pristine graphene, (b) COH, (c) 00000000-00ud00000ud0, which corresponds to the most energetically favored cluster fully oxidized by epoxy groups, (d) u0d00d0u-00000ud00000, with  $\Delta E_j = -0.72$  eV/cluster, and (e) d000000d-0000uu0000u0, with  $\Delta E_j = -0.67$  eV/cluster. Carbon, oxygen and hydrogen atoms are respectively represented by brown, red and grey spheres. . . . . 117
- FIGURE 5.17 –The mixing free energy of the understoichiometric GO systems as a function of the average compositions at synthesis temperature of (a)  $200^\circ C$  and (b)  $1100^\circ C$ . . . . . 118
- FIGURE 5.18 –The mixing internal energy  $\Delta U$ , free energy entropic contribution  $-T\Delta S$ , and mixing Helmholtz free energy  $\Delta F$  curves for a fully oxidized system  $(COH)_y(CO_{1/2})_{1-y}$ . The solid lines are obtained for a growth temperature of  $200^\circ C$ , while the dashed lines are for a growth temperature of  $1100^\circ C$ . The zero-energy line is given as a guideline. . . . . 119
- FIGURE 5.19 –The average lattice constant  $a$  of the GO systems calculated within the GQCA approach at synthesis temperature of  $200^\circ C$  as second-nearest neighbor C distances. . . . . 119
- FIGURE 5.20 –The average buckling amplitude  $\Delta$  of the GO systems calculated within the GQCA approach at synthesis temperature of  $200^\circ C$ . . . 120
- FIGURE 5.21 –The average energy gap bowing of the GO systems as a function of the average compositions at growth temperature of (a)  $200^\circ C$  and (b)  $1100^\circ C$ . . . . . 121
- FIGURE 5.22 –The average optical absorbance of fully oxidized GO systems for different  $-O-/-OH$  ratio measured in units  $\pi\alpha$  ( $\alpha$  - fine structure constant), represented curves in different colors. The full lines represent the averages obtained within the GQCA statistical approach considering a growth temperature of  $200^\circ C$ , while the dashed lines have been computed for a growth temperature of  $1100^\circ C$ . . . . . 123

# List of Tables

TABLE 3.1 –	For each different cluster class $j$ it is presented one possible atomic arrangement and degeneracies $g_j$ of 8-atom supercells to study $\text{Si}_{1-x}\text{C}_x$ , $\text{Ge}_{1-x}\text{C}_x$ and $\text{Ge}_{1-x}\text{Si}_x$ binary alloys. Each configuration is labelled according to the numeration represented in figure 3.1. . . . . .	66
TABLE 3.2 –	Excess energy $\Delta\varepsilon_j$ (eV) and statistical contribution $x_j(x = 0.5, T = 800\text{K})$ of the cluster configurations $\text{Ge}_{8-n_j}\text{C}_{n_j}$ , $\text{Si}_{8-n_j}\text{Ge}_{n_j}$ and $\text{Si}_{8-n_j}\text{C}_{n_j}$ . . . . .	67
TABLE 3.3 –	Comparison of mean first-neighbor distances obtained within GQCA and SQS (PADILHA <i>et al.</i> , 2013) (in parenthesis) for $\text{Si}_{1-x}\text{Ge}_x$ alloys at fixed compositions. All values are given in Å. . . . .	73
TABLE 3.4 –	Buckling parameter $\Delta_j$ of the cluster configurations $\text{Ge}_{8-n_j}\text{C}_{n_j}$ , $\text{Si}_{8-n_j}\text{Ge}_{n_j}$ and $\text{Si}_{8-n_j}\text{C}_{n_j}$ . . . . .	76
TABLE 3.5 –	Layer bucklings ( $\Delta$ ) for the 2D $\text{Ge}_{1-x}\text{C}_x$ , $\text{Si}_{1-x}\text{Ge}_x$ and $\text{Si}_{1-x}\text{C}_x$ alloys, considering the cluster statistics ( $x = 0.5$ ) and for the configuration $j = 11$ . Results are compared with literature data shown in parenthesis. References: (SAHIN <i>et al.</i> , 2009) <sup>a</sup> , (ZHOU <i>et al.</i> , 2013) <sup>b</sup> and (PADILHA <i>et al.</i> , 2013) <sup>c</sup> . . . . .	77
TABLE 3.6 –	Energy gap $E_{g,j}$ of the cluster configurations $\text{Ge}_{8-n_j}\text{C}_{n_j}$ , $\text{Si}_{8-n_j}\text{Ge}_{n_j}$ and $\text{Si}_{8-n_j}\text{C}_{n_j}$ . Metallic configurations are indicated by ‘metal’. . . . .	78
TABLE 3.7 –	Energy gaps ( $E_g$ ) for the 2D $\text{Ge}_{1-x}\text{C}_x$ , $\text{Si}_{1-x}\text{Ge}_x$ and $\text{Si}_{1-x}\text{C}_x$ alloys, considering the cluster statistics ( $x = 0.5$ ), and for the configuration $j = 11$ . The values with the symbol † were calculated considering gap corrections. The DFT-1/2 self-energy corrections for alloy statistics were obtained with transferability arguments, while the results for the ordered configurations ( $j = 11$ ) were optimized for these specific arrangements. . . . .	80
TABLE 4.1 –	$(\text{BN})_{1-x}(\text{C}_2)_x$ non-equivalent cluster classes and their degeneracies $g_j$ . The numeration of sites for cluster labelling is depicted in Fig. 4.1. . . . .	85

TABLE 4.2 – Excess energy $\Delta\varepsilon_j$ (eV) and statistical contribution $x_j$ ( $x = 0.5, T = 1600K$ ) of the cluster configurations of the $C_x(\text{BN})_{1-x}$ alloy. . . . .	86
TABLE 4.3 – Layer buckling $\Delta_j$ and lattice constant $a_j$ of each cluster configuration class $j$ of the $C_x(\text{BN})_{1-x}$ alloy. . . . .	90
TABLE 4.4 – Energy gap $E_g$ of the cluster configurations of $C_x(\text{BN})_{1-x}$ alloys in eV. GGA calculations are performed for all configurations, while HSE06 hybrid functional is only considered for the statistically most relevant ones. . . . .	93
TABLE 5.1 – Cluster classes $j$ , their labels, their degeneracies $g_j$ , numbers of hydroxyl groups per cluster $n_{\text{OH},j}$ , excess energies $E_j$ per cluster, and fundamental energy gaps from PBE ( $E_{g,j}^{PBE}$ ) and HSE06 calculations ( $E_{g,j}^{HSE}$ ). Metallic configurations are indicated by ‘Metal’. . . . .	104
TABLE 5.2 – Cluster classes $j$ , their labels, their degeneracies $g_j$ , numbers of epoxy groups per cluster $n_{\text{epo},j}$ , excess energies $\Delta E_j$ per cluster and fundamental energy gaps from PBE ( $E_{g,j}^{PBE}$ ) and HSE06 calculations ( $E_{g,j}^{HSE}$ ). . . . .	111
TABLE 5.3 – Fitting parameters for gap bowing $\Delta E_g(y, z, T)$ as defined in Eq.5.3 for different growth temperatures. The average fitting error $\bar{e}$ is given for each temperature. Parameters for intermediate temperatures can be estimated by interpolation. . . . .	123

# List of Abbreviations and Acronyms

2D	Two-dimensional
3D	Three-dimensional
TMD	Transition Metal Dichalcogenides
QCA	Quasi-Chemical Approximation
GQCA	Generalized Quasi-Chemical Approximation
DFT	Density Functional Theory
PAW	Projector Augmented Waves
HF	Hartree-Fock
KS	Kohn-Sham
LDA	Local Density Approximation
GGA	Generalized Gradient Approximation
PBE	Perdew-Burke-Ernzerhof
HSE	Heyd-Scuseria-Ernzerhof
CVD	Chemical Vapor Deposition
VASP	Vienna Ab-initio Package
DOS	Density of States
KL	Kullback-Leibler
SRO	Short-Range Ordering
SQS	Special Quasirandom Structure
H	Hydrogen
B	Boron
C	Carbon
N	Nitrogen
O	Oxygen
Si	Silicon
S	Sulphide
Ge	Germanium
GO	Graphene Oxide

# List of Symbols

$x$	Concentration of the element B in a $A_{1-x}B_x$ binary alloy
$y$	Concentration of the element A in a $A_{1-x}B_x$ binary alloy, with $y = 1 - x$ .
$T$	System temperature
$P$	System pressure
$H$	System enthalpy
$E$	System internal energy
$V$	System volume
$G$	System Gibbs free energy
$F(x, T)$	Helmholtz free energy of an alloy at a concentration $x$ and temperature $T$
$F_A(T)$	Helmholtz free energy of compound A
$F_B(T)$	Helmholtz free energy of compound B
$\Delta F$	Mixture free energy of $A_{1-x}B_x$ alloy
$\Delta E$	Mixture internal energy of $A_{1-x}B_x$ alloy
$\Delta S$	Mixture entropy of $A_{1-x}B_x$ alloy
$k$	Boltzmann constant
$\Omega$	Number of system configurations
$N$	Number of atoms in the system
$N_A$	Number of atoms A in the system
$N_B$	Number of atoms B in the system
$M$	Total number of clusters
$J$	Number of possible cluster classes of a cluster expansion
$\Delta\varepsilon_j$	Excess energy of the cluster configuration $j$
$T_c$	Critical temperature
$M_j$	Number of clusters $j$
$x_j$	Occurrence probability of cluster $j$
$g_j$	Degeneracy of cluster $j$
$E_j$	Internal energy of cluster $j$
$q_i$	Electric charge of the $i$ -th particle
$e$	Elementary charge
$\epsilon_o$	Vacuum permissibility

---

$\hat{H}$	Hamiltonian operator
$\hat{T}$	Kinetic energy operator
$\hat{V}_{ee}$	Electron-electron energy operator
$\hbar$	Reduced Planck's constant
$\Psi$	System's exact wavefunction
$\Phi$	Hartree-Fock's wavefunction
$\phi_i$	$i$ -th orbital
$n(\vec{r})$	Electronic charge density
$E_{XC}[n]$	Exchange and correlation functional
$T[n]$	Exact kinetic energy functional
$T_0[n]$	Kinetic energy functional for non-interacting particles
$U_0[n]$	Electrostatic energy functional for non-interacting particles
$V_{ee}[n]$	Electron-electron interaction energy functional
$v_H(\vec{r})$	Hartree potential
$v_{XC}(\vec{r})$	Exchange-correlation potential
$v_{KS}(\vec{r})$	Kohn-Sham potential
$S_i$	Self energy of the $i$ -th orbital
$f_i$	Occupancy of the $i$ -th orbital
$A$	Electronic affinity
$I$	Ionic energy
$E_F$	Fermi's energy
$a$	Lattice parameter
$b$	Bowing parameter
$E_g$	Bandgap energy
$\Delta$	Buckling parameter
$\omega$	Photon angular frequency
$\vec{A}(\vec{r}, y)$	Electromagnetic vector potential
$\vec{E}(\vec{r}, y)$	Electric field
$\vec{B}(\vec{r}, y)$	Magnetic field
$\sigma(\vec{q}, \omega)$	Optical conductivity
$A(\omega)$	Optical absorbance at photon frequency $\omega$
$A_{GQCA}(\omega, x, T)$	Average optical absorbance at photon frequency $\omega$ considering composition fluctuation effects
$A_{PS}(\omega, x, T)$	Average optical absorbance at photon frequency $\omega$ considering phase segregation effects
$L$	Short-range ordering parameter
$P_{A-B}$	robability of occurrence of an A-B bond in an alloyed system
$D_{KL}(x_j    x_j^o)$	Kullback-Leibler divergence between the <i>a posteriori</i> $x_j$ and <i>a priori</i> $x_j^o$ probability distributions

# Contents

1	GENERAL INTRODUCTION . . . . .	26
1.1	Motivation . . . . .	26
1.2	Objective . . . . .	29
1.3	Organization . . . . .	29
2	THEORETICAL BACKGROUND . . . . .	31
2.1	Electronic structure calculation . . . . .	31
2.1.1	Hartree-Fock Method . . . . .	31
2.1.2	Density Functional Theory (DFT) . . . . .	34
2.1.3	Local Density Approximation (LDA) . . . . .	38
2.1.4	Generalized Gradient Approximation (GGA) . . . . .	39
2.1.5	Hybrid Potentials . . . . .	40
2.1.6	DFT-1/2 method . . . . .	42
2.1.7	Bloch Theorem . . . . .	44
2.1.8	Projector Augmented Wave (PAW) method . . . . .	46
2.2	Thermodynamic properties and statistical model for alloyed systems . . . . .	48
2.2.1	Generalized Quasichemical Approximation (GQCA) . . . . .	48
2.2.2	Thermodynamic stability and phase decomposition . . . . .	52
2.2.3	Generalizations concerning ternary alloys . . . . .	54
2.2.4	Generalization of GQCA for 2D functionalized sheets . . . . .	56
2.3	Optical properties . . . . .	60
2.3.1	Layer optical absorbance . . . . .	60

---

2.3.2	Average optical spectra . . . . .	61
2.4	VASP Software and computational details . . . . .	62
3	GROUP IV BINARY ALLOYS . . . . .	64
3.1	Introduction . . . . .	64
3.2	Determination of the equivalence cluster classes . . . . .	65
3.3	Thermodynamic properties . . . . .	66
3.4	Structural Properties . . . . .	71
3.4.1	Lattice parameter $a$ . . . . .	71
3.4.2	First-neighbor distances . . . . .	72
3.4.3	Buckling parameter $\Delta$ . . . . .	74
3.5	Electronic Properties . . . . .	77
4	$(\text{BN})_{1-x}(\text{C}_2)_x$ ALLOY . . . . .	83
4.1	Introduction . . . . .	83
4.2	Cluster expansion and configurational counting . . . . .	84
4.3	Phase stability and composition fluctuation . . . . .	86
4.4	Structural properties . . . . .	89
4.5	Electronic properties . . . . .	91
4.6	Optical properties . . . . .	95
5	GRAPHENE OXIDE . . . . .	97
5.1	Introduction . . . . .	97
5.2	Cluster expansion and configurational counting . . . . .	98
5.3	Fully oxidized sheets . . . . .	99
5.4	Partial hydroxyl oxidation . . . . .	103
5.5	Partial epoxy oxidation . . . . .	111
5.6	Simultaneous oxidation with hydroxyl and epoxy groups . . . . .	115
5.6.1	Thermodynamic stability . . . . .	115
5.6.2	Structural properties . . . . .	118
5.6.3	Electronic and optical properties . . . . .	120

---

6 CONCLUSION . . . . .	124
BIBLIOGRAPHY . . . . .	126
APPENDIX A – GQCA SCALING WITH CLUSTER SIZE . . . . .	141
APPENDIX B – GRAND CANONICAL QUASI CHEMICAL APPROXI- MATION (GRAND-GQCA) . . . . .	143
ANNEX A – PUBLISHED WORKS . . . . .	145
ANNEX B – PARTICIPATION IN SCIENTIFIC CONGRESSES AND CONFERENCES . . . . .	146

# 1 General Introduction

## 1.1 Motivation

The study of two-dimensional (2D) materials is an exciting field that has received a great amount of interest from both academia and industry after the isolation of graphene from graphite through mechanical exfoliation (NOVOSELOV, 2004). The great importance of this achievement gave to Geim and Novoselov the Physics Nobel Prize in 2010 and there were very optimistic expectations that technology would be arriving to an ‘Age of Graphene’ (FLYNN, 2011). This 2D material is formed by a unique atomic layer with  $sp^2$ -hybridized carbon atoms distributed in a planar honeycomb structure, as depicted in Fig.1.1. The world-wide attention has emerged from graphene exceptional mechanical, electronic and thermal properties, which are closely related to the linear energy-momentum dispersion at the Dirac point (ALLEN, 2010).

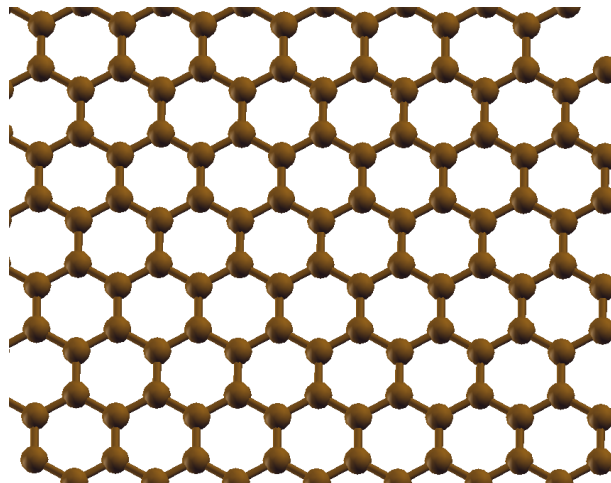


FIGURE 1.1 – Planar honeycomb structure of graphene.

However, large scale high-quality graphene synthesis is a big challenge. The best quality graphene samples are still obtained by mechanical exfoliation, although this process is limited to flakes smaller than  $1mm$  length with unfeasible reproductivity in large scales (ALLEN, 2010; YI; SHEN, 2015). The current more popular solutions to this problem are the chemical vapor deposition (CVD) on transition metals substrates (SUTTER, 2008; REINA,

2009) and chemical exfoliation, which isolate graphene oxide sheets in a graphite sample through Hummers' method.

There are still other obstacles to be surpassed in order to turn possible the generalized graphene application in novel devices. One key feature that makes the use of graphene unlikely in high-performance integrated logic circuits as a planar channel material is the absence of a band gap (NOVOSELOV *et al.*, 2012). Another limitation of its application in electronics is the difficult integration into the current Si-based technology. These facts have triggered the search for other 2D atomically thin crystals, such as monolayers of hexagonal boron nitride (*h*-BN) (PACILE *et al.*, 2008), transition metal dichalcogenides (TMDs) (ROLDAN *et al.*, 2014), such as molybdenum disulfide ( $\text{MoS}_2$ ) (AYARI *et al.*, 2007), and many others materials (SUZUKI; YOKOMIZO, 2010; KOSKI; CUI, 2013; SAHIN *et al.*, 2009; SUZUKI, 2015; ZHANG *et al.*, 2017). There are now a vast variety of materials that make electronic devices entirely based on 2D materials possible (MIRO *et al.*, 2014).

A common feature in devices is the use of three-dimensional (3D) alloys, which allows to vary the band gap between the values of the endcomponents. Considering the 2D group-IV materials, it is natural to try to tailor the electronic properties by alloying the elements with different compositions. This increases the potential to modulate the electronic structures and to widen possible actual applications. Such a concept has been already realized for 2D TMDs. 2D-TMD alloys, such as  $\text{Mo}_{1-x}\text{W}_x\text{S}_2$  (CHEN *et al.*, 2013; RIGOSI *et al.*, 2016),  $\text{Mo}_{1-x}\text{W}_x\text{Se}_2$  (ZHANG *et al.*, 2014),  $\text{MoS}_{2(x)}\text{Se}_{2(1-x)}$  (LI *et al.*, 2014a),  $\text{WS}_{2(x)}\text{Se}_{2(1-x)}$  (DUAN *et al.*, 2016), and  $\text{CoMoS}_2$  (LI *et al.*, 2015) that have been synthesized recently for the study of continuous tunable optical properties. Recently, Wei *et al.* (WEI *et al.*, 2014) discussed the phase stability of mixed single-layer TMDs, showing that the different alloyed TMDs have great distinct stability and electronic structures.

A strong effort has been invested to study graphene-like 2D materials composed of other group-IV elements. It has been demonstrated that 2D sheets of Si and Ge, referred to as silicene and germanene, respectively, exhibit similar properties as graphene, except for a low buckled structure instead of the planar one (CAHANGIROV *et al.*, 2009). The honeycomb structures of binary group-IV compounds  $\text{Si}_{1-x}\text{C}_x$ ,  $\text{Si}_{1-x}\text{Ge}_x$  and  $\text{Ge}_{1-x}\text{C}_x$  have also been reported to have interesting electronic properties. Theoretical predictions showed an energy gap for an ordered configuration of  $\text{Ge}_{0.5}\text{C}_{0.5}$ ,  $\text{Ge}_{0.5}\text{Si}_{0.5}$  and  $\text{Si}_{0.5}\text{C}_{0.5}$  of 3.16 eV, 0.285 eV and 3.53, respectively (SUZUKI; YOKOMIZO, 2010). These predictions indicate that such 2D alloy can exhibit novel properties that are not even a mean value between the correspondent endcomponents, since graphene, silicene and germanene do not exhibit significant energy bandgap values.

Among other several possibilities, hexagonal boron nitride (*h*-BN) is a natural candidate to be combined with graphene in a 2D alloy, since both sheet crystals possess a flat honeycomb structure while the lattice constant mismatch only amounts to 2% (LIU, 2013).

In contrast to graphene, which has no energy gap, *h*-BN is a dielectric with a wide energy band gap of about 6 eV (PACILE *et al.*, 2008) due to the very ionic B-N bond and the broken symmetry between the two sublattices in *h*-BN. Alloying these two 2D materials allows, in principle, a very wide range for changing the energy gap.

Alloying methodologies are not the only possible approach to obtain tunable physical properties through chemical composition control. Due the sensibility of 2D materials to the adsorption of functional groups, oxidation, hydrogenation, and halogenation processes (LOH *et al.*, 2010; PUMERA; WONG, 2013; POH *et al.*, 2013) have been proposed to overcome graphene's zero-gap limitation. These materials can be synthesized through chemical treatment of graphene samples and are natural candidates to chemically tunable graphene-compatible platforms for future applications.

As demonstrated, 2D alloys and functionalized graphene-based materials have a great potential in order to be incorporated inside future electronic and optoelectronic devices based on 2D materials. Reliable simulation approaches beyond the investigation of restricted few "guessed" nonrandom structures (NI *et al.*, 2014; D'SOUZA; MUKHERJEE, 2015; KAN *et al.*, 2011; MAZZONI *et al.*, 2006) or the stoichiometric ordered configurations (SUZUKI; YOKOMIZO, 2010; SAHIN *et al.*, 2009) are demanded to study the non-trivial structural disorder exhibited by these materials. Another important feature that requires further investigation is the influence of composition fluctuation and phase segregation on the alloy properties. Despite the fact that some theoretical approaches have been used only to predict phase separation in such systems (YUGE, 2009; MAZZONI *et al.*, 2006; AZEVEDO, 2006), the exact influence of these effects on the alloy physical properties is still an open question.

There are some important answers that we would like to answer in this work: (i) How can one tune energy band gaps of disordered 2D systems by varying their average chemical compositions? (ii) Would such systems exhibit homogeneous phases or phase decomposition? (iii) How is the influence of phase separation and local composition fluctuations on their physical properties?

A statistical methodology based on generalized quasi-chemical approximation (GQCA) (CHEN; SHER, 1995) has been successfully applied to describe the physical properties of several 3D alloys (MARQUES *et al.*, 2003; TELES *et al.*, 2000; TELES *et al.*, 2001; TELES *et al.*, 2002; PELA *et al.*, 2011). In this work, we present a pioneer, rigorous and systematic theoretical study of 2D alloys and propose its generalization to functionalized sheets, considering several different local atomic configurations and a statistical average to make theoretical predictions about their thermodynamic, structural, electronic and optical properties and how they depend on the system average chemical composition.

## 1.2 Objective

This main goal of this work is to provide theoretical predictions to important 2D disordered systems as first-principles calculations, giving trustworthy information about their structural, thermodynamic, electronic and optical properties based on a statistical approach that accounts for different possible atomic arrangements.

The adopted methodology is easily applicable to other disordered systems and results can be systematic refined by different cluster size choices. Such approach can be a powerful tool in the design of materials with tuned properties by controlling their growth condition and average chemical composition.

## 1.3 Organization

A general introduction is contained in chapter 1, here we discuss the scientific context where this work comes in. We also make a brief review of available literature of the subject and discuss about the possibility of designing an alloy to a specific application on novel devices. The main goals and organization of this work are also explained.

Chapter 2 presents the theoretical background of the used methodology. In this chapter we introduce the Hartree-Fock method to calculate electronic structure, the density functional theory (DFT), and different approximations to the exchange and correlation functionals as well. Different alternatives to improve the description of excited states depending physical properties are presented. At last, we describe the theoretical approach to account the disorder effect within the Generalized Quasi Chemical Approximation (GQCA) and how it can be extended to 2D functionalized sheets.

Chapter 3 is dedicated to show the results obtained for two-dimensional alloys constituted by elements from group IV such as  $\text{Si}_{1-x}\text{C}_x$ ,  $\text{Ge}_{1-x}\text{Si}_x$  and  $\text{Ge}_{1-x}\text{C}_x$ . Our calculations predict very distinct behavior for each alloy,  $\text{Ge}_{1-x}\text{Si}_x$  is characterized for being a random alloy at typical growth temperature and the thermodynamical is expected for the whole composition range,  $\text{Ge}_{1-x}\text{C}_x$  present a completely opposite behavior, having a huge critical temperature and predicting very small solubilities, finally an ordered phase is predicted for  $\text{Si}_{1-x}\text{C}_x$  and it is in agreement with recent experimental findings. We investigated the causes of such distinct behaviors and the role of growth temperature to the ordered phase stability in  $\text{Si}_{1-x}\text{C}_x$ . At last structural and electronic properties are predicted and the influence of thermodynamics on these results is elucidated.

Chapter 4, in its turn, is dedicated to the  $(\text{BN})_{1-x}(\text{C}_2)_x$  2D alloy obtained from graphene and hexagonal boron nitride. This system is studied with a reduced sample set from a ternary alloy made from boron, carbon and nitrogen atoms. The tendency to

phase decomposition verified in experiment is obtained and our predictions for solubilities is consistent with the experimental data. Different scenarios for phase segregation are discussed and the electronic and optical properties that follow from them are described. The statistics considering both the phase separation and the composition fluctuation are applied on calculated absorbance spectra. Experimental results are qualitatively reproduced by our model.

Chapter 5 presents a detailed investigation about graphene oxide under distinct environment conditions applying the GQCA extension to 2D functionalized sheets proposed in chapter 2. Based on experimental findings, we study the effects of adsorption of hydroxyl and epoxy groups on the carbon basal sheet. The effect of simultaneous oxidation of both groups process is studied within an analogous theoretical description to a ternary alloy. The obtained results are compared with experimental data and other theoretical approaches whenever it is possible.

Finally, in Chapter 6 we highlight the most significant methodological contributions from this PhD project to the literature. The most distinctive features of each of the considered 2D systems are also summarized for better comprehension.

In the end we present few appendices and annexes. The appendix A discusses how the GQCA computational cost scales with the choice of cluster size and other parameters. The appendix B contains a generalization of GQCA to the grand-canonical ensemble that naturally arises from the novel formalism proposed in chapter 2. This topic will be further discussed in future works and it is specially interesting to realistic descriptions of 2D functionalized sheets. Finally, annexes A and B respectively present lists of published works in periodic journals and participations in scientific events, where partial results of this PhD project were presented to scientific community.

# 2 Theoretical Background

## 2.1 Electronic structure calculation

The problem of exact electronic structure calculation of a crystal is intrinsically very complicated, since it is an interacting many-body problem. The use of quantum mechanics in this kind of problem is mandatory. However, it is infeasible to solve the Schrödinger equation for all the interacting electrons and nuclei in the solid. Therefore, reasonable simplifications are needed to obtain approximated solutions.

In 1998, the austrian scientist Walter Kohn were laureate with the Chemistry Nobel prize for the development of the Density Functional Theory (NOBEL, 1998), which was extremely important to the simulations of molecules and solids as the available computational power increased in the last decades.

Since *ab initio* computational simulations can provide reliable predictions of different physical properties, expensive synthesis and characterization experiments with different materials can be substituted by such methodologies, saving money and time in the research for new materials with specific desired properties. Another important feature is that the use of this theoretical approach can provide meaningful information of the phenomena studied.

In this section, some different theoretical fundamentals will be discussed, including the ones used in the present work.

### 2.1.1 Hartree-Fock Method

Consider the problem of describing the dynamics of  $N$  electrons, located in  $\vec{r}_1, \dots, \vec{r}_N$  positions, and  $N_z$  nuclei, located in  $\vec{r}_{N+1}, \dots, \vec{r}_{N+N_z}$  positions, distributed in a crystalline structure. All these charged particles interact by Coulombic forces.

Disregarding the spin-component of the complete wavefunction  $\Psi_C(\vec{r}_1, \dots, \vec{r}_{N+N_z})$ , the time-independent Schrödinger equation that describe the stationary states of such system can be written as

$$\begin{aligned}
& - \sum_{i=1}^{N+N_z} \frac{\hbar^2}{2m_i} \nabla_i^2 \Psi_C(\vec{r}_1, \dots, \vec{r}_{N+N_z}) + \sum_{i=1}^{N+N_z} \sum_{j \neq i} \frac{q_i q_j}{4\pi\epsilon_0 |\vec{r}_i - \vec{r}_j|} \Psi_C(\vec{r}_1, \dots, \vec{r}_{N+N_z}) \\
& = E \Psi_C(\vec{r}_1, \dots, \vec{r}_{N+N_z}), \quad (2.1)
\end{aligned}$$

where  $\epsilon_0$  represents the permittivity of vacuum.

Since the nuclei are much heavier than electrons, their dynamics is orders of magnitude slower than the electronic one. Therefore it is possible to deal with the nuclei and electronic dynamics separately. This is called adiabatic or Born-Oppenheimer approximation. In this formalism the interaction between the nuclei and the electrons can be introduced by an external potential  $V_{ext}$  and the number of degrees of freedom of the system decreases from  $3(N + N_z)$  to  $3N$ . The electronic wavefunction  $\Psi(\vec{r}_1, \dots, \vec{r}_N)$  time evolution is given by

$$\begin{aligned}
& - \sum_{i=1}^N \frac{\hbar^2}{2m} \nabla_i^2 \Psi(\vec{r}_1, \dots, \vec{r}_N) + \sum_{i=1}^N \sum_{j \neq i} \frac{e^2}{4\pi\epsilon_0 |\vec{r}_i - \vec{r}_j|} \Psi(\vec{r}_1, \vec{r}_2, \dots, \vec{r}_N) \\
& \quad + \sum_{i=1}^N V_{ext}(\vec{r}_i) \Psi(\vec{r}_1, \dots, \vec{r}_N) = E \Psi(\vec{r}_1, \dots, \vec{r}_N). \quad (2.2)
\end{aligned}$$

In this situation, the electronic Hamiltonian operator  $\hat{H}$  can be identified as

$$\hat{H} = - \sum_{i=1}^N \frac{\hbar^2}{2m} \nabla_i^2 + \sum_{i=1}^N \sum_{j \neq i} \frac{e^2}{4\pi\epsilon_0 |\vec{r}_i - \vec{r}_j|} + \sum_{i=1}^N V_{ext}(\vec{r}_i). \quad (2.3)$$

where one can identify the contribution of the kinetic energy of electrons, the Coulombic electron-electron interaction and the interaction of the nuclei with the electronic distribution terms, respectively. Henceforth, the atomic system of units, where  $\hbar = 1$ ,  $e = 1$ ,  $m = 1$  and  $\epsilon_0 = \frac{1}{4\pi}$ , will be assumed. The equation 2.3 is simplified as

$$\hat{H} = - \sum_{i=1}^N \frac{1}{2} \nabla_i^2 + \sum_{i=1}^N \sum_{j \neq i} \frac{1}{|\vec{r}_i - \vec{r}_j|} + \sum_{i=1}^N V_{ext}(\vec{r}_i). \quad (2.4)$$

We are specially interested in describing the system ground state, which corresponds to the minimal total energy. Approximated solutions to the ground state wave function can be obtained by the variational principle application considering parametrized trial functions.

Due to the electron-electron interaction, we are dealing with a problem of many

interacting particles which may not be separated into multiple independent particle problems nor the exact wave function can be decomposed into a product of orbitals. However, one may ignore this fact and seek to get an approximation of the  $\Psi(\vec{r}_1, \dots, \vec{r}_N)$ . We associate each of the  $N$  electrons with a particular one-particle state  $\phi_i(\vec{r})$  and impose the antisymmetry property of the exact wave function due to the fact that electrons are fermionic particles to its spacial component. The approximated wave function can be written as a Slater determinant

$$\Psi(\vec{r}_1, \dots, \vec{r}_N) = \frac{1}{\sqrt{N!}} \begin{vmatrix} \phi_1(\vec{r}_1) & \dots & \phi_N(\vec{r}_1) \\ \dots & & \dots \\ \phi_1(\vec{r}_N) & \dots & \phi_N(\vec{r}_N) \end{vmatrix}. \quad (2.5)$$

In order to minimize the total energy with respect to the occupied orbitals  $\phi_i(\vec{r})$ , which must fulfill the normalization constraints, one can use the Lagrange multipliers formalism and obtain the following set of equations

$$\frac{\delta}{\delta \phi_i^*} \left[ \langle \hat{H} \rangle - \sum_j \epsilon_j (\langle \phi_i | \phi_i \rangle - 1) \right] = 0, \quad (2.6)$$

which leads to the well known Hartree-Fock (HF) equations

$$\left( -\frac{1}{2} \nabla^2 + V_{ext}(\vec{r}) + V_H(\vec{r}) \right) \phi_i(\vec{r}) + f_{F,i}[\phi_i] = \epsilon_i \phi_i(\vec{r}), \quad (2.7)$$

where  $V_H(\vec{r})$  is the Hartree potential, given by the equation

$$V_H(\vec{r}) = \int \frac{n(\vec{r}')}{|\vec{r}' - \vec{r}|} d^3 r'. \quad (2.8)$$

and the Fock term  $f_{F,i}[\phi_i]$  is given by

$$f_{F,i}[\phi_i] = - \sum_j^N \int \frac{\phi_i(\vec{r}') \phi_j^*(\vec{r}')}{|\vec{r}' - \vec{r}|} \phi_j(\vec{r}) d^3 r'. \quad (2.9)$$

One can interpret equation 2.7 with analogies with classical physical quantities. The operator  $-\frac{1}{2} \nabla^2$  is directly associated with the electron kinetic energy, the external potential is associated with the electron interaction with the periodic distribution with the nuclei disposed in a crystalline structure and the Hartree potential comes as a classic Coulombic interaction. However, the Fock term  $f_{F,i}[\phi_i]$  cannot be associated with any classical physical quantity and represents a pure quantum effect, which is called exchange interaction (PARR, 1989).

Since  $f_{F,i}[\phi_i]$  and  $V_H(\vec{r})$  depend on all orbitals, a self-consistent approach should be used to numerically solve this set of equations. The computational cost involved is extremely high due to the complexity of the term  $f_{F,i}[\phi_i]$ , which is calculated  $N$  times for each interaction step.

### 2.1.2 Density Functional Theory (DFT)

The Hartree-Fock (HF) method and its variants obtain an approximated solution to the problem of electronic structure calculation solving coupled one-body problems subjected to average potentials (FAZZIO, 1995). Each calculated orbital participates in the potential that gives rise to the movement of other electrons. Since one-electron orbitals are considered, it is said that no correlation between different electrons is included in HF method. It is common to define the correlation energy contribution  $E_{cor}$  as the difference between the exact energy  $E$  and Hartree-Fock energy  $E_{HF}$

$$E_{cor} = E - E_{HF}. \quad (2.10)$$

Furthermore, calculations using this method are generally limited to simple systems, since this method is very computationally demanding. As we discussed in session 2.1.1, Hartree-Fock method transforms one problem of  $N$  interacting bodies into  $N$  coupled one-body problems. The fact that a different  $f_{F,i}[\phi_i]$  term must be calculated for each one-body problem contributes to the method complexity.

In this scheme, we assume the total wave function  $\Psi(\vec{r}_1, \dots, \vec{r}_N)$ , which depends on the coordinates of the  $N$  electrons, as our key object. However, there is another way to attack the problem in which the key object is the total electron density  $n(\vec{r})$ . That is the density functional theory (DFT), which is mainly founded on two Hohenberg-Kohn theorems (KOHN, 1965).

The first theorem guarantees that the ground state electronic density  $n(\vec{r})$  of a system of  $N$  electrons determines a unique potential that acts on the electron. We will prove this theorem assuming a system with a non-degenerate ground state, although the theorem can also be applied to the degenerate case.

Suppose by contradiction that there is a system of  $N$  electrons in which the external potential on the electronic system is not determined uniquely by  $n(\vec{r})$ . Therefore, there are two potentials,  $V_{ext}(\vec{r})$  and  $V'_{ext}(\vec{r})$ , associated with different Hamiltonian operators,  $\hat{H}$  and  $\hat{H}'$ , with ground states given by the wave functions  $\psi(\vec{r})$  and  $\psi'(\vec{r})$ , respectively, which generate the same electron density  $n(\vec{r})$ .

Since  $\psi(\vec{r})$  and  $\psi'(\vec{r})$  are the ground states of  $\hat{H}$  and  $\hat{H}'$ , respectively, we can write the

inequalities 2.11 and 2.12.

$$\langle \psi | \hat{H} | \psi \rangle < \langle \psi' | \hat{H} | \psi' \rangle \quad (2.11)$$

and

$$\langle \psi' | \hat{H}' | \psi' \rangle < \langle \psi | \hat{H}' | \psi \rangle. \quad (2.12)$$

Subtracting one inequality from the other, we find that

$$\langle \psi | \hat{H} - \hat{H}' | \psi \rangle < \langle \psi' | \hat{H} - \hat{H}' | \psi' \rangle \quad (2.13)$$

$$\langle \psi | V_{ext} - V'_{ext} | \psi \rangle < \langle \psi' | V_{ext} - V'_{ext} | \psi' \rangle \quad (2.14)$$

Which is a contradiction, because both sides of the inequality gives the same result

$$\int (V_{ext} - V'_{ext})n(\vec{r})d^3r < \int (V_{ext} - V'_{ext})n(\vec{r})d^3r \quad (2.15)$$

as we wanted to prove. Thus, the theorem has been proved by *reductio ad absurdum*.

The second Hohenberg-Kohn theorem guarantees that the density of the ground state of a system is the one that minimizes the total energy functional  $E[n]$  given by

$$E[n] = F[n] + \int n(\vec{r})V_{ext}[n](\vec{r})d^3r \quad (2.16)$$

where  $F[n]$  is given by

$$F[n] = \min_{\psi \rightarrow n} \langle \psi | \hat{T} + \hat{V}_{ee} | \psi \rangle = \langle \psi[n] | \hat{T} + \hat{V}_{ee} | \psi[n] \rangle, \quad (2.17)$$

the minimum value of kinetic energy with electron-electron interaction energy among all possible antisymmetric wave functions that generate the same electron density. In fact, it must be true, because if an electronic density does not minimize  $E[n]$  then it cannot come from the ground state.

Since  $F[n]$  does not depend on the external potential, it is a universal functional. Despite this fact, it does not have a known exact explicit expression, but only several different approximations to the this potential are available in literature.

Based on these two exposed theorems, Kohn and Sham in 1965 were the first to

present a variational method to the electronic structure calculation of systems of many particles from which later came to the known Kohn-Sham equations (KOHN, 1965). In this framework the real system of  $N$  interacting electrons is substituted by a fictitious system of  $N$  non-interacting electrons that generates the same electronic density  $n(\vec{r})$  of the real interacting system.

From the first theorem, we can calculate the total energy of the real system from the electronic density  $n(\vec{r})$  of the fictional non-interacting system and the energy functional  $E[n]$ . We can write the universal functional  $F[n]$  as a sum of three terms:

$$F[n] = T_0[n] + U_0[n] + E_{XC}[n], \quad (2.18)$$

where the exchange and correlation functional  $E_{XC}[n]$  is given by

$$E_{XC}[n] = V_{ee}[n] - U_0[n] + T[n] - T_0[n], \quad (2.19)$$

$T_0[n]$  is the kinetic energy of non-interacting electron system, which can be written as

$$T_0[n] = -\frac{1}{2} \sum_{i=1}^N \int \phi_i^*(\vec{r}) \nabla^2 \phi_i(\vec{r}) d^3r, \quad (2.20)$$

$T[n]$  is kinetic energy of the real interacting electron system,

$$T[n] = -\frac{1}{2} \int \psi^*[n](\vec{r}_1, \dots, \vec{r}_N) \nabla^2 \psi[n](\vec{r}_1, \dots, \vec{r}_N) d^3r_1 \dots d^3r_N, \quad (2.21)$$

$U_0[n]$  is classic electrostatic energy of non-interacting electrons

$$U_0[n] = \frac{1}{2} \int \frac{n(\vec{r})n(\vec{r}')}{|\vec{r} - \vec{r}'|} d^3r d^3r', \quad (2.22)$$

and  $V_{ee}[n]$  is the energy of mutual interaction between the electrons in the real system

$$V_{ee}[n] = \frac{1}{2} \sum_{i \neq j} \int \frac{\psi^*[n](\vec{r}_1, \dots, \vec{r}_N) \psi[n](\vec{r}_1, \dots, \vec{r}_N)}{|\vec{r}_i - \vec{r}_j|} d^3r_1 \dots d^3r_j. \quad (2.23)$$

The solution of the fictional non-interacting system can be obtained from the so called Kohn-Sham orbitals  $\{\phi_i(\vec{r})\}$ . Since this set of orbitals is orthonormal, its electronic density

can be written as

$$n(\vec{r}) = \sum_{i=1}^N |\phi_i(\vec{r})|^2. \quad (2.24)$$

So it is possible to obtain the equation that determines the orbital Kohn-Sham  $\phi_i(\vec{r})$  simply by using the Lagrange multipliers formalism respecting the constraint of the orbitals normalization

$$\int |\phi_i(\vec{r})|^2 dr = 1. \quad (2.25)$$

Therefore, we can state that

$$\frac{\delta}{\delta \phi_i^*} \left[ E[n] - \epsilon_i \left( \int |\phi_i(\vec{r})|^2 dr - 1 \right) \right] = 0. \quad (2.26)$$

Developing equation 2.26 we arrive to the Kohn-Sham equations,

$$\left[ -\frac{1}{2} \nabla^2 + V_H(\vec{r}) + V_{XC}(\vec{r}) + V_{ext}(\vec{r}) \right] \phi_i(\vec{r}) = \epsilon_i \phi_i(\vec{r}), \quad (2.27)$$

where the Hartree potential  $V_H(\vec{r})$  is given by

$$V_H(\vec{r}) = \frac{\delta U_0}{\delta n(\vec{r})} = \int \frac{n(\vec{r}')}{|\vec{r} - \vec{r}'|} d^3 r' \quad (2.28)$$

and the exchange and correlation potential  $V_{XC}(\vec{r})$  is defined as

$$V_{XC}(\vec{r}) = \frac{\delta E_{XC}}{\delta n(\vec{r})}, \quad (2.29)$$

which does not have an exact explicit analytic expression.

These equations determine the Kohn-Sham orbitals  $\phi_i(\vec{r})$  of the fictional non-interacting system and generates the same electronic density  $n(\vec{r})$  from the real interacting system. Observe that, rigorously, the only connection between these two systems is the electronic density  $n(\vec{r})$  and the properties that derived from it, such as the total energy.

Given an electronic charge density, it is possible to calculate the  $N$  Kohn-Sham orbitals independently. Because, unlike the Hartree-Fock problem, the Kohn-Sham equations are only coupled by the total electronic density.

We can face the Kohn-Sham potential as an average potential that acts on an independent electron in the system which includes effects related to the external potential  $V_{ext}(\vec{r})$ ,

the electrostatic interaction included in the Hartree potential  $V_H(\vec{r})$  and quantum effects represented by exchange and correlation potential  $V_{XC}(\vec{r})$ .

Typically this problem is solved by a self-consistent approach. An adequate approximation is chosen to deal with the exchange and correlation potential and then the algorithm represented by flowchart of Figure 2.1 is executed.

In the next sessions, different approximations to the exchange and correlation potential are discussed.

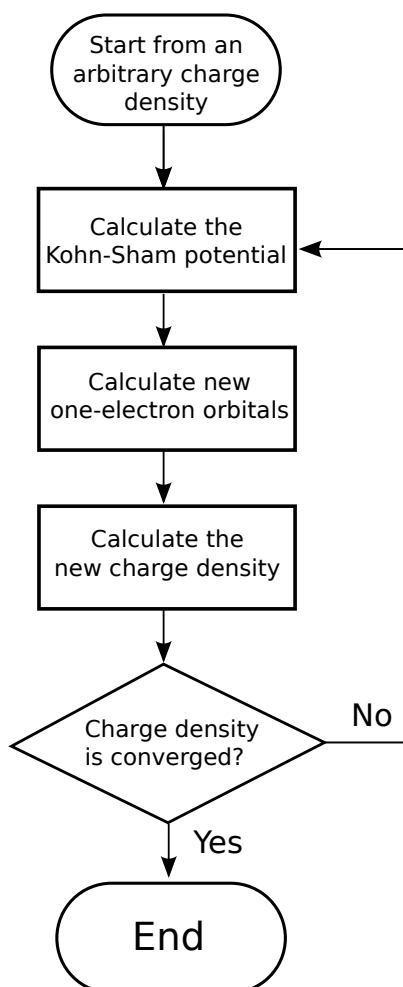


FIGURE 2.1 – Flowchart of the algorithm used in the self-consistent solution of the Kohn-Sham equations.

### 2.1.3 Local Density Approximation (LDA)

The exchange and correlation potential gathers the major complexity of the interaction between electrons and many different approximations have been proposed to obtain reliable prediction by computational simulations. One of the most popular approximations is the Local Density Approximation (LDA).

The LDA approach approximates the exchange and correlation energy functional  $E_{xc}$  as local functional  $E_{xc}^{LDA}$ . Then, it is possible to define the local exchange and correlation per particle  $e_{xc}[n]$  as (PARR, 1989)

$$E_{xc}^{LDA} = \int e_{xc}[n(\vec{r})]n(\vec{r})d^3r, \quad (2.30)$$

where  $e_{xc}[n(\vec{r})]$  is the exchange-correlation energy per particle of a uniform electron gas of density  $n$ , and thus only depends on the local electronic density  $n(\vec{r})$ .

Splitting  $e_{xc}^{LDA}[n(\vec{r})]$  in exchange and correlation contributions

$$e_{xc}^{LDA}[n(\vec{r})] = e_x[n(\vec{r})] + e_c[n(\vec{r})], \quad (2.31)$$

the  $e_x[n(\vec{r})]$  can be determined assuming that the infinitesimal volume element can be well approximated by a uniform electron gas. For the non-spin-polarized case one may write

$$e_x^{LDA}[n(\vec{r})] = -\frac{3}{4} \left( \frac{3}{\pi} \right)^{\frac{1}{3}} n^{\frac{1}{3}}(\vec{r}). \quad (2.32)$$

The correlation energy contribution does not have an exact explicit expression. Since the approximation of an electron gas does not include correlation effects, this quantity estimation must consider other results, such as quantum Monte Carlo calculations (MARTIN, 1980).

### 2.1.4 Generalized Gradient Approximation (GGA)

Since the local density approximation considers the exchange and correlation effects of a uniform electron gas for an infinitesimal volume element with electronic density  $n(\vec{r})$ , the LDA is, by definition, exact for a homogeneous system, and arbitrarily accurate for a system of sufficiently slowly varying density. In real systems however,  $n(\vec{r})$  is a rather rapidly varying function of  $\vec{r}$ , and any effects of local variations of the electronic density are neglected in LDA.

One possible way to include corrections associated with electronic density variations on the exchange and correlation potential is the gradient expansion approximation (GEA) of the functional

$$E_{xc}^{GEA} = \int e_{xc}^{(1)}[n(\vec{r})]n(\vec{r})d^3r + \int e_{xc}^{(2)}[n(\vec{r})]|\nabla n(\vec{r})|^2d^3r, \quad (2.33)$$

however such approximation does not necessary fulfill the sum rule conditions that must

be satisfied by the exact exchange-correlation potential. Therefore such expansion does not necessary gives better results than LDA (BECHSTEDT, 2015).

Despite of this obstacle, many groups have worked on the development of generalized gradient approximations to the exchange and correlation potential considering semi-local functionals

$$E_{xc}^{GGA} = \int f[n(\vec{r}), \nabla n(\vec{r})] d^3r, \quad (2.34)$$

designed to fulfill different sum rules and scaling laws. Among the several GGA alternatives proposed in literature (LEE *et al.*, 1988; PERDEW; YUE, 1986; BECKE, 1988), we considered in this work the Perdew-Burke-Erzenhof (PBE) (PERDEW *et al.*, 1996) approximation, which is the one of most popular approaches available in the literature.

In DFT with approximated exchange-correlation functionals, the cancellation is incomplete and the remainder is known as self-interaction error. The exact exchange-correlation energy functional would cancel the self-energy interaction. However, as this functional is unknown, we are restricted to approximated functionals with nonzero self-interaction errors. There are several methods to reduce this term, here we cite the hybrid functionals and the DFT-1/2 method.

### 2.1.5 Hybrid Potentials

The standard DFT approach, both considering local or semi-local exchange and correlation potentials, gives predictions for ground-state properties with good accuracy. On the other hand, *ab initio* predictions based on DFT of physical properties which depend on excited states usually do not share the same precision. It is well known, for example, that energy gap is underestimated by such theoretical approach.

The Hartree-Fock gives an exact solution to the exchange energy, however the effect that it does not consider, the correlation energy, makes this methodology unable to well describe chemical bondings (BECKE, 1993) and in the case of solid it usually predicts overestimated energy gaps (DURIG, 1998).

To solve these problem, exchange and correlation potential approximation combining Hartree-Fock and Density Functional Theory contribution were proposed. The associated weight to each contribution depends on the considered approximation to the exchange correlation potential. Becke (BECKE, 1993) proposed equal weight of 1/2 to each contributions and became known as half-and-half hybrid. On the other hand this choice is essentially arbitrary and other approximations with different weights have been tested in order to reproduce the experimental findings (PERDEW *et al.*, 1996; ADAMO; BARONE,

1999; STEPHENS *et al.*, 1996).

Further investigations on the optimal ratio between the exchange contribution of GGA-PBE functional and Hartree-Fock method arrived in a ratio of 1:3

$$E_{xc}^{PBE0} = \frac{1}{4}E_x^{HF} + \frac{3}{4}E_x^{PBE} + E_c^{PBE}, \quad (2.35)$$

which is known as PBE0 (ADAMO; BARONE, 1999).

Such approach for big molecules and solids is computational demanding due the slow convergence of the Hartree-Fock exchange, specially for metallic materials (HEYD *et al.*, 2003). Heyd, Scuseria and Ernzerhof proposed a screened Coulomb potential to the exchange interaction in order to screen the long-range part of the HF exchange and spare computational effort (HEYD *et al.*, 2003), known as HSE functional.

In this approach, the Coulomb operator in the HF exchange contribution is split into short-range and long-range components as

$$\frac{1}{r} = \frac{\text{erfc}(\mu r)}{r} + \frac{\text{erf}(\mu r)}{r}, \quad (2.36)$$

where the error function is given by  $\text{erf}(x) = \frac{2}{\sqrt{\pi}} \int_0^x e^{-t^2} dt$  and the complementary error function is defined as  $\text{erfc}(x) = 1 - \text{erf}(x)$ . In this equation,  $\mu$  is an adjustable parameter associated with the screening of the Hartree-Fock exchange interaction.

In order to combine good precision with fast convergence, the average between Hartree-Fock and PBE exchange contributions can be only applied to the short-range (SR) domain, while the long-range (LR) exchange interaction only considers PBE functional. This considerations lead to the following exchange and correlation energy HSE hybrid functional

$$E_{xc}^{HSE} = \frac{1}{4}E_x^{SR,HF}(\mu) + \frac{3}{4}E_x^{SR,PBE}(\mu) + E_x^{LR,PBE}(\mu) + E_c^{PBE}. \quad (2.37)$$

If screening parameter  $\mu = 0$ , HSE functional is reduced to the PBE0 one, while the situation  $\mu \rightarrow \infty$  it recovers the PBE functional. In the original work, there was shown that there is only a small dependence between the physical properties predictions and the screening parameter and the optimal value of  $\mu = 0.3\text{\AA}^{-1}$  was proposed (HEYD *et al.*, 2003). This first version of the HSE hybrid functional is known as HSE03. Three years later, an erratum was published reconsidering the optimal screening value to  $\mu = 0.2\text{\AA}^{-1}$  (HEYD *et al.*, 2006). This second version is known as HSE06, which is the one we used in this work.

Due to the slow convergence of the Hartree-Fock method and the need of calculating different Fock terms of exchange for each orbital, even hybrid potentials are much more time consuming than conventional DFT calculations. The solution of screening the Hartree-Fock

exchange interaction mitigate the problem, but HSE calculations can still demand about  $10^4$  more time than DFT calculations (PELA *et al.*, 2015).

### 2.1.6 DFT-1/2 method

Ferreira, Marques, and Teles, our group leaders, developed the DFT-1/2 methodology, which is able to correct the energy gap results with similar precision of such conventional gap correction methods, but with the same computational effort with standard DFT calculations (FERREIRA *et al.*, 2008; FERREIRA *et al.*, 2011). Recently, Pelá *et al.* (PELA *et al.*, 2015), by performing a comparison among DFT-1/2, HSE03, HSE06 and the considered “state of art” GW calculations, showed that DFT-1/2 present the best compromise considering accuracy of the results and the computational effort for disordered systems.

The DFT-1/2 methodology is derived in the spirit of Slater-Janak transition-state-theory (SLATER; JOHNSON, 1972; JANAK, 1978; LEITE; FERREIRA, 1971), solving the problem of its implementation to the case of infinite solid systems, giving a practical scheme for band gap calculations of semiconductors (FERREIRA *et al.*, 2008; FERREIRA *et al.*, 2011).

The Janak’s theorem (JANAK, 1978) states that the derivative of the total energy  $E(N)$  of a system with  $N$  electrons with respect to the occupancy number  $f_i$  of an arbitrary state  $\alpha$  is given by its respective Kohn-Sham eigenvalue

$$\frac{\partial E(N)}{\partial f_\alpha} = \varepsilon_\alpha(f_\alpha). \quad (2.38)$$

Combined with the assumption of the linearity of the eigenvalues with the orbital occupancies (FERREIRA *et al.*, 2011; LEITE; FERREIRA, 1971), one may calculate the ionization energy  $I$  and electron affinity  $A$  of an  $N$  electron system as

$$I = E(N - 1) - E(N) = -\varepsilon_v(1/2), \quad (2.39)$$

and

$$A = E(N) - E(N + 1) = -\varepsilon_c(1/2), \quad (2.40)$$

where  $\varepsilon_v(1/2)$  and  $\varepsilon_c(1/2)$  represent respectively the eigenenergies associated with valence band maximum and conduction band minimum. A scheme illustrating the half occupation technique is given in Fig. 2.2.

While the half-occupation scheme provides accurate atomic ionization potentials, it

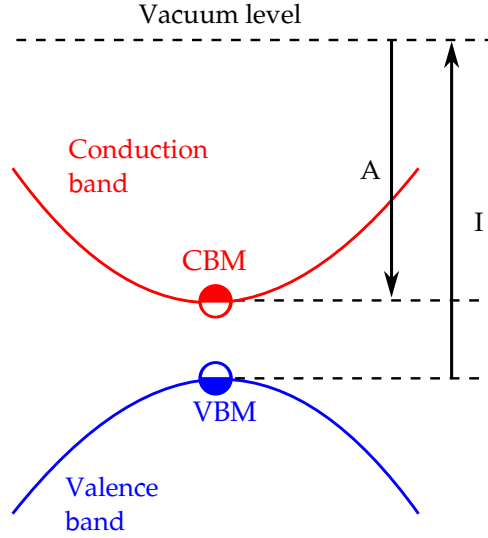


FIGURE 2.2 – Half occupation scheme of DFT-1/2 considering self energy corrections on valence and conduction bands. Half electron is removed from VBM, while half electron is added to CBM, to corrections on electronic affinity and ionization energy, respectively.

cannot be directly applied to extended crystalline systems. In DFT-1/2 approach the orbital-dependent self-energy  $S_\alpha$  is considered as a quantum mechanical average of a “self-energy potential”  $V_S(\vec{r})$

$$S_\alpha = \int d^3r n_\alpha(\vec{r}) V_S(\vec{r}) \quad (2.41)$$

of a Kohn-Sham state  $\alpha$  with  $n_\alpha(\vec{r})$  being its correspondent electronic density. The self-energy potential  $V_S(\vec{r})$  is approximately given by the difference between the Kohn-Sham potentials for the ion and the atom

$$V_S(\vec{r}) = -V(-1/2, r) + V(0, r). \quad (2.42)$$

In crystals the self-energy correction is obtained by subtracting the self-energy potential  $V_S(\vec{r})$  from the local part of the atomic pseudopotential or the  $-2Z/r$  part of the all-electron potential. To avoid the penetration of the self-energy coulomb tails into neighbouring atom sites, the self-energy potentials are trimmered according to  $\tilde{V}_S = \Theta(r)V_S(\vec{r})$  by a cutoff function  $\Theta(r)$

$$\Theta(r) = \begin{cases} A \left[1 - \left(\frac{r}{CUT}\right)^8\right]^3 & \text{if } r \leq CUT \\ 0 & \text{if } r \geq CUT \end{cases}, \quad (2.43)$$

where  $A$  and  $CUT$  are constants.  $A$  is considered as +1 (plus one) when we are considering the valence band  $V_{s,v}$  (the removal of half electron) and as  $-1$  (minus one) in the case of

conduction band  $V_{s,c}$  (the addition of half electron). The value of the CUT parameter is determined in a variational way to make the band gaps extremal (FERREIRA *et al.*, 2008)

$$\frac{\delta E_g^{QP}}{\delta \tilde{V}_S(\vec{r})} = 0, \quad (2.44)$$

without falling back to empirical parameters.

Finally, the following one-particle Kohn-Sham DFT-1/2 equation must be solved

$$\left[ -\frac{1}{2}\nabla^2 + V_{KS}(\vec{r}) + \tilde{V}_{s,v}(\vec{r}) + \tilde{V}_{s,c}(\vec{r}) \right] \varphi_i(\vec{r}) = \epsilon_i \varphi_i(\vec{r}), \quad (2.45)$$

where  $\tilde{V}_{s,v}$  ( $\tilde{V}_{s,c}$ ) is the trimmed valence (conducting) self-energy potential. Thus the DFT-1/2 energy gap is directly given by the difference between eigenvalues  $\epsilon_c - \epsilon_v$  with the same computational cost as a standard DFT calculation.

### 2.1.7 Bloch Theorem

There are several different ways of solving the Kohn-Sham equations. Since we want to describe crystalline systems, we will start discussing the Bloch theorem, which tells us which form the solutions of the Schrödinger equation must satisfy and also how to index the solutions.

An arbitrary crystalline system can be described with a Bravais Lattice and a basis. The symmetries observed in the crystalline structure are preserved both in the electronic charge density and the Kohn-Sham potential. However, there is no guarantee that this symmetry holds to the wave function, since it is an imaginary physical quantity.

Consider one particle subjected to the following periodic Hamiltonian operator

$$\hat{H} = -\frac{1}{2}\nabla^2 + V_{ext}(\vec{r}) \quad (2.46)$$

with  $V_{ext}(\vec{r})$  satisfying the following translational periodicity condition

$$V_{ext}(\vec{r}) = V_{ext}(\vec{r} + \vec{R}) \quad (2.47)$$

for all vector  $\vec{R}$  that belongs to a Bravais lattice.

The Bloch theorem (FAZZIO, 1995; MARDER, 1976; ASHCROFT; MERMIN, 1960) states

that the particle eigenstates of the Hamiltonian operator can be written as

$$\psi_{n\vec{k}} = e^{i\vec{k}\cdot\vec{r}} u_{n\vec{k}}(\vec{r}), \quad (2.48)$$

where  $u_{n\vec{k}}(\vec{r})$  is a periodic function with the same translational symmetry as the external potential  $u_{n\vec{k}}(\vec{r}) = u_{n\vec{k}}(\vec{r} + \vec{R})$  for all translations  $\vec{R}$  that belongs to the Bravais lattice.

This can be verified by expanding the particle wave function  $\Psi(\vec{r})$  and the periodic potential  $V_{ext}(\vec{r})$  in a set of plane waves. Considering the Born-Von Karman periodic contour conditions the wave function can be written as (ASHCROFT; MERMIN, 1960)

$$\Psi(\vec{r}) = \sum_{\vec{q}} c_{\vec{q}} e^{i\vec{q}\cdot\vec{r}}. \quad (2.49)$$

Since  $V_{ext}(\vec{r})$  is periodic, it can be expanded in plane waves with wave vectors  $\vec{K}$  given by the reciprocal crystal lattice

$$V_{ext}(\vec{r}) = \sum_{\vec{K}} U_{\vec{K}} e^{i\vec{K}\cdot\vec{r}}. \quad (2.50)$$

The Schrödinger equation  $\hat{H}\Psi(\vec{r}) = E\Psi(\vec{r})$  can be expanded to the equation

$$\sum_{\vec{q}} e^{i\vec{q}\cdot\vec{r}} \left[ \left( \frac{q^2}{2} - E \right) c_{\vec{q}} + \sum_{\vec{K}} U_{\vec{K}} c_{\vec{q}-\vec{K}} \right] = 0, \quad (2.51)$$

which can only be satisfied if all the expansion coefficients are identically zero. This equation shows that only the waves which wave vectors  $\vec{q}$  differ by one vector  $\vec{K}$  of the reciprocal lattice are coupled. Therefore it is possible to label the following solutions by one wave vector  $\vec{k}$  that belongs to the first Brillouin zone and one integer number corresponding to the other wave vectors  $\vec{k} + \vec{K}$  which are coupled to  $\vec{k}$ .

It follows from such coupling that wave functions  $\Psi_{\vec{k}}(\vec{r})$  can be written as a linear combination of the correspondent plane waves

$$\Psi_{\vec{k}}(\vec{r}) = \sum_{\vec{K}} c_{n,\vec{k}+\vec{K}} e^{i(\vec{k}+\vec{K})\cdot\vec{r}}, \quad (2.52)$$

factoring  $e^{i\vec{k}\cdot\vec{r}}$  from the equation we obtain

$$\Psi_{\vec{k}}(\vec{r}) = e^{i\vec{k}\cdot\vec{r}} \sum_{\vec{K}} c_{\vec{k}+\vec{K}} e^{i\vec{K}\cdot\vec{r}}. \quad (2.53)$$

Therefore, the solution for the Schrödinger equation subjected to a periodic potential is

$$\Psi_{\vec{k}}(\vec{r}) = e^{i\vec{k}\cdot\vec{r}} u_{\vec{k}}(\vec{r}), \quad (2.54)$$

where  $u_{\vec{k}}(\vec{r}) = \sum_{\vec{K}} c_{\vec{k}+\vec{K}} e^{i\vec{K}\cdot\vec{r}}$  is a function with the same periodicity than the corresponding Bravais lattice and the coefficients  $c_{\vec{k}+\vec{K}}$  can be calculated imposing null coefficients to the series written in the equation 2.51.

The Bloch theorem give not only valuable information about the necessary conditions that must be satisfied by the one-electron wave function in a periodic potential, but also how to index solutions in terms of one wave vector  $\vec{k}$  from the first Brillouin zone and a integer number. This solution indexing scheme leads to the description of eigenenergy dispersion as an electronic band structure, which is a fundamental tool to solid state physics.

### 2.1.8 Projector Augmented Wave (PAW) method

One natural basis choice to describe the eigenfunctions  $\Psi_{\vec{k}}(\vec{r})$  of a crystalline system is a set of plane wave. In general, electronic states localized close to the ionic cores exhibit strong oscillations. The description of these states would require a dramatically larger set of plane waves, which implies on significant enhancement of simulations memory and time consumption. One efficient alternative to overcome this problem and reduce the number of plane waves needed to obtain good approximations of the wave functions is the Projector Augmented Wave (PAW) method (KRESSE, 1999; BLOCHL, 1994).

It is known that the chemical properties do not strongly depend on inner electronic states, only on the valence electrons. Inspired by this chemical insight, the PAW method (BLOCHL, 1994) divides the space into two regions: the augmented region  $\Omega_A$ , composed of points which are closer than  $r_c$  radius from some nuclei in the crystalline structure, and the interstitial region  $\Omega_I$ , with the remaining part of the state. The two regions are treated separately.

The goal of this method is to provide an accurate description of valence electrons in order to reproduce chemical properties of a crystalline system. In this formalism, the actual functions  $|\psi\rangle$  are transformed into pseudo-functions  $|\psi'\rangle$  that can be calculated in a simpler way from their actual counterparts. The two functions are the same in the  $\Omega_I$ , being described as plane waves, while in  $\Omega_A$  the pseudo-functions  $|\psi'\rangle$  do not exhibit variations as strong as the real functions  $|\psi\rangle$ . On the boundary between the augmented and interstitial regions, one must ensure the continuity and differentiability of the pseudo-function. The calculation of pseudo-functions is meant to calculate chemical properties with an efficient way to describe the valence electrons. Consider the transformation  $\hat{T}$  that relates the

actual and pseudo- wave functions

$$|\psi\rangle = \hat{T} |\psi'\rangle. \quad (2.55)$$

Since the  $|\psi\rangle$  and  $|\psi'\rangle$  only differ inside spheres centered on the nuclei, the transformation operator  $\hat{T}$  can be written as the sum of the identity operator with the transformation operators  $\hat{T}_{\vec{R}}$  responsible for the addition of difference between  $|\psi\rangle$  and  $|\psi'\rangle$  in the vicinity of the atomic site located at the nuclei located by  $\vec{R}$  vector (KRESSE, 1999)

$$\hat{T} = \hat{1} + \sum_{\vec{R}} \hat{T}_{\vec{R}}. \quad (2.56)$$

A set of convenient all electrons  $|\phi_i\rangle$  and pseudo orbitals  $|\phi'_i\rangle$  are determined in order to calculate the nodal structure of the valence electrons in the  $\Omega_A$  region. In the vicinity of the nuclei located by vector  $\vec{R}$ , the all electrons and pseudo orbitals are mapped according to the equation  $|\phi_i\rangle = \hat{T} |\phi'_i\rangle$ . These orbitals are typically partial waves in the augmented region, resembling the Kohn-Sham solutions for free atom in this limited region.

It can be shown (KRESSE, 1999) that the transformation operator can be written as

$$\hat{T} = \hat{1} + \sum_i (|\phi_i\rangle - |\phi'_i\rangle) \langle p'_i|, \quad (2.57)$$

where  $\langle p'_i|$  represents projector operator of the pseudo-function  $|\psi'\rangle$  on pseudo orbital  $|\phi'_i\rangle$  partial wave, which must fulfill the condition  $\langle p'_i|\phi'_j\rangle = \delta_{ij}$ . The actual wave function can be, therefore written as

$$|\psi\rangle = |\psi'\rangle + \sum_i \langle p'_i|\psi'\rangle |\phi_i\rangle - \sum_i \langle p'_i|\psi'\rangle |\phi'_i\rangle, \quad (2.58)$$

$$|\psi\rangle = |\psi'\rangle + |\psi^1\rangle - |\psi'^1\rangle. \quad (2.59)$$

The decomposition of the actual wave function in its pseudo counterpart, indicated as  $'$ , and central quantities in  $\Omega_A$  regions, indicated as  $^1$ , is also possible to other physical quantities. The real charge density  $n(\vec{r})$  can be written as (KRESSE, 1999)

$$n(\vec{r}) = n'(\vec{r}) + n^1(\vec{r}) - n'^1(\vec{r}), \quad (2.60)$$

where  $n'(\vec{r})$  is the pseudo electronic density and  $n^1(\vec{r})$  and  $n'^1(\vec{r})$  are the on-site charge density from the real function and pseudo wave functions, respectively. As described

elsewhere (BLOCHL, 1994), the effective Hamiltonian operator acting on the pseudo-wavefunctions can be expressed as

$$\hat{H}' = -\frac{1}{2}\nabla^2 + \hat{V}'_{eff} + \sum_{i,j} \langle p'_i | (D'_{ij} + D_{ij}^1 - D_{ij}^1) | p'_i \rangle, \quad (2.61)$$

where  $D'_{ij}$ ,  $D_{ij}^1$  and  $D_{ij}^1$  are operators related to the decomposition of  $n(\vec{r})$  in terms of  $n'(\vec{r})$ ,  $n^1(\vec{r})$  and  $n^1(\vec{r})$ . This operator allows us to calculate a Schrödinger like DFT equation for the pseudo-function  $|\psi'\rangle$  that demands a small fraction of the Kohn-Sham equations 2.27 written in terms of the actual wave functions  $|\psi\rangle$ .

## 2.2 Thermodynamic properties and statistical model for alloyed systems

### 2.2.1 Generalized Quasichemical Approximation (GQCA)

The VASP software applies periodic boundary conditions to the given structure, so this tool could not directly deal with non-periodic disordered systems, such as random alloys. This obstacle can be surpassed by the application of a statistical approach combined with *ab initio* calculations based on DFT. First we will focus on the study of binary alloys, which can be represented as  $A_{1-x}B_x$ , where A and B represent different compounds and  $x$  is the average B composition in the system and finally some results will be generalized to a ternary alloy.

We start with the classic definition of the Gibbs free energy  $G$  of a system with enthalpy  $H$ , entropy  $S$  and temperature  $T$

$$G = H - TS, \quad (2.62)$$

which can be rewritten using the definition of enthalpy as

$$G = E + PV - TS, \quad (2.63)$$

where  $E$  is the internal energy,  $P$  is the pressure and  $V$  is the volume of the corresponding system.

It follows from thermodynamics that the equilibrium state of a system maintained at a constant temperature and pressure corresponds to the state of minimum Gibbs energy

(GOKCEN, 1986). In the case of solid materials under pressures about 1 atm, we have

$$G \approx E - TS = F, \quad (2.64)$$

where  $F$  is the Helmholtz free energy. We can also define conveniently the mixing free energy  $\Delta F$  as the deviation from the Helmholtz free energy from the weighted average for the concentration of the free energy of the A and B pure compounds (SHER, 1995)

$$\Delta F(x, T) = F(x, T) - (1 - x)F_A(T) - xF_B(T), \quad (2.65)$$

where  $F(x, T)$ ,  $F_A(T)$  and  $F_B(T)$  represent, respectively, the Helmholtz free energy of the studied alloy, compound A and compound B. We can decompose  $\Delta F$  into two contributions, one from the mixing energy  $\Delta E$  and the other from the mixing entropy  $\Delta S$

$$\Delta F = \Delta E - T\Delta S. \quad (2.66)$$

There are different models to describe the terms  $\Delta E$  and  $\Delta S$ . We will adopt in this work the generalized quasi-chemical approximation (GQCA). Consider a system decomposed in statistically and energetically independent with  $n$  sites that may be occupied by an atom A or B. Possible generalizations will be discussed in the sessions 2.2.3 and 2.2.4. Initially, we can list  $2^n$  different supercells configurations, ranging from a configuration in which all sites filled with atoms A to another one filled only with atoms B. Due the fact that crystalline structures are symmetric some configurations can be obtained from the application of some symmetry operations on the atomic arrangement, such as rotation, translation or reflection. These configurations are equivalent, since they share the same physical properties. Let  $g_j$  be degeneracy of a specific configuration  $j$ , given by the number of atomic arrangements among the  $2^n$  considered ones that are equivalent to the cluster configuration  $j$ .

Therefore, exploring the crystalline symmetry group we can reduce our list of  $2^n$  configurations to  $J$  non-equivalent cluster classes with different degeneracies  $g_j$ . Let  $M$  be the total number of clusters in an alloyed system and  $M_j$  the number of clusters  $j$ . One can calculate the mixing internal energy as

$$\Delta E = \sum_{j=1}^J M_j E_j - M(xE_A + (1 - x)E_B) \quad (2.67)$$

where  $E_A$  and  $E_B$  are the energies of the clusters occupied only by atoms A and B, respectively, and  $x$  is the concentration of type A atoms in the alloy.

In order to add corrections on the mixing entropy estimation, we must consider the information given by the number  $M_j$  of clusters  $j$  observed in the system. Consider the number of possible configurations of the alloy calculated on the random distribution of atoms, multiplied by a term that considers the probability of achieving a certain distribution of  $\{M_j\}$  cluster. This expression can be normalized by the *a priori* probabilities  $x_j^o = g_j x^{n_j} (1-x)^{n-n_j}$  of finding the cluster  $j$  if the alloy were perfectly random (CHEN; SHER, 1995).

$$\Phi = \frac{N!}{N_A! N_B!} \frac{M!}{\prod_j M_j!} \prod_j (x_j^o)^{M_j} \quad (2.68)$$

Using Stirling's approximation  $\ln(N!) \approx N \ln(N) - N$ , we can write the mixing entropy in terms of the occurrence probability  $x_j = M_j/M$  of the cluster  $j$  in the alloy.

$$\Delta S = -Nk(x \ln(x) + y \ln(y)) - Mk \sum_j x_j \ln \left( \frac{x_j}{x_j^o} \right), \quad (2.69)$$

with  $y = 1 - x$  and  $k$  the Boltzmann constant. Substituting these results in the expression  $\Delta F = \Delta E - T\Delta S$ , we obtain the mixing free energy as a function of the occurrence probabilities  $x_j$

$$\Delta F = \sum_{j=1}^J M_j E_j - M(x E_A + (1-x) E_B) + NkT(x \ln(x) + y \ln(y)) + MkT \sum_j x_j \ln \left( \frac{x_j}{x_j^o} \right) \quad (2.70)$$

The probabilities  $x_j$  are the values that minimize  $\Delta F$ , respecting the condition of probability normalization and the alloy average composition  $x$ . The two constraint conditions can be written, respectively, by the equations

$$\sum_{j=1}^J x_j = 1 \quad (2.71)$$

$$\sum_{j=1}^J n_j x_j = nx. \quad (2.72)$$

This problem can be solved using the Lagrange multipliers formalism. Then when get

a set of  $J$  equations given by

$$\frac{\partial}{\partial x_j} \left( \frac{\Delta F}{M} - \lambda_1 \left[ \sum_{j=1}^J x_j - 1 \right] - \lambda_2 \left[ \sum_{j=1}^J n_j x_j - nx \right] \right) = 0, \forall j \in \{1, 2, 3, \dots, J\}, \quad (2.73)$$

where  $\lambda_1$  and  $\lambda_2$  are the Lagrange multipliers associated with the normalization and average constraints, respectively. We can develop this set of equations and determine the probabilities  $x_j$

$$x_j = \frac{x_j^0 \exp[(\lambda_2 n_j - \Delta \varepsilon_j)/kT]}{\sum_{j=1}^J x_j^0 \exp[(\lambda_2 n_j - \Delta \varepsilon_j)/kT]}, \quad (2.74)$$

where  $\Delta \varepsilon_j$  is the configuration excess energy given by the equation

$$\Delta \varepsilon_j = E_j - \frac{n_j}{n} E_A - \frac{n - n_j}{n} E_B. \quad (2.75)$$

Defining  $\lambda = x e^{\lambda_2/kT} / (1 - x)$ , we can rewrite the equation as

$$x_j = \frac{g_j \lambda^{n_j} \exp[(-\Delta \varepsilon_j)/kT]}{\sum_{j=1}^J g_j \lambda^{n_j} \exp[(-\Delta \varepsilon_j)/kT]}, \quad (2.76)$$

where  $\lambda$  can be determined by the mean composition constraint.

Each cluster  $j$  can be associated with an infinite periodic system obtained by the repetition of the correspondent atomic arrangement in the space. The physical properties of this system can be calculated using an *ab initio* methodology, representing as  $P_j$  a particular property of the cluster  $j$  of interest. Then, we can estimate the alloy property  $P_{alloy}(x, T)$  through an average of  $P_j$  values weighted by the probabilities  $x_j$ . Then, we write

$$P_{GQCA}(x, T) = \sum_{j=1}^N x_j(x, T) P_j. \quad (2.77)$$

In addition, we can evaluate the uncertainty of the estimation by the standard deviation associated with the distribution of  $P_j$  values

$$\Delta P_{GQCA}(x, T) = \sqrt{\left[ \sum_{j=1}^N x_j(x, T) P_j^2 \right] - \left[ \sum_{j=1}^N x_j(x, T) P_j \right]^2}. \quad (2.78)$$

## 2.2.2 Thermodynamic stability and phase decomposition

The  $T$ - $x$  phase diagram of an alloy is obtained from two curves: the binodal and spinodal. These curves divide the diagram into three regions corresponding to stable, meta-stable or unstable conditions.

Given a growth temperature  $T$ , we can study the  $\Delta F/M$  of a binary alloy as a function of the mean composition  $x$ . For each concentration  $x$  the GQCA approach calculate a set of occurrence probabilities  $\{x_j\}$ , which can be use to calculate  $\Delta F/M$  as

$$\frac{\Delta F}{M} = \sum_{j=1}^J x_j E_j - (xE_A + (1-x)E_B) + nkT(x \ln(x) + y \ln(y)) + kT \sum_j x_j \ln \left( \frac{x_j}{x_j^o} \right). \quad (2.79)$$

Performing the calculation of the free energy of the alloy for several compositions  $x$ , adopting a fixed temperature value  $T$ , one obtain the behavior of the alloy mixing free energy curve as a function of the concentration of its compounds.

For temperatures lower than the critical temperature, there may be a miscibility gap, i.e. concentrations  $x$  where the alloy becomes unstable and tends to split into two different stable phases with concentrations  $x_1$  and  $x_2$ , with  $x_1 < x_2$ . The  $x_1$  and  $x_2$  values are such that in the equilibrium condition the two phases share the same chemical potential  $\mu$ , which can be associated with the derivative of  $\Delta F(x, T)$  with respect to  $x$

$$\frac{\partial \Delta F(x_1, T)}{\partial x} = \frac{\partial \Delta F(x_2, T)}{\partial x}. \quad (2.80)$$

One condition that must be observed in this case is that the phase separation must give lower free energy than the condition of one only phase with composition  $x$  between  $x_1$  and  $x_2$ , as we see in figure 2.3. In fact, the decomposition into two phases with concentrations  $x_1$  and  $x_2$  gives the minimum possible free energy with an average  $x_1 < x < x_2$ . The set of concentrations  $x_1$  and  $x_2$  for different temperatures form the binodal curve in the  $T$ - $x$  diagram.

Other important points of the free energy curve are inflection points  $x'_1$  and  $x'_2$ , where the concavity of the free energy of mixing curve changes. For a given temperature, the concentrations points  $x'_1$  and  $x'_2$  are determined from the equations

$$\frac{\partial^2 \Delta F(x_1, T)}{\partial^2 x} = 0, \quad \text{and} \quad \frac{\partial^2 \Delta F(x_2, T)}{\partial^2 x} = 0. \quad (2.81)$$

The alloy is stable in the composition ranges  $x < x_1$  and  $x > x_2$ , unstable in  $x'_1 < x < x'_2$  and metastable in the intervals  $x_1 < x < x'_1$  and  $x'_2 < x < x_2$ . The interval  $x_1 < x < x_2$

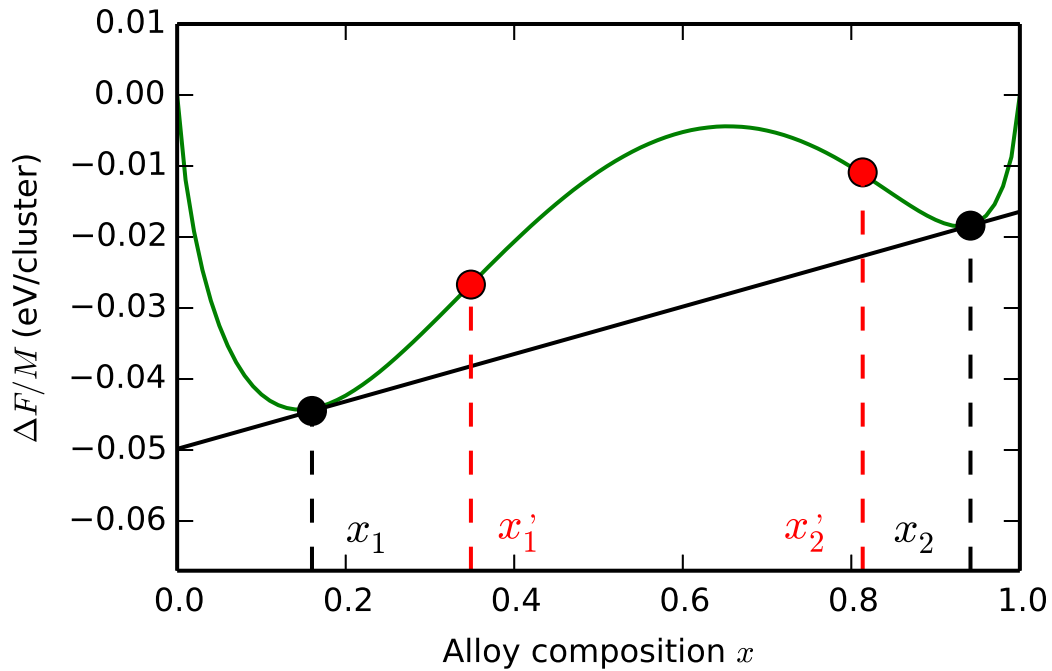


FIGURE 2.3 – Mixing excess energy of an alloy calculated at an arbitrary temperature. The concentrations  $x_1$  and  $x_2$  are determined by the common tangent method and the  $x'_1$  and  $x'_2$  are calculated by the change of curve concavity.

have higher free energy than its decomposition into two phases with composition  $x_1$  and  $x_2$ . The instability and the metastability may be distinguished by considering small local composition fluctuations. If the concavity in  $x$  of  $\Delta F(x, T)$  is negative, i.e. the curve is concave, a small disturbance tends to lower the free energy, it occurs in the whole alloy and the system is decomposed in order to obtain a minimum free energy.

If the concavity of the curve at the point  $x$  is upward, i.e. the curve is convex, although the decomposition in the phases with compositions  $x_1$  and  $x_2$  could lower the system free energy, small perturbations in the alloy concentration tends to increase the system free energy. In these composition ranges  $x_1 < x < x'_1$  and  $x'_2 < x < x_2$  there is an energy barrier for the decomposition. In this situation, one may say that the alloy is metastable.

The phase diagram is composed by the binodal and the spinodal curves. This diagram summarizes the information about the alloy thermodynamic stability. The two curves split the diagram in three different regions. The points  $(x, T)$  above the binodal curve correspond to stable condition for the alloy growing, the points between the two curves corresponds to metastable conditions and, finally, the points below the spinodal correspond to unstable condition. The figure 2.4 depicts an example of a  $T$ - $x$  phase diagram.

In the region below the spinodal curve the alloy decomposes into two different phases with average compositions  $x_1$  and  $x_2$  thereby minimizing the mixing free energy  $F(x, T)$  for given  $x$  and  $T$ . The poor and rich phases with concentrations  $x_1$  and  $x_2$  are respectively

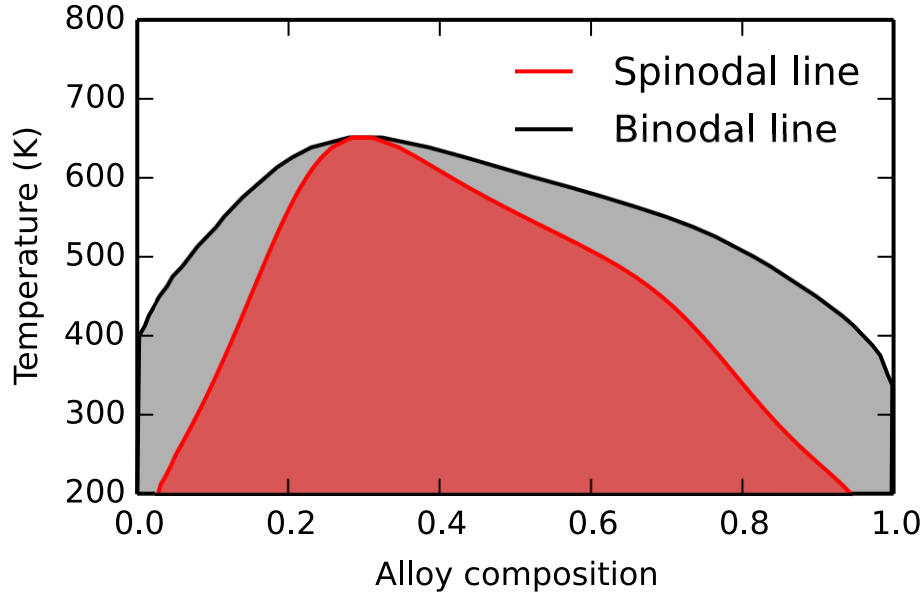


FIGURE 2.4 – Arbitrary example of  $T$ - $x$  phase diagram. The stable, metastable, and unstable regions are represented by the white, grey, and red colors, respectively.

characterized by statistical weights

$$w_1 = \frac{x_2 - x}{x_2 - x_1} \quad \text{and} \quad w_2 = \frac{x - x_1}{x_2 - x_1}. \quad (2.82)$$

The alloy average properties estimated by equation 2.77 should be reasonable to represent homogeneous systems under stable  $(x, T)$  conditions and systems with small cluster sizes where composition fluctuation effects between the two segregated phases are relevant. If these conditions are not fulfilled and the system is fully segregated in poor and rich phases, i.e. for temperatures and compositions below the binodal curve, a more reliable estimation of the mean absorbance spectra is given by

$$P_{PS}(x, T) = w_1(x, T)P_{GQCA}(x_1, T) + w_2(x, T)P_{GQCA}(x_2, T) \quad (2.83)$$

with  $w_1$  and  $w_2$  the statistical weights defined in equations (2.82).

### 2.2.3 Generalizations concerning ternary alloys

In this work, we are also interested in alloys that can be represented as  $(A_2)_{x'}(BC)_{1-x'}$ . Despite the fact that, these alloys are completely defined with one average composition parameter  $x$  and behave somehow like a pseudo-binary alloy. Their statistics must be obtained by particularization of a ternary alloy  $A_xB_yC_z$ .

Each term in equation 2.79 for the binary alloys has a physical interpretation that can

be generalized to the ternary case, dispensing a reformalization from the very beginning. The mixing internal energy  $\Delta E^{(bin)} = \sum_{j=1}^J x_j E_j - (xE_A + (1-x)E_B)$  can be corrected by considering the three end components

$$\Delta E^{(ter)} = \sum_{j=1}^J x_j E_j - (xE_A + yE_B + zE_C) \quad (2.84)$$

and new set of cluster configuration possibilities arising from the fact that a third element can occupy each atomic site. The term  $\Delta S_0^{(bin)} = -(x \ln(x) + y \ln(y))$  can be interpreted as the entropy per atomic site of a random binary alloy according to the Shannon entropy (SALINAS, 1997), therefore it must be corrected to a generic ternary alloy as

$$\Delta S_0^{(ter)} = -k(x \ln(x) + y \ln(y) + z \ln(z)), \quad (2.85)$$

and finally the quantity

$$D_{KL}(x_j || x_j^o) = -k \sum_j x_j \ln \left( \frac{x_j}{x_j^o} \right) \quad (2.86)$$

can be interpreted as the relative entropy or the Kullback-Leibler divergence (KULLBACK; LEIBLER, 1951), which is associated with the information lost in the assumption of a probability distribution among the several clusters  $x_j^o$  instead of  $x_j$ , assumed to be the correct probability distribution. This expression should remain unchanged. Considering these observations, we may write for ternary alloys

$$\begin{aligned} \frac{\Delta F^{(ter)}(x, y, T)}{M} &= \sum_{j=1}^J x_j E_j - (xE_A + yE_B + zE_C) \\ &+ nkT(x \ln(x) + y \ln(y) + z \ln(z)) + kT \sum_j x_j \ln \left( \frac{x_j}{x_j^o} \right). \end{aligned} \quad (2.87)$$

The  $(A_2)_{x'}(BC)_{1-x'}$  alloy is described by setting  $x = x'$  and  $y = z = \frac{1-x'}{2}$ . The equation 2.79 can be reformulated, considering the two possible end components as  $E_A$  and  $E_{BC}$  as

$$\begin{aligned} \frac{\Delta F(x)}{M} &= \sum_{j=1}^J x_j E_j - (xE_A + (1-x)E_{BC}) \\ &+ nkT \left( x \ln(x) + (1-x) \ln \left( \frac{1-x}{2} \right) \right) + kT \sum_j x_j \ln \left( \frac{x_j}{x_j^o} \right). \end{aligned} \quad (2.88)$$

It is also interesting to discuss what is the effect of considering only a subset  $S'$  of  $J'$  cluster configurations among the initial set  $S$  with  $J > J'$  configurations. In the  $(A_2)_x(BC)_{1-x}$  alloy study, for example, we may restrict the sample set  $S'$  to only those configurations with  $n_B = n_C$ . Therefore, the *a priori*  $x_j^o$  of a configuration  $j$  in  $S'$  set can be corrected by a normalization factor that comes from the conditional probability

$$x_j^o = P(j|j \in S') = \frac{P(j)}{P(j \in S')} \quad (2.89)$$

$$x_j^o = P(j|j \in J') = \frac{g_j x^{n_{A,j}} \left(\frac{1-x}{2}\right)^{n-n_{A,j}}}{\sum_{j \in S'} g_j x^{n_{A,j}} \left(\frac{1-x}{2}\right)^{n-n_{A,j}}}. \quad (2.90)$$

The determination of the probability distribution  $x_j$  can still be recalculated by considering the same constraints given by equations 2.71 and 2.72 considering the subset of configurations  $S'$ . Observe that the correction on  $\Delta S_0^{(ter)}$  is irrelevant in the minimization of the mixing free energy, since it does only depend on the alloy average composition, and that the normalization factor is cancelled in equation 2.74. The modification of the  $x_j^o$  can be absorbed by a redefinition of the auxiliary parameter  $\lambda$  as  $\lambda = 2xe^{\lambda_2/kT}/(1-x)$  and the result given by equation 2.76 still holds with only slight changes

$$x_j = \frac{g_j \lambda^{n_{A,j}} \exp[(-\Delta\varepsilon_j)/kT]}{\sum_{j \in S'} g_j \lambda^{n_{A,j}} \exp[(-\Delta\varepsilon_j)/kT]} \quad (2.91)$$

Since these alloys are completely defined with one average composition parameter  $x$ , the same stability formalism based on  $x_1, x'_1, x'_2$  and  $x_2$  special compositions obtained from the  $\Delta F(x, T)$  can be directly applied.

## 2.2.4 Generalization of GQCA for 2D functionalized sheets

In previous works, the entropy of an alloyed system has been derived from the number of possible combinations between different elements (GUILHON *et al.*, 2015; TELES *et al.*, 2000; MARQUES *et al.*, 2003). Hence, the correction of the system entropy referring to the cluster distribution is obtained from combinatorics arguments (MARQUES *et al.*, 2006). The exact number of atomic arrangements is a relatively easy task, since it naturally arises from a combination of a defined set of atoms in  $N$  atomic sites.

In this work, we are interested not only in 2D substitutional alloys, but also in 2D functionalized sheets. In such systems, the absence of adsorbant group, groups adsorbed above or below the sheet may be counted in an analogous way as a ternary substitutional alloy with the same structure of the considered sheet. However, the adsorbed of groups on first-neighbor sites on the same side of the sheet might lead to very large total energies, due

to repulsion between these groups. Such situation asks for the constraints of the adsorbed groups, in order to obtain moderate energy values, which changes the total number of arrangements. The functionalized sheet may be also decorated with multisite adsorption groups, leading to a non-trivial configuration counting. In fact, different approximate solutions have been proposed to this problem in literature (ROMA *et al.*, 2003; D'AVILA *et al.*, 2006). Indeed, the difficulty in the analysis of a multisite statistics has been addressed for dimer adsorption on various 2D lattices (ROMA *et al.*, 2003). The introduction of structural constraints on adsorption groups distributions, and the occurrence of multisite adsorbants result into a non-trivial number of allowed arrangements.

The previous formulation to calculate the number of atomic arrangements, and therefore the system entropy, depends on combinatoric arguments to derive equation 2.68. However, we have discussed how the obtained results can be interpreted and generalized to a ternary alloy using the Shannon entropy (SALINAS, 1997), leading to equation 2.85, and the correction of the GQCA to the entropy term (eq. 2.86) may be interpreted as a Kullback-Leibler divergence (KULLBACK; LEIBLER, 1951) of *a priori* and *a posteriori* probability distributions. These results show the close relationship between configurational entropy of atoms in the cluster expansion and the occurrence probability distribution of elements and clusters.

To avoid the complications originated from the combinatoric arguments in these special cases, we will propose an alternative approach to calculate the entropy term that does not require any combinatoric arguments. To accomplish this task, we start with the Shannon entropy per cluster from the very first beginning, calculating  $\Delta S/M$  in terms of probability distribution  $x_j$ . However, to calculate the configurational entropy one needs to use not the probability distribution among the symmetry classes, but on the atomic arrangements themselves. Since the GQCA supposes that the clusters are statistically independent from the neighborhood, there is not favoring between the occurrence of any of the  $g_j$  atomic arrangements that belong to the same symmetry class  $j$ . Therefore the occurrence probability of an arbitrary arrangement from symmetry class  $j$  is given by  $p_{j,arr} = x_j/g_j$ . The Shannon entropy per cluster is then calculated as

$$\frac{\Delta S}{M} = -k \sum_{j,arr} p_{j,arr} \ln(p_{j,arr}), \quad (2.92)$$

covering all the  $g_j$  possible arrangements that belong to each the symmetry class  $j$  and all the  $J$  identified symmetry classes. This expression can be rewritten in terms of the identified symmetry classes probabilities  $x_j$  as

$$\Delta S = kM \sum_{j=1}^J x_j (\ln g_j - \ln x_j). \quad (2.93)$$

This formula is simpler than the previously considered entropy expressions (GUILHON *et al.*, 2015; TELES *et al.*, 2000; MARQUES *et al.*, 2006), but reproduces the same results in the thermodynamic limit with no need of combinatorics arguments. We will demonstrate the equivalence between the two different approaches for substitutional alloys.

Consider the simplest case that we considered in the regular solution (CHEN; SHER, 1995), which is a perfectly random binary substitutional alloy with  $N$  atomic sites that can be occupied by  $N_A = xN$  atoms  $A$  and  $N_B = (1 - x)N$  atoms  $B$ . Since the identity  $x_j = x_j^0$  holds for this system, the equation 2.69 results in the following entropy

$$\Delta S_0^{(bin)} = -Nk[(1 - x)\ln(1 - x) + x\ln(x)]. \quad (2.94)$$

One may also consider the probability distribution approach to obtain the same result. Since the atoms are randomly distributed, the *a priori* probability distribution  $x_j^o$  is determined by each configuration degeneracy  $g_j$ , the average composition  $x$  of element A, and  $y$  of element B ( $x + y = 1$ ) as

$$x_j^o = g_j x^{n_{A,j}} y^{n_{B,j}}, \quad (2.95)$$

with  $n_{A,j}$  ( $n_{B,j}$ ) representing the number of A (B) atoms in cluster  $j$ .

Substituting this probability distribution in the entropy expression (2.93), one obtains a configurational entropy

$$S' = -kM \left( \sum_{j=1}^J x_j n_{A,j} \ln x + \sum_{j=1}^J x_j n_{B,j} \ln y \right). \quad (2.96)$$

The average composition constraints  $\sum_{j=1}^J x_j n_{A,j} = nx$  and  $\sum_{j=1}^J x_j n_{B,j} = ny$  yield on the same result of equation 2.94. This equivalence of the two approaches can be easily generalized for random alloys of more atomic components.

The equivalence between approaches still hold for a cluster expansion combined with GQCA. As previously demonstrated with combinatoric arguments, an alloyed system entropy is given by equation 2.69. A qualitative interpretation of each entropy term under the light of information theory has already been give in section 2.2.4. The difference  $\delta S$  between the entropy values per cluster calculated from equations 2.69 and 2.93 is

$$\delta S = -k \sum_{j=1}^J x_j \left( \frac{g_j}{x_j} \right) + k \sum_{j=1}^J x_j^o \left( \frac{g_j}{x_j^o} \right) + k \sum_{j=1}^J x_j \ln \left( \frac{x_j}{x_j^o} \right) \quad (2.97)$$

and

$$\delta S = -k \sum_{j=1}^J (x_j - x_j^o) \ln \left( \frac{g_j}{x_j^o} \right). \quad (2.98)$$

Substituting the random probability distribution  $x_j^o$ , given by (2.95) in the logarithm, we obtain that

$$\begin{aligned} \delta S = k \left\{ \left[ \sum_{j=1}^J x_j^o n_{A,j} - \sum_{j=1}^J x_j n_{A,j} \right] \ln x \right. \\ \left. + \left[ \sum_{j=1}^J x_j^o n_{B,j} - \sum_{j=1}^J x_j n_{B,j} \right] \ln y \right\}. \end{aligned} \quad (2.99)$$

Since the *a priori* and *a posteriori* probability distributions  $x_j^o$  and  $x_j$  refer to the same system, the terms in parenthesis cancel each other because the average composition  $x$  is a given constraint. Therefore, it holds

$$\delta S = 0, \quad (2.100)$$

and the informational and configurational approaches lead to the same result.

The proposed formalism to entropy calculation directly from the occurrence probability distribution  $x_j$ , as described in 2.93, has significant advantages comparing to 2.69. The obtained expression calculates the total entropy straight forwardly instead of calculating one term from combinatoric arguments, and the relative entropy associated to the difference between the *a priori*  $x_j^o$  and *a posteriori*  $x_j$  probability distributions. Since the combinatoric argument are not required any more, it represents a significant simplification to the disorder modeling of 2D functionalized sheets.

In this work, we consider system with a fixed number of particles as canonical ensembles. It is worthy saying that the approach proposed here to entropy calculation approach is also a simple alternative to the generalization of the GQCA methodology to systems modeled as grand-canonical ensembles. The demonstration of such result is left as an annex, and its application to different systems will be further explored by other studies in a near future.

## 2.3 Optical properties

### 2.3.1 Layer optical absorbance

The optical properties of matter follow from the coupling between electromagnetic fields to the possible electronic excitations. The optical transitions might have different strength of coupling depending on the relation between the photon energy and the difference between the initial and final electronic state.

To study the interaction between the electromagnetic field and the electronic structure, one may change the electron standard momentum operator  $\hat{p}$  by the generalized momentum operator  $\hat{p} + \frac{e}{c}\hat{A}(\vec{r}, t)$ , considering cgs units, in the Hamiltonian operator expression

$$\hat{H} = \frac{1}{2m}(\vec{p} + \frac{e}{c}\vec{A})^2 + V_{ext}(\vec{r}), \quad (2.101)$$

where  $\vec{A}(\vec{r}, t)$  represents the electromagnetic vector potential. Choosing the Coulomb gauge, where  $\nabla \cdot \vec{A} = 0$  the electric and the magnetic fields can be expressed in terms of the vector potential as  $\vec{E}(\vec{r}, t) = -\frac{1}{c}\frac{\partial}{\partial t}\vec{A}(\vec{r}, t)$  and  $\vec{B}(\vec{r}, t) = \nabla \times \vec{A}(\vec{r}, t)$ .

This problem can be solved using time dependent perturbation theory, where the optical properties are obtained by the coupling between different electronic states by the electromagnetic perturbation term according to the Fermi's golden rule (PIZA, 2003).

Let  $\vec{q}$  be the momentum and  $\omega$  the frequency of the incident light. It follows from the Ohm's law  $\vec{j}(\vec{q}, \omega) = \sigma(\vec{q}, \omega)\vec{E}(t)$ , where  $\sigma(\vec{q}, \omega)$  describes the material response to the incident wave as a complex number. From Ampere's Law, the relative dielectric function can be written as

$$\epsilon_r(\vec{q}, \omega) = 1 + i4\pi\frac{\sigma(\vec{q}, \omega)}{\omega}, \quad (2.102)$$

in CGS units.

Since the typical wavelengths are much larger compared to the lattices constants of crystalline structure in solid materials we can use the approximation  $\vec{q} \rightarrow 0$  and also neglect the local-fields corrections for the dielectric function. Considering these assumptions, one may write the dielectric function of a solid with respect to longitudinal perturbations as (EHRENREICH; COHEN, 1959; GAJDOS *et al.*, 2006)

$$\epsilon_r(\hat{q}, \omega) = 1 + \frac{4\pi e^2}{V} \sum_{c,v} \sum_{\vec{k}} |M_{cv}(\vec{k}, \hat{q})|^2 \frac{1}{\epsilon_c(\vec{k}) - \epsilon_v(\vec{k}) - \hbar\omega - i\eta}, \quad (2.103)$$

where  $\eta$  represents a small broadening to deal with divergences at resonances frequencies

and  $M_{cv}(\vec{k}, \hat{q})$  are the elements of the optical matrix

$$M_{cv}(\vec{k}, \hat{q}) = \lim_{\vec{q} \rightarrow \vec{0}} \frac{1}{|\vec{q}|} \langle c\vec{k} | e^{i\vec{q}\cdot\vec{r}} | v\vec{k} + \vec{q} \rangle. \quad (2.104)$$

In this work, we studied the optical absorbance  $A(\omega)$ , which is connected to the frequency-dependent imaginary part of the dielectric function  $\epsilon_r(\vec{q}, \omega)$ . The imaginary part of the dielectric function can be calculated taking the limit for small  $\eta$  values of the expression

$$\lim_{\eta \rightarrow 0} \frac{1}{\epsilon_c(\vec{k}) - \epsilon_v(\vec{k}) - \hbar\omega - i\eta} = \frac{1}{\epsilon_c(\vec{k}) - \epsilon_v(\vec{k}) - \hbar\omega} + i\pi\delta(\epsilon_c(\vec{k}) - \epsilon_v(\vec{k}) - \hbar\omega), \quad (2.105)$$

then we obtain

$$Im[\epsilon_r(\hat{q}, \omega)] = \frac{4\pi^2 e^2}{V} \sum_{c,v} \sum_{\vec{k}} |M_{cv}(\vec{k}, \hat{q})|^2 \delta(\epsilon_c(\vec{k}) - \epsilon_v(\vec{k}) - \hbar\omega). \quad (2.106)$$

The optical conductivity  $\sigma(\vec{q}, \omega)$  can be obtained from the imaginary part of the dielectric function according to equation 2.102

$$\sigma(\vec{q}, \omega) = \frac{\omega}{4\pi} Im[\epsilon_r(\hat{q}, \omega)]. \quad (2.107)$$

When the *ab initio* calculations are performed in the VASP package, the output dielectric function considers not only the 2D material, but also a large vacuum layer that isolate different layers that comes from the periodic conditions in the three dimensions. The 3D optical conductivity can be related to the 2D by a factor of  $L$ , which is the distance between two neighbor sheets. The sheet absorbance for in-plane light polarization with angular frequency  $\omega$  and isotropic layers can be expressed in terms of

$$A(\omega) = \frac{\omega}{c} L Im[\epsilon(\omega)]. \quad (2.108)$$

### 2.3.2 Average optical spectra

In a disordered system, where the cluster expansion is performed, the alloy statistic and the set of optical spectra  $A_j(\omega)$  calculated in the *ab-initio* framework for each cluster configuration  $j$  must be combined to obtain the alloy average optical spectrum.

The average absorbance spectra of an alloy at a specific photon frequency  $\omega$  can be estimated within GQCA by equation (2.77). Therefore, such expression can be generalized

for the whole optical spectrum as described by the expression

$$A_{GQCA}(\omega, x, T) = \sum_{j=1}^N x_j(x, T) A_j(\omega). \quad (2.109)$$

This average should be reasonable to represent homogeneous systems under stable  $(x, T)$  conditions and systems with small cluster sizes where composition fluctuation effects between the two segregated phases are relevant. These are the conditions in which the probability distribution among the clusters can be well described by the  $x_j(x, T)$  set of probabilities.

If these conditions are not fulfilled and the system is fully segregated in poor and rich phases, i.e. for temperatures and compositions below the binodal curve, there is one different set of occurrence probabilities for each cluster in each phase, described by  $x_j(x_1, T)$  and  $x_j(x_2, T)$ . In this situation, as already mentioned a more reliable estimation of the mean absorbance spectra is given by equation 2.83 and the phase separated absorbance can be written as

$$A_{PS}(\omega, x, T) = w_1(x, T) A_{GQCA}(\omega, x_1, T) + w_2(x, T) A_{GQCA}(\omega, x_2, T) \quad (2.110)$$

with  $w_1$  and  $w_2$  the statistical weights defined in equations (2.82).

## 2.4 VASP Software and computational details

In our work, we solved the Kohn-Sham equations as implemented in Vienna Ab Initio Package (VASP) (KRESSE, 2012). This simulation package is implemented with parallel programming MPI (KRESSE, 2012), with the aim of using multicore computers to parallelize the operations in order to reduce the processing time required by the computational simulations of electronic structures.

This code computes the approximate solution to the many-body Schrödinger equation as previously discussed. DFT and Hartree-Fock methods are both implemented. Hybrid functionals are available as well, and it is also possible to set the ratio between DFT and HF contribution to the considered exchange energy and the screening parameter  $\mu$  as well. Furthermore, Green's functions methods as GW are also available in VASP.

VASP expands the orbital wave functions into plane waves and applies periodic contour conditions, considering a given periodic cell and an atomic basis. The Kohn-Sham orbitals are solved within PAW formalism. In chapter 3, we use an energy cutoff parameter for plane

wave expansion of  $E_{cut} = 400eV$  and a  $9 \times 9 \times 1$   $\Gamma$ -centered  $k$ -point mesh to approximated integrals over the Brillouin-zone as a weighted sum over the sampled  $k$ -points. In chapter 4, a cutoff parameter  $E_{cut} = 450eV$  and a  $12 \times 12 \times 1$   $\Gamma$ -centered  $k$ -point mesh were considered. All the atomic coordinates are relaxed until Hellmann-Feynman forces are smaller than  $0.01 \text{ eV } \text{\AA}^{-1}$ . Each alloy system is simulated as an artificial 3D crystal constituted by a periodic repetition of the atomic sheets in a distance  $L = 20 \text{ \AA}$  from the neighbor ones. This distance is large enough that the interaction between the sheets vanishes.

The optical properties are described by the frequency-dependent dielectric matrix, which is calculated within the independent-quasiparticle approximation (ADOLPH *et al.*, 1996). The optical transition matrix elements are described adopting the longitudinal gauge (GAJDOS *et al.*, 2006). We focus on the optical absorbance  $A(\omega)$  for normal incident light with wavelength  $\omega$ . For dielectric function calculations a refined  $\Gamma$ -centered mesh  $42 \times 42 \times 1$  is used in order to increase the number of considered optical transitions in our calculations.

# 3 Group IV binary alloys

## 3.1 Introduction

A strong effort has been invested to study graphene-like 2D materials composed of other group-IV elements. It has been suggested that 2D sheets with a hexagonal lattice structure of Si and Ge, referred to as silicene and germanene, respectively, might exhibit similar properties as graphene, but with a low buckled structure instead of the planar one (CAHANGIROV *et al.*, 2009).

Scientific reports have progressed from theoretical predictions to experimental observations in only a few years (XU *et al.*, 2013). The formation of silicene was reported on Ag (1 1 1) (VOGT *et al.*, 2012; FENG *et al.*, 2012; CHIAPPE *et al.*, 2012), ZrB<sub>2</sub>(0 0 0 1) (FLEURENCE *et al.*, 2012) and Ir(1 1 1) (MENG *et al.*, 2013) surfaces. Very recently, germanene was grown on the Au(1 1 1) surface (DAVILA *et al.*, 2014), on Pt(1 1 1) substrate (LI *et al.*, 2014b), and as a termination of Ge<sub>2</sub>Pt crystals on Ge(1 1 0) (BAMPOULIS *et al.*, 2014). The angle-resolved photoemission spectroscopy revealed the presence of a linear dispersion in the band structure of silicene (so called Dirac cones) with a Fermi velocity of about  $1.3 \times 10^6$  m/s (VOGT *et al.*, 2012), higher than expected from free-standing graphene ( $1.1 \times 10^6$  m/s). The corresponding measured value for multilayer silicene (VOGT *et al.*, 2012) seems to be closer to velocities as theoretically predicted (HOUSSA *et al.*, 2011; HOUSSA *et al.*, 2014).

Despite the fact that silicene and germanene have no energy gap, theoretical predictions of binary systems indicate that a gap opening can be obtained by breaking the symmetry between the two sub-lattices of the honeycomb structure (SAHIN *et al.*, 2009; SUZUKI; YOKOMIZO, 2010). Photoluminescence experiments shows a strong light-emitting of 2D SiC nanoflakes at 373 nm (LIN, 2012), which is consistent with the previous predictions.

In this chapter, we will discuss the possibility of varying the composition of the alloyed 2D binaries formed by IV-A column elements and its consequences on the properties of the new system, which can be treated as an alloy. The GQCA statistical approach is, therefore, an important step to go beyond the simulation of a specific ordered atomic distribution and understand how thermodynamics influence the others physical properties

of the alloyed system. Whenever it is possible, we compare our results with available experimental data and other theoretical results as well.

## 3.2 Determination of the equivalence cluster classes

This study will focus on the 2D group IV binary alloys made from carbon, silicon and germanium  $\text{Si}_{1-x}\text{C}_x$ ,  $\text{Ge}_{1-x}\text{C}_x$  and  $\text{Ge}_{1-x}\text{Si}_x$ , which can be generic referred as  $\text{A}_{1-x}\text{B}_x$ . The first step in the study of such systems using GQCA approach consists in the choice of an adequate supercell for the cluster expansion of the alloys. In this work, the clusters are described by a 22 unit cell, as depicted in figure 3.1. This choice gives a reasonable compromise solution between computational costs and the number of possible atomic arrangements. The chosen supercell format preserves the same symmetry class as the primitive cell, which simplifies the count of the non-equivalent configuration classes. Read appendix A for a further discussion on the supercell cell size choice.

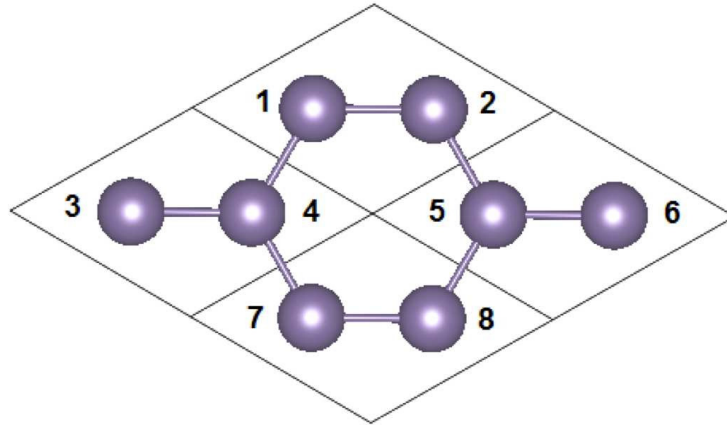


FIGURE 3.1 – Eight-atom supercell considered in the calculation. The atomic sites are labelled by 1,2,3,4,5,6,7,8.

The atomic sites can be occupied by the two different elements that correspond to the alloy endcomponents. The possible  $2^8 = 256$  atomic arrangements can be arranged in different equivalence classes. The planar honeycomb structure belongs to the  $C_{6v}$  point symmetry group (WATARI, 2009), since the structure is symmetric by a rotation of  $60^\circ$  and by reflections with respect to six different planes. There are also translational symmetries associated with two vectors of the Bravais lattice,  $\vec{a}_1$  and  $\vec{a}_2$ , and the vector  $\vec{a}_1 + \vec{a}_2$  as well.

Each symmetry operation can be transformed into a permutation of integer from 1 to 8, considering the labelling indicated in figure 3.1. If the cluster configuration can be obtained from the application of a symmetry operation on another one, these two atomic arrangements are called equivalent and the configuration class degeneracy is incremented. After all the possible configurations and symmetry operations are considered,  $J = 22$

non-equivalent cluster configurations are obtained. Each class has a different degeneracy  $g_j$ , as shown in table 3.1. The configurations are labelled by the occupation of atomic site 1 to atomic site 8, as depicted in figure 3.1. For example, the AAAAAABB configuration has atoms A located on the lattice sites of 1 to 6 and atoms B on sites 7 and 8.

TABLE 3.1 – For each different cluster class  $j$  it is presented one possible atomic arrangement and degeneracies  $g_j$  of 8-atom supercells to study  $\text{Si}_{1-x}\text{C}_x$ ,  $\text{Ge}_{1-x}\text{C}_x$  and  $\text{Ge}_{1-x}\text{Si}_x$  binary alloys. Each configuration is labelled according to the numeration represented in figure 3.1.

$j$	$g_j$	Label	$j$	$g_j$	Label
1	1	BBBBBBBB	12	6	AABBBBAA
2	8	ABBBBBBB	13	24	AAABBBAB
3	4	ABBBBBBA	14	24	AAABBABB
4	12	ABABBBBB	15	24	AAAAABBB
5	12	AABBBBBB	16	8	AAABABAB
6	8	ABABABBB	17	24	AAABBAAB
7	24	AABBBBAB	18	4	AAABBAAA
8	24	AAABBBBB	19	12	AAAAABAB
9	6	AAAABBBB	20	12	AAAAAABB
10	8	AAABABBB	21	8	AAAAAAAAB
11	2	ABABABAB	22	1	AAAAAAA

### 3.3 Thermodynamic properties

In an alloy where the mixing internal energy is not zero, the assumption that a random arrangement of atoms is the equilibrium geometry might not be acceptable. The actual arrangement of atoms will be a compromise that gives the lowest internal energy consistent with sufficient entropy, or randomness, to achieve the minimum free energy as discussed in section 2.2.1. The probability of occurrence of each configuration  $x_j$  depends on the average composition  $x$  in the alloy, the temperature and the excess energy of each configuration is defined in equation (2.75). To illustrate the effect of  $\Delta\varepsilon_j$  values on  $x_j$  calculations, we listed in Table 3.2 a column with  $x_j$  for an alloy with composition  $x=0.5$  at  $T=800$  K. One can observe that the configurations with lower excess energies are favored over the more energetic ones.

In systems with  $\Delta U < 0$  the internal energy of the system is reduced by increasing the number of  $A$ - $B$  bonds by ordering the atoms. If  $\Delta U > 0$  the internal energy can be reduced by increasing the number of  $A$ - $A$  and  $B$ - $B$  bonds by the clustering of the atoms in  $A$ -rich and  $B$ -rich domains. However, the degree of ordering or clustering will decrease as temperature increases due to the increasing importance of the entropy.

In systems where negative excess energies are observed ordered structures with low

TABLE 3.2 – Excess energy  $\Delta\varepsilon_j$  (eV) and statistical contribution  $x_j$  ( $x = 0.5, T = 800\text{K}$ ) of the cluster configurations  $\text{Ge}_{8-n_j}\text{C}_{n_j}$ ,  $\text{Si}_{8-n_j}\text{Ge}_{n_j}$  and  $\text{Si}_{8-n_j}\text{C}_{n_j}$ .

Class $j$	$\text{Ge}_{8-n_j}\text{C}_{n_j}$		$\text{Si}_{8-n_j}\text{Ge}_{n_j}$		$\text{Si}_{8-n_j}\text{C}_{n_j}$	
	$\Delta\varepsilon_j$	$x_j$	$\Delta\varepsilon_j$	$x_j$	$\Delta\varepsilon_j$	$x_j$
1	0.00	0.402	0.00	0.006	0.00	0.061
2	2.57	0.031	0.10	0.038	1.41	0.044
3	3.76	0.002	0.17	0.017	1.26	0.033
4	4.16	0.003	0.18	0.048	2.10	0.021
5	2.51	0.053	0.16	0.050	1.44	0.072
6	4.91	0.000	0.26	0.028	0.82	0.169
7	5.19	0.001	0.21	0.091	2.76	0.015
8	3.13	0.035	0.20	0.093	3.67	0.003
9	3.26	0.007	0.21	0.023	2.56	0.006
10	5.49	0.000	0.23	0.029	2.82	0.005
11	5.49	0.000	0.32	0.006	-0.18	0.300
12	5.31	0.000	0.23	0.022	2.32	0.010
13	5.70	0.000	0.24	0.086	2.53	0.026
14	4.78	0.002	0.22	0.091	3.46	0.005
15	5.28	0.001	0.20	0.093	3.72	0.003
16	6.64	0.000	0.26	0.028	2.28	0.016
17	6.22	0.000	0.22	0.091	3.60	0.004
18	4.40	0.001	0.17	0.016	2.18	0.011
19	6.90	0.000	0.19	0.048	3.52	0.003
20	7.63	0.000	0.16	0.051	3.84	0.002
21	5.34	0.000	0.11	0.038	3.24	0.004
22	0.00	0.462	0.00	0.006	0.00	0.187

excess energies may occur at low temperatures. First, we investigate the relative stability of ordered and disordered phases by observing the behaviour of  $\Delta F$  at  $T=0\text{K}$ , which corresponds to analyze the values of  $\Delta U$ . In addition, for each cluster class  $j$  we compute the excess energy  $\Delta\varepsilon_j$  of the considered cluster configurations. The results are listed in Table 3.2. For the 22 studied configurations for  $\text{Ge}_{1-x}\text{C}_x$  and  $\text{Si}_{1-x}\text{Ge}_x$  the values are non-negative, while for  $\text{Si}_{1-x}\text{C}_x$  the configuration 11 exhibits an excess energy  $\Delta\varepsilon_{11} < 0$ , that indicates a tendency for ordering in  $\text{Si}_{1-x}\text{C}_x$  alloy under small temperatures. In Fig. 3.2 (a), this fact is indicated by  $\Delta U < 0$  for all  $x$ , despite the fact that, apart from configuration 11, any configuration has an energy greater or equal to the  $\text{Si}_{1-x}\text{C}_x$  alloy consisting mainly of the configurations 1 (Si), 11 (SiC) and 22 (C). Indeed the  $\Delta U(x, T = 0\text{K})$  curve has one inflection point at  $x=0.5$ , which is mainly due to the ordered structure corresponding to configuration 11 (displayed as an inset in Fig. 3.2(a)). In this configuration the atomic sites represent an ideal honeycomb lattice and are occupied alternately. We conclude that the  $\text{Si}_{1-x}\text{C}_x$  alloy consists of domains of ordered 2D SiC, the silicographene (GORI *et al.*,

2012), graphene and silicene depending on the alloy composition. For  $x = 0.5$  at  $T = 0\text{K}$  only silicon-graphene is realized.

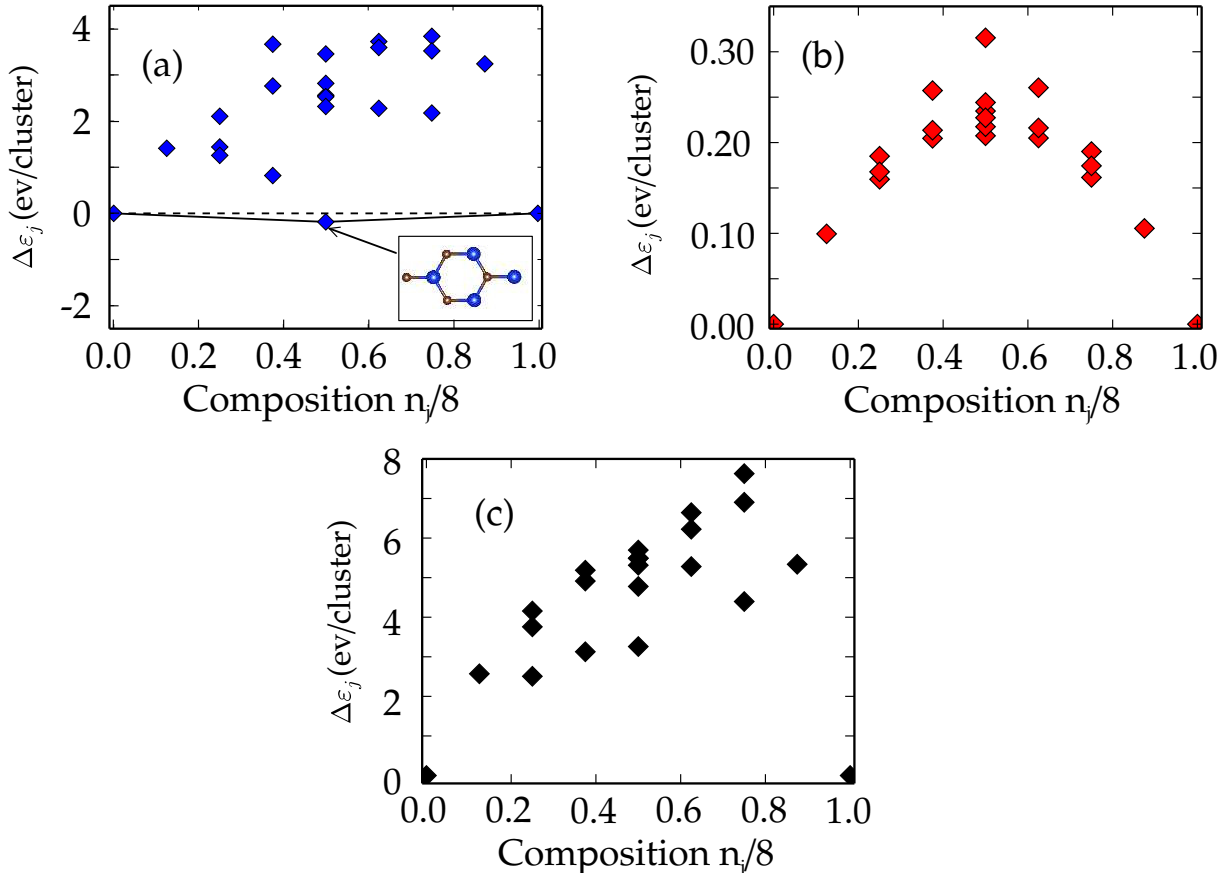


FIGURE 3.2 – Plot of the excess energies (2.75) of each  $\text{Si}_{8-n_j}\text{C}_{n_j}$  (a),  $\text{Ge}_{8-n_j}\text{Si}_{n_j}$  (b) and  $\text{Ge}_{8-n_j}\text{C}_{n_j}$  (c) configuration. In addition, the tie line representing the internal energy  $\Delta\varepsilon_j$  of  $\text{Si}_{1-x}\text{C}_x$  at  $T = 0\text{ K}$ , calculated through 2.75, is shown as function of the concentration  $x$ . The inset figure corresponds to configuration 11, i.e.  $sp^2$ -bonded SiC.

This result is underlined by Fig. 3.3 for the composition  $x = 0.5$ . In Fig. 3.3 (a) the values of  $x_j$  are plotted as a function of the temperature. At very low temperatures the ordered configuration 11 is predominant. As the temperature increases other configurations begin to contribute. Besides SiC, mainly graphene and silicene contribute. Also configuration 6 with 5 Si and 3 C atoms per cluster may be visible. At temperatures about  $T = 1000\text{ K}$ , one can say that the alloy is almost randomly disordered.

In order to quantify the degree of ordering, we calculate the short-range order (SRO) parameter, such that  $L = 1$  for a fully ordered alloy and  $L = 0$  for a completely random distribution. The SRO is defined as (PORTER; EASTERLING, 1981)

$$L = \frac{P_{\text{Si-C}} - P_{\text{Si-C}}^0}{P_{\text{Si-C}}^{\text{max}} - P_{\text{Si-C}}^0}, \quad (3.1)$$

where  $P_{\text{Si-C}}$  is the probability to find a Si-C bond in the considered alloy for a given  $x$

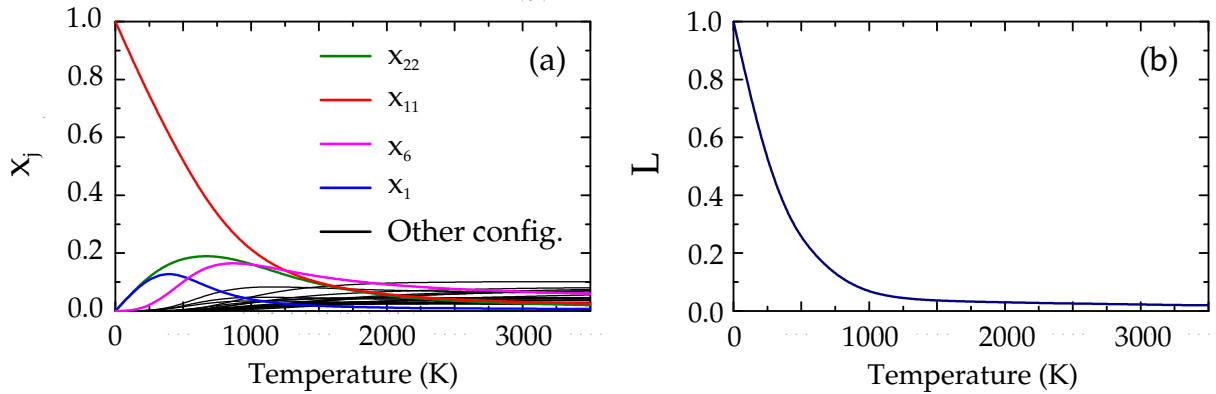


FIGURE 3.3 – (a) The probabilities  $x_j$  of all  $\text{Si}_{n_j}\text{C}_{8-n_j}$  configurations versus temperature at  $x = 0.50$ . Configurations 1, 6, 11 and 22 are highlighted. (b) Degree of ordering in  $\text{Si}_{1-x}\text{C}_x$  for  $x = 0.5$ , quantified as SRO parameter  $L$ , as a function of temperature.

and  $T$ , which can be estimated by the means of equation (2.77)

$$P_{\text{Si-C}}(x, T) = \sum_{j=1}^J x_j(x, T) P_{\text{Si-C},j}, \quad (3.2)$$

$P_{\text{Si-C}}^0 = 2x(1-x)$  describes this probability in a completely random alloy, and  $P_{\text{Si-C}}^{\text{max}} = 2\min\{x, 1-x\}$  is its possible maximum value, given by the concentration  $x$ . The order parameter is plotted in Fig. 3.3 (b) for  $x = 0.5$  versus the temperature. It again indicates complete ordering for  $T = 0\text{K}$ , but rapidly decreasing ordering for temperatures above  $T = 1000\text{K}$ .

In the case of  $\text{Ge}_{1-x}\text{C}_x$  and  $\text{Si}_{1-x}\text{Ge}_x$  the situation is completely different. It holds  $\Delta U(x, T) \geq 0$  for all compositions and temperatures. This is obvious from the excess energies in Table 3.2. Miscibility or spinodal decomposition should happen depending on composition and temperature, as described in section 2.2.2.

The application of the GQCA to these two binary alloys for different temperatures and compositions results in the  $T$ - $x$  phase diagrams. The results are shown in Fig. 3.4. They represent the binodal and the spinodal curves that divide the  $(x, T)$  points in zones of stable, metastable and unstable phases.

From Fig. 3.4(a) we observe a strong tendency of phase separation with a huge critical temperature of 22400 K for  $\text{Ge}_{1-x}\text{C}_x$ . This temperature represents the minimum temperature for which one has a completely random alloy of graphene mixed with germanene for any composition. For temperatures which can be experimentally accessed, only small amounts of carbon can be mixed into the 2D germanium in order to form a random alloy.

The situation is completely different if carbon is replaced by silicon as indicated by the phase diagram in Fig. 3.4(b). The  $\text{Si}_{1-x}\text{Ge}_x$  alloy has a critical temperature of 550

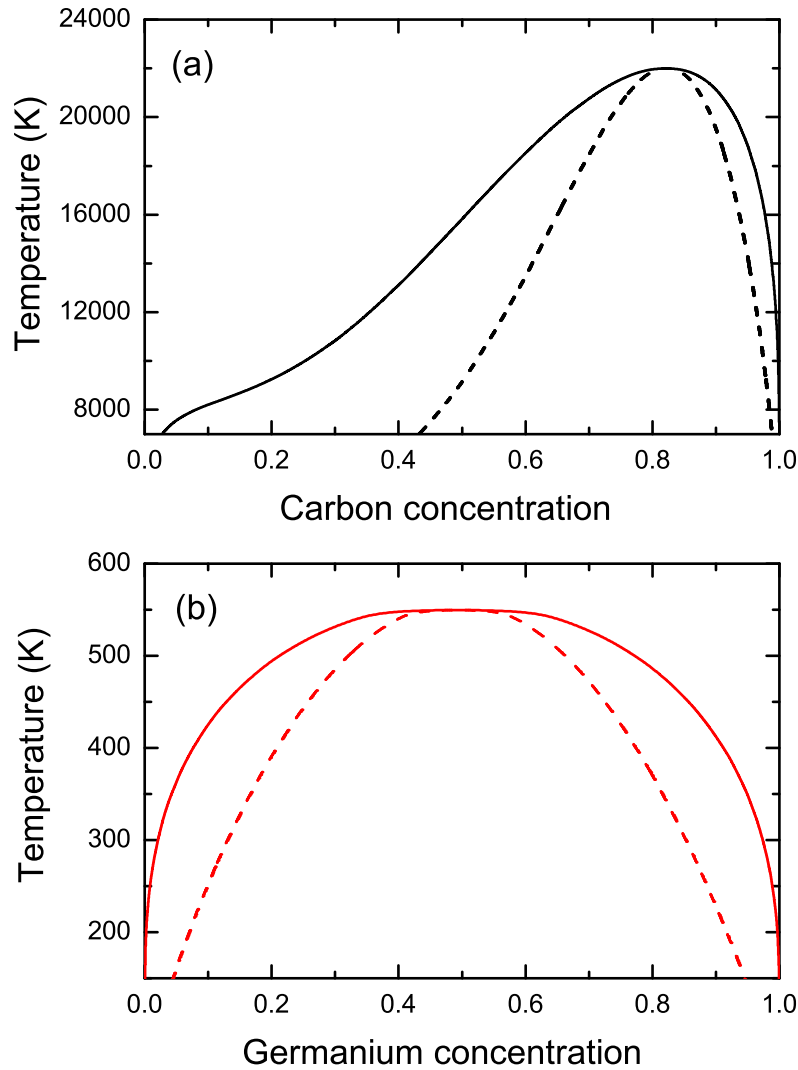


FIGURE 3.4 – The  $T$ - $x$  phase diagram of (a)  $\text{Ge}_{1-x}\text{C}_x$  (black) and (b)  $\text{Si}_{1-x}\text{Ge}_x$  (red). Solid lines: binodal curves; dashed lines: spinodal curves.

K, indicating the possibility to synthesize a random alloy of germanene and silicene, in agreement with results obtained within special quasirandom structures (SQS) (PADILHA *et al.*, 2013). The phase diagram is rather symmetric. For lower temperatures it indicates that in the equilibrium the random  $\text{Si}_{1-x}\text{Ge}_x$  alloys tend to decompose into a low-concentration and a high-concentration alloy.

In  $\text{Si}_{1-x}\text{Ge}_x$ , we observe smaller  $\Delta\varepsilon_j$  values explaining the achievable critical temperature of these alloys. On the other hand, most of the  $\text{Ge}_{1-x}\text{C}_x$  configurations exhibit higher excess energies, contributing to small  $x_j$  values, reflecting their immiscibility until very

high temperatures.

Consequently the details of the alloy statistics and thermodynamics can be related to the energetics of the individual cluster configurations. We observe from Table 3.2 that the excess energies of carbon-rich configurations are greater than germanium-rich ones. This means that adding germanium atoms to a graphene structure is more thermodynamically unfavorable comparing to incorporating carbons atoms in a germanene structure, since the first case demands bigger deformations of the atomic arrangements in the hexagonal unit cells. Both facts explain the asymmetry of the  $T$ - $x$  phase diagram in Fig. 3.4 (a).

## 3.4 Structural Properties

Our study of structural properties focus on the average lattice parameter and the average first-neighbor distances. These parameters are very important to evaluate possible stresses that may be observed if these materials are used in in-plane heterostructures. We also consider the buckling parameter of these materials, which represents displacements of the atomic sites in the honeycomb structure perpendicularly to the atomic layer.

The alloy properties are estimated within the GQCA approach. The alloy properties depends on the alloy average composition and the growth temperature. As was discussed before, in section 2.2.1, these results are derived from a weighted average of the clusters properties that make up the alloy, considering the probability of occurrence  $x_j$  of each of the different non-equivalent configurations. We perform explicit calculations at  $T = 800$  K based on the growth temperatures of graphene on SiC found in literature (LOGINOVA *et al.*, 2008). However, the calculated lattice constant curves do not change significantly for 500 K, approximately the growth temperature of germanene and silicene on Ag(111) (SONE *et al.*, 2014; LI *et al.*, 2014b).

### 3.4.1 Lattice parameter $a$

The configurationally averaged lattice parameter  $a$  is obtained by considering the equation (2.77) as

$$a = \sum_{j=1}^J x_j(x, T) a_j, \quad (3.3)$$

where  $a_j$  is the equilibrium lattice constant of each cluster  $j$ .

The resulting lattice constants projected onto a two-atom unit cell as in graphene, silicene or germanene are shown in Fig. 3.5. One verifies that for 2D  $\text{Ge}_{1-x}\text{C}_x$ ,  $\text{Si}_{1-x}\text{Ge}_x$

and  $\text{Si}_{1-x}\text{C}_x$  alloys the lattice parameter varies approximately linearly with the composition. Only a small bowing appears for the carbides.

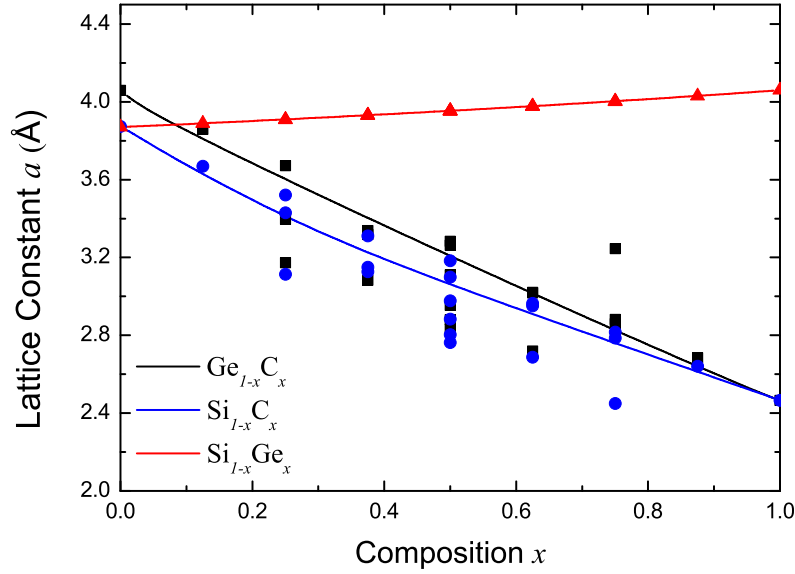


FIGURE 3.5 – The lattice parameter as a function of the composition for  $\text{Ge}_{1-x}\text{C}_x$  (black),  $\text{Si}_{1-x}\text{C}_x$  (blue) and  $\text{Si}_{1-x}\text{Ge}_x$  (red). The symbols represent the lattices parameters of an individual cluster configuration with the corresponding composition.

We observe that some individual  $a_j$  values in clusters forming  $\text{Ge}_{1-x}\text{C}_x$  and  $\text{Si}_{1-x}\text{C}_x$ , which have no significant statistical contribution for the calculated mean value, do not adhere to the obtained curve. This follows from the fact that these configurations are thermodynamically unfavored.

### 3.4.2 First-neighbor distances

In graphene, silicene and germanene all bond lengths are the same by symmetry. For the binary alloys, considering the ionic relaxation, the first-neighbor distances will change, depending very strongly on which elements are involved and on the concentration. We study the different bonds in all clusters between atoms of the same kind ( $A - A$  or  $B - B$  bonds) and different kinds ( $A - B$  bonds), with  $A, B = \text{Ge}, \text{Si}$  or  $\text{C}$ . Each cluster possesses 12 bonds between neighbor pairs. The mean first-neighbor distance  $d_{X-Y}$ , using GQCA, can be written as

$$d_{X-Y} = \frac{\sum_{j=1}^J x_j n_{(j,X-Y)} d_{(j,X-Y)}}{\sum_{j=1}^J n_{(j,X-Y)} x_j}, \quad (3.4)$$

where  $X$  and  $Y$  represents  $A$  or  $B$ ,  $d_{(j,X-Y)}$  is the mean distance of  $X - Y$  bonds in cluster class  $j$ , and  $n_{(j,X-Y)}$  is the number of  $X - Y$  bonds in class  $j$ .

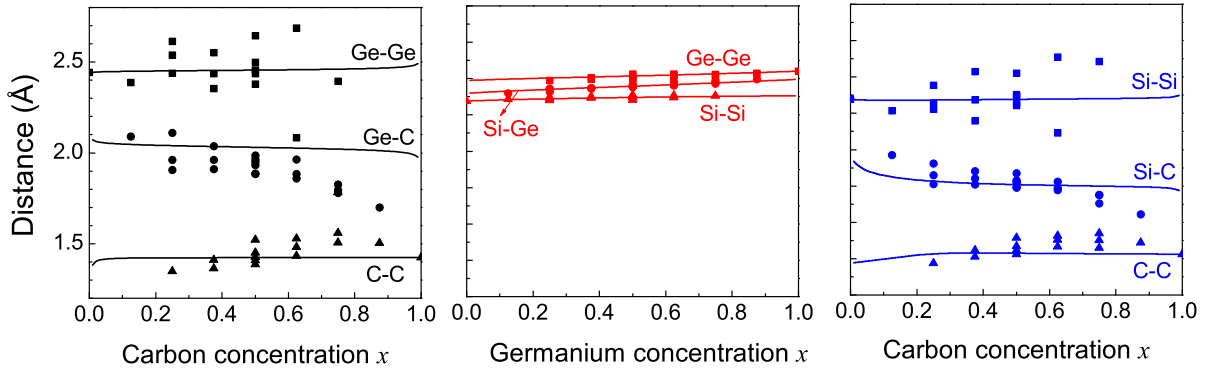


FIGURE 3.6 – The mean first-nearest neighbor distance of  $\text{Ge}_{1-x}\text{C}_x$  (black),  $\text{Si}_{1-x}\text{Ge}_x$  (red) and  $\text{Si}_{1-x}\text{C}_x$  (blue) as a function of the composition with respective mean values associated with the configuration in each cluster class. The  $A - A$ ,  $A - B$ , and  $B - B$  bond lengths are shown with triangles, circles and squares, respectively.

The results are shown in the Fig. 3.6. First, we observe three distinct bond lengths, showing that Vegard rule fails for bond lengths as observed for 3D alloys (TELES *et al.*, 2000). We also observe a tendency to keep the bond length of pure materials, the mean bond lengths of  $A - B$  bonds mainly follow the covalent radii of the constituting atoms. We find that the difference between the bond lengths in  $\text{Si}_{1-x}\text{Ge}_x$  is much smaller than in  $\text{Ge}_{1-x}\text{C}_x$  and  $\text{Si}_{1-x}\text{C}_x$ . This fact explains why  $\text{Si}_{1-x}\text{Ge}_x$  is more likely to be a more stable alloy, with weak tendency to phase separation, in contrast to  $\text{Ge}_{1-x}\text{C}_x$  and  $\text{Si}_{1-x}\text{C}_x$ . The reason is clearly related to the different sizes of the atoms in carbides  $A_{1-x}\text{C}_x$  ( $A = \text{Si}, \text{Ge}$ ) and, hence, the strong internal strains.

The obtained mean first-neighbor distances in  $\text{Si}_{1-x}\text{Ge}_x$  alloys are compared in Table 3.3 with results based on SQS for particular concentrations (PADILHA *et al.*, 2013). Apart from generally slightly larger values obtained within the SQS, the trends with the composition are quite similar.

TABLE 3.3 – Comparison of mean first-neighbor distances obtained within GQCA and SQS (PADILHA *et al.*, 2013) (in parenthesis) for  $\text{Si}_{1-x}\text{Ge}_x$  alloys at fixed compositions. All values are given in Å.

$x$	Ge-Ge	Si-Ge	Si-Si
0	-	-	2.27 (2.31)
0.265	2.40 (2.42)	2.34 (2.37)	2.29 (2.32)
0.500	2.41 (2.43)	2.36 (2.38)	2.30 (2.32)
0.735	2.42 (2.44)	2.37 (2.38)	2.30 (2.33)
1	2.44 (2.46)	-	-

Indeed, the mean bond lengths associated with different configurations in Fig. 3.6

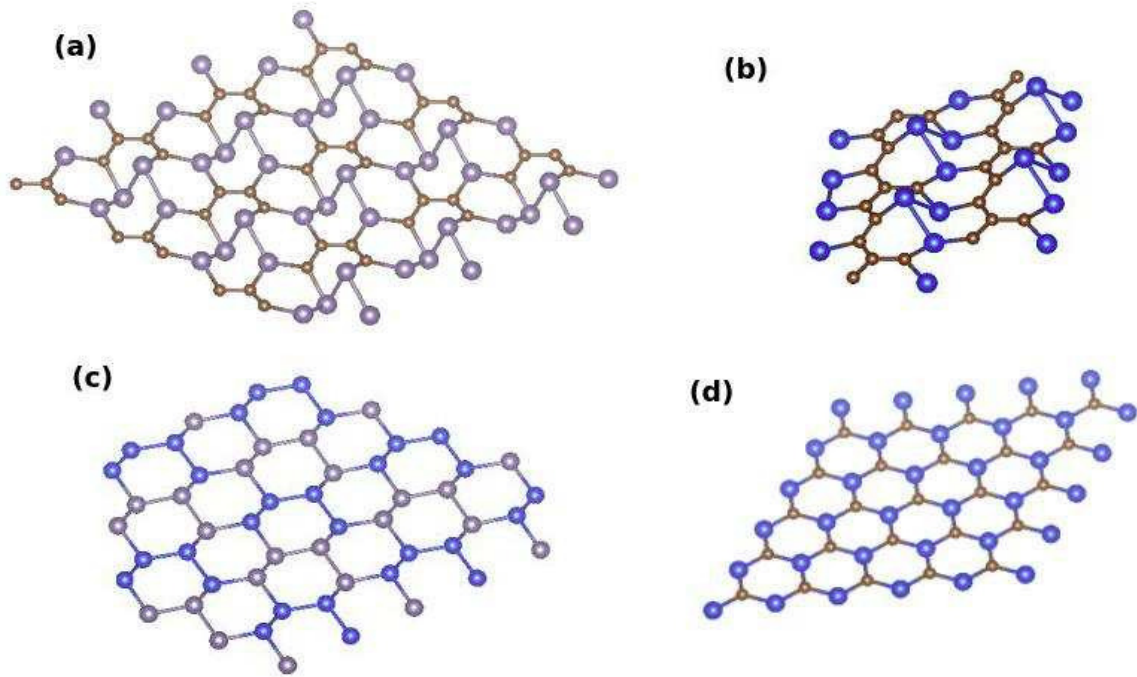


FIGURE 3.7 – Perspective views on (a)  $\text{Ge}_4\text{C}_4$  (configuration  $j = 14$ ), (b)  $\text{Si}_6\text{C}_2$  (configuration  $j = 20$ ), (c)  $\text{Si}_4\text{Ge}_4$  (configuration  $j = 11$ ), and (d)  $\text{Si}_4\text{C}_4$  (configuration  $j = 11$ ). C (Si, Ge) atoms are presented as brown (bright blue, dark blue) dots.

are more diffuse in  $\text{Ge}_{1-x}\text{C}_x$  and  $\text{Si}_{1-x}\text{C}_x$ , while the calculated first-neighbor distances do not change appreciably with the composition  $x$ . These configurations present significant deformation on the honeycomb geometry, as we can see in Figure 3.7(a) and 3.7(b). We believe that the main reason for such deformations are the big differences between the lattice parameters of graphene and the other 2D group-IV materials. For some specific configurations this effect is very pronounced, affecting not only the bond lengths, but also the layer buckling (see explanation in Fig. 3.8). As an example, the geometries of a few cluster materials  $A_{8-n_j}B_{n_j}$  are displayed in Fig. 3.7. In Figs. 3.7 (a) and 3.7(b), despite the equal numbers of atoms, the covalent radii and the bonding are different, resulting in a strong deformation and change of the atomic geometries, which are related to neighboring constitutes of the same element. On the other hand, since germanium and silicon have similar covalent radii, the honeycomb geometry of these materials does not need to deform much to accommodate a different atom, as shown in Fig.3.7(c). In Fig.3.7(d) a symmetric and equally bonded configuration ( $j = 11$ ) is shown for  $\text{Si}_{1-x}\text{C}_x$ , resulting in a completely hexagonal and planar honeycomb structure.

### 3.4.3 Buckling parameter $\Delta$

Graphene has a planar honeycomb configuration, while silicene and germanene represent a slightly buckled structure, since the bonds between atoms are not pure  $sp^2$  but correspond

to a mixed  $sp^2 - sp^3$  hybridization (ZHOU *et al.*, 2013; MATTHES *et al.*, 2013a). This hybridization is also expected for many bonds in the studied 2D alloys. As a consequence some configurations exhibit large buckling values above 1 Å (see Table 3.4). They are associated with considerable deformations of the local hexagonal structure. Indeed, the bonding hexagons in Figs. 3.7 (a) and (b) are strongly deformed.

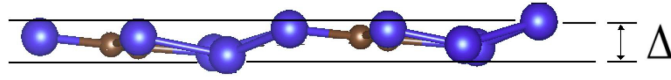


FIGURE 3.8 – Buckling amplitude of an arbitrary configuration.

The buckling amplitude in each cluster is calculated as the maximum displacement between two atoms in the direction perpendicular to the sheet plane, as shown in Fig. 3.8. Besides the individual results in Table 3.4, the mean alloy values averaged according to (2.77) are depicted in Fig. 3.9. The most stable configuration for graphene is the planar honeycomb structure, while silicene and germanene present more stable slightly buckled configurations with buckling parameters  $\Delta$  of 0.46 Å and 0.68 Å, respectively, which are in agreement with other calculations (MATTHES *et al.*, 2013a; IVANOVSKII, 2012).

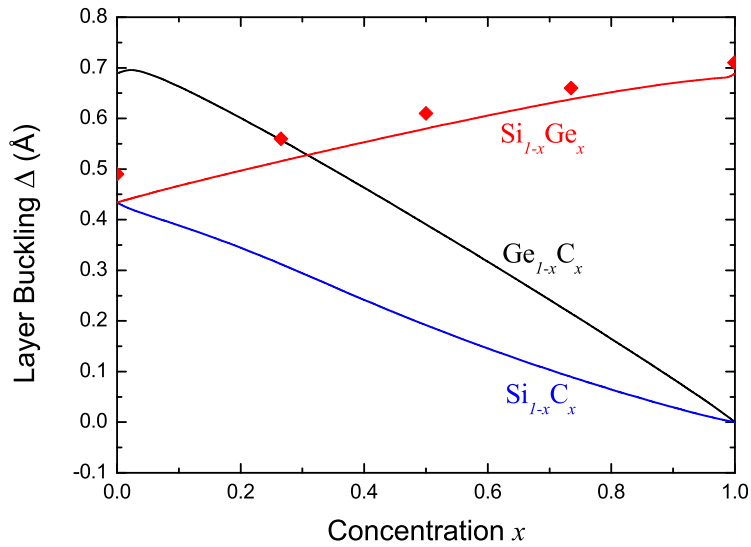


FIGURE 3.9 – Averaged buckling amplitude of  $\text{Ge}_{1-x}\text{C}_x$  (black),  $\text{Si}_{1-x}\text{Ge}_x$  (red) and  $\text{Si}_{1-x}\text{C}_x$  (blue) as a function of the composition. The red diamonds represent previously reported results for  $\text{Si}_{1-x}\text{Ge}_x$  alloys within SQS methodology (PADILHA *et al.*, 2013).

As indicated in Table 3.4, the buckling parameter varies significantly from zero to 2.81 Å. Nevertheless, when considering the cluster statistics, equation (2.77), the buckling parameter of  $\text{Ge}_{1-x}\text{C}_x$  exhibits an approximated linear behavior with composition  $x$ . This is due to the major statistical contribution of the cluster  $j = 1$ , which corresponds to

TABLE 3.4 – Buckling parameter  $\Delta_j$  of the cluster configurations  $\text{Ge}_{8-n_j}\text{C}_{n_j}$ ,  $\text{Si}_{8-n_j}\text{Ge}_{n_j}$  and  $\text{Si}_{8-n_j}\text{C}_{n_j}$ .

Class $j$	$\Delta_j$ (Å)		
	$\text{Ge}_{8-n_j}\text{C}_{n_j}$	$\text{Si}_{8-n_j}\text{Ge}_{n_j}$	$\text{Si}_{8-n_j}\text{C}_{n_j}$
1	0.69	0.43	0.43
2	0.85	0.48	0.48
3	0.71	0.51	0.08
4	1.65	0.51	0.68
5	2.81	0.51	2.70
6	1.67	0.55	1.51
7	1.49	0.55	0.57
8	2.81	0.55	1.28
9	2.01	0.59	1.79
10	2.37	0.58	1.99
11	0.00	0.58	0.00
12	0.75	0.58	0.03
13	1.91	0.58	1.70
14	2.76	0.58	2.48
15	2.15	0.62	1.91
16	0.85	0.61	0.02
17	1.36	0.62	0.55
18	0.24	0.64	0.01
19	0.00	0.65	0.00
20	1.07	0.65	2.29
21	0.06	0.67	0.01
22	0.00	0.68	0.00

pure graphene, and cluster  $j = 22$ , which corresponds to pure germanene. In  $\text{Si}_{1-x}\text{Ge}_x$  and  $\text{Si}_{1-x}\text{C}_x$ , we have contributions of different configurations. For  $\text{Si}_{1-x}\text{Ge}_x$ , a more homogeneous distribution of  $x_j$  and  $\Delta_j$  is observed (see Table 3.4), while for  $\text{Si}_{1-x}\text{C}_x$  the most significant contributions comes from the configuration  $j = 11$  and pure configurations  $j = 1$  and  $22$  as well as  $j = 6$  ( $\text{Si}_5\text{C}_3$ ). The configuration 11 represents an ordered alloy of 50% Si and 50% C atoms, for which there is a maximum number of Si-C bonds. In particular, for  $\text{Si}_{1-x}\text{Ge}_x$ , the only random alloy, the values previously obtained within SQS (PADILHA *et al.*, 2013) are depicted in Fig. 3.9 for comparison. The GQCA and the SQS results agree very well.

In Table 3.5 we compare results considering the cluster statistics and the configuration  $j = 11$ . We observe that the values for the layer buckling  $\Delta$  differ when considering or not the statistics for  $\text{Ge}_{1-x}\text{C}_x$  and  $\text{Si}_{1-x}\text{C}_x$  alloys, being comparable only for  $\text{Si}_{1-x}\text{Ge}_x$ . In the case of  $\text{Si}_{1-x}\text{C}_x$  the value depends on the growth temperature, which determines the contribution of the configurations and if the alloy consists of ordered domains. For

$\text{Ge}_{1-x}\text{C}_x$  and  $\text{Si}_{1-x}\text{Ge}_x$ , the mean buckling does not depend on the temperature. This is due to the fact that, in the first case, one has a phase separated alloy with a huge critical temperature, so for reasonable temperatures the only contributing configurations are the pure compounds, while in the second case, the dependence of the mean buckling in the random alloy is approximately linear, which will not change for a phase separated phase at low temperatures.

TABLE 3.5 – Layer bucklings ( $\Delta$ ) for the 2D  $\text{Ge}_{1-x}\text{C}_x$ ,  $\text{Si}_{1-x}\text{Ge}_x$  and  $\text{Si}_{1-x}\text{C}_x$  alloys, considering the cluster statistics ( $x = 0.5$ ) and for the configuration  $j = 11$ . Results are compared with literature data shown in parenthesis. References: (SAHIN *et al.*, 2009)<sup>a</sup>, (ZHOU *et al.*, 2013)<sup>b</sup> and (PADILHA *et al.*, 2013)<sup>c</sup>.

Alloy	$\Delta$ (Å)
$\text{Ge}_{0.5}\text{C}_{0.5}$ ( $j = 11$ )	0.00
$\text{Ge}_{0.5}\text{C}_{0.5}$	0.39
$\text{Si}_{0.5}\text{Ge}_{0.5}$ ( $j = 11$ )	0.58(0.55 <sup>a</sup> ,0.579 <sup>b</sup> )
$\text{Si}_{0.5}\text{Ge}_{0.5}$	0.58 (0.61 <sup>c</sup> )
$\text{Si}_{0.5}\text{C}_{0.5}$ ( $j = 11$ )	0.00 (0.00 <sup>a</sup> )
$\text{Si}_{0.5}\text{C}_{0.5}$	0.19

### 3.5 Electronic Properties

The ability to obtain customized electronic properties, such as the energy bandgap, is the main concept of the bandgap engineering. The GQCA statistical approach allows the prediction of the average band gaps for the whole composition range for alloyed systems considering a growth temperature  $T$ . The obtained fundamental energy gaps  $E_g$  are listed in table 3.6 for the random alloys  $\text{Ge}_{1-x}\text{C}_x$ ,  $\text{Si}_{1-x}\text{Ge}_x$  and  $\text{Si}_{1-x}\text{C}_x$  at the growth temperature of  $T=800$  K. In order to simulate the quasiparticle shifts we apply the DFT-1/2 approach (FERREIRA *et al.*, 2008; FERREIRA *et al.*, 2011) (see section 2.1.6). Considering 3D materials the DFT-1/2 method predicts energy band gaps in very good agreement with experimental data, including alloys (PELA *et al.*, 2015). For 2D materials it was recently applied to 2D allotropes of group-IV materials giving results in reasonable agreement when compared with gaps derived by hybrid functionals (MATUSALEM *et al.*, 2015).

It is worth to point out that the alloys may exhibit phase separation, or even ordered geometries. That means that the result for the 50% compositions can be different from the values predicted for the ordered cases (SUZUKI; YOKOMIZO, 2010). This is the case for  $\text{Ge}_{0.5}\text{C}_{0.5}$ , for which the predicted values for the ordered configuration 11 is 2.07 eV, while the predicted energy gap of the random alloy (Fig. 3.10) remains extremely

TABLE 3.6 – Energy gap  $E_{g,j}$  of the cluster configurations  $\text{Ge}_{8-n_j}\text{C}_{n_j}$ ,  $\text{Si}_{8-n_j}\text{Ge}_{n_j}$  and  $\text{Si}_{8-n_j}\text{C}_{n_j}$ . Metallic configurations are indicated by ‘metal’.

Class	$E_{g,j}^{GGA}$ (eV)			$E_{g,j}^{GGA-1/2}$ (eV)		
	$\text{Ge}_{8-n_j}\text{C}_{n_j}$	$\text{Si}_{8-n_j}\text{Ge}_{n_j}$	$\text{Si}_{8-n_j}\text{C}_{n_j}$	$\text{Ge}_{8-n_j}\text{C}_{n_j}$	$\text{Si}_{8-n_j}\text{Ge}_{n_j}$	$\text{Si}_{8-n_j}\text{C}_{n_j}$
1	0.000	0.000	0.000	0.000	0.000	0.000
2	metal	0.003	0.202	metal	0.003	0.206
3	metal	0.000	0.000	metal	0.000	0.000
4	metal	0.005	0.485	metal	0.009	1.027
5	metal	0.003	metal	metal	0.003	metal
6	1.442	0.007	1.832	1.930	0.001	2.396
7	0.446	0.005	0.561	0.838	0.007	0.563
8	1.095	0.003	0.020	1.059	0.003	metal
9	metal	0.008	metal	metal	0.006	metal
10	metal	0.004	metal	metal	0.005	0.071
11	2.072	0.007	2.534	2.535	0.014	3.061
12	metal	0.008	0.003	metal	0.009	0.090
13	1.089	0.006	1.374	0.610	0.011	1.017
14	metal	0.000	metal	metal	0.000	0.159
15	0.529	0.005	0.563	0.540	0.006	0.322
16	1.352	0.005	1.429	1.535	0.010	1.678
17	0.619	0.005	0.579	0.788	0.008	0.677
18	0.000	0.000	0.000	metal	0.000	metal
19	0.943	0.002	1.295	1.411	0.009	1.573
20	metal	0.006	0.079	metal	0.005	0.312
21	0.674	0.001	0.766	0.840	0.001	0.932
22	0.000	0.000	0.000	0.000	0.000	0.000

small with 0.04 eV. This is due to the fact that, in spite of non-zero values for different concentrations, the only two configurations that have a significant statistical contribution are those corresponding to pure graphene and pure germanene, which have both zero energy gaps. This is a good example of how mandatory is the use of statistics, showing that values previously obtained for a special arrangement of the C and Ge atoms (SUZUKI; YOKOMIZO, 2010; SAHIN *et al.*, 2009) are only valid for an energetically unfavorable distribution of the atoms.

For  $\text{Si}_{1-x}\text{Ge}_x$ , which can be widely mixed, but especially  $\text{Si}_{1-x}\text{C}_x$  we see from Fig. 3.10 that the values of  $E_g$  strongly deviate from the linear behavior, but can be well described by a parabolic one. We apply the usual formula for the average energy gap  $E_g$  versus average composition  $x$  as well known from semiconducting alloys (CHEN; SHER, 1995), where the deviations from the linear variation are described by a bowing parameter  $b$  as

$$E_g(x, T) = xE_g^A + (1-x)E_g^B - bx(1-x). \quad (3.5)$$

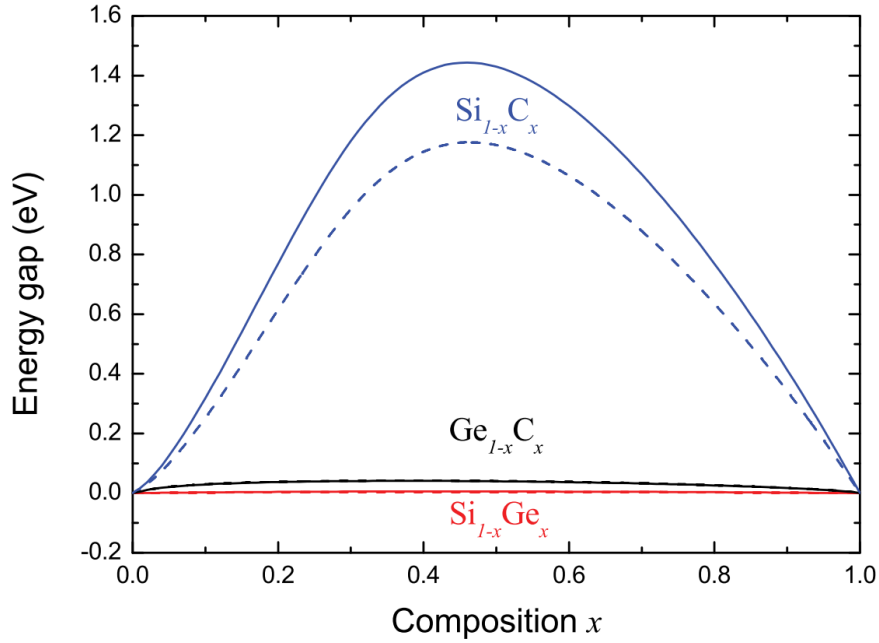


FIGURE 3.10 – The gap curves of random alloys of  $\text{Ge}_{1-x}\text{C}_x$  (black),  $\text{Si}_{1-x}\text{Ge}_x$  (red) and  $\text{Si}_{1-x}\text{C}_x$  (blue) as a function of the composition for  $T=800\text{K}$ . Full line (dashed) curves correspond to results obtained within the GGA-1/2 (GGA) approach.

Germanene presents a metallic electronic band structure in the planar honeycomb geometry without buckling but near  $K$  in the BZ Dirac cones with zero gap when one considers the buckling effect, as we did. Silicene, on the other hand, present Dirac cones with zero gap independently if one considers the layer buckling or not (CAHANGIROV *et al.*, 2009). Thus, here  $E_g^A = E_g^B = 0$  holds because all group-IV-derived graphene-like systems possess a vanishing fundamental gap at  $K$  or  $K'$  in the Brillouin Zone, at least neglecting spin-orbit interaction (KOKOTT *et al.*, 2014; MATTHES *et al.*, 2013b). In contrast to 3D semiconductors an anti-bowing  $b < 0$  is found in Fig. 3.10. For  $\text{Si}_{1-x}\text{Ge}_x$  ( $\text{Ge}_{1-x}\text{C}_x$ ) we calculate  $b = -0.02$  ( $-0.18$ ) eV for the parabolic fit, whereas for  $\text{Si}_{1-x}\text{C}_x$ ,  $b = -4.38$  eV indicating the large gaps for SiC-like configurations. While  $\text{Si}_{1-x}\text{Ge}_x$  and  $\text{Ge}_{1-x}\text{C}_x$  alloys present energy gaps about a few meV, the  $\text{Si}_{1-x}\text{C}_x$  alloys possesses large direct energy gaps that can be very interesting for optoelectronic applications.

In order to compare our values for  $\text{Si}_{1-x}\text{C}_x$  and  $\text{Ge}_{1-x}\text{C}_x$  with results previously obtained, we need to consider only the energy gap of configuration 11. The  $E_g$  values for this configuration, as well as, considering the statistics are shown in Table 3.7. A nice agreement is observed among our results and the ones obtained considering LDA or GGA (GORI *et al.*, 2012; SAHIN *et al.*, 2009; LIN *et al.*, 2013; MIRO *et al.*, 2014), while a qualitative agreement is verified with other calculations (SUZUKI; YOKOMIZO, 2010; GORI *et al.*, 2012; SAHIN *et al.*, 2009; MIRO *et al.*, 2014). The latter case is due the use of different (approximate) quasiparticle corrections (QPCs) due to the spatial non-locality of the XC potential, these calculations obtain absolute gap values for  $\text{Si}_{1-x}\text{C}_x$  and  $\text{Ge}_{1-x}\text{C}_x$  about 1

eV higher than the values in Table 3.7, as one can observe. We also made a simulation for a generalized Kohn-Sham scheme with a hybrid functional HSE06 (HEYD *et al.*, 2003; HEYD *et al.*, 2006), which has been successfully applied to band structures of silicene, germanene, and graphene (MATTHES *et al.*, 2013b) and gives rise to a gap value  $E_g = 3.40$  eV and 2.87 eV for ordered  $\text{Si}_{0.5}\text{C}_{0.5}$  and  $\text{Ge}_{0.5}\text{C}_{0.5}$  arrangements, respectively. The obtained energy gap for a ordered  $\text{Si}_{0.5}\text{C}_{0.5}$  phase is very close to the experimental optical gap measurement made by S. S. Lin, obtained by photoluminescence of ultrathin SiC nanosheets (LIN, 2012). However, it is important to emphasize that the larger localization and modification of screening due to low-dimensionality in 2D materials lead to great exciton binding energies and intense self-energy interactions that may not be fully captured by the hybrid functional picture. A partial compensation of these two effects was reported in other 2D materials (WIRTZ *et al.*, 2006; YANG *et al.*, 2009), explaining why the energy gap obtained within independent quasi-particle picture and hybrid functional obtained within is comparable with the  $\text{Si}_{0.5}\text{C}_{0.5}$  optical gap, while a GW ( $\text{GW}_0$ ) calculation leads to quasiparticle energy gaps of 4.42 eV (4.19 eV) (HSUEH *et al.*, 2011; SAHIN *et al.*, 2009).

TABLE 3.7 – Energy gaps ( $E_g$ ) for the 2D  $\text{Ge}_{1-x}\text{C}_x$ ,  $\text{Si}_{1-x}\text{Ge}_x$  and  $\text{Si}_{1-x}\text{C}_x$  alloys, considering the cluster statistics ( $x = 0.5$ ), and for the configuration  $j = 11$ . The values with the symbol  $\dagger$  were calculated considering gap corrections. The DFT-1/2 self-energy corrections for alloy statistics were obtained with transferability arguments, while the results for the ordered configurations ( $j = 11$ ) were optimized for these specific arrangements.

Alloy	$E_g$ (eV)		
	Present work	Other calc.	Exp.
	GGA	GGA-1/2 (HSE06)	
$\text{Ge}_{0.5}\text{C}_{0.5}$	0.041	0.041	
$\text{Si}_{0.5}\text{Ge}_{0.5}$	0.004	0.005	0.010 <sup>c</sup>
$\text{Si}_{0.5}\text{C}_{0.5}$	1.166	1.429	
$\text{Ge}_{0.5}\text{C}_{0.5}$ ( $j = 11$ )	2.07	3.87 (2.87)	2.09 <sup>a</sup> , 2.26 <sup>h</sup> 3.16 <sup>†,b</sup> , 3.37 <sup>†,h</sup> , 3.83 <sup>†,a</sup>
$\text{Si}_{0.5}\text{Ge}_{0.5}$ ( $j = 11$ )	0.007	0.01	0.02 <sup>a</sup> , 0.015 <sup>i</sup> 0.275 <sup>†,b</sup>
$\text{Si}_{0.5}\text{C}_{0.5}$ ( $j = 11$ )	2.53	4.38 (3.40)	2.52 <sup>a</sup> , 2.55 <sup>d</sup> , 2.5 <sup>e</sup> , 2.56 <sup>f</sup> 2.57 <sup>h</sup> , 4.19 <sup>†,a</sup> , 4.42 <sup>†,j</sup> 3.53 <sup>†,b</sup> , 3.63 <sup>†,d</sup> , 3.7 <sup>†,f</sup> , 3.88 <sup>†,h</sup>

<sup>a</sup>Ref. (SAHIN *et al.*, 2009), <sup>b</sup>Ref.(SUZUKI; YOKOMIZO, 2010), <sup>c</sup>Ref.(PADILHA *et al.*, 2013),

<sup>d</sup>Ref.(MIRO *et al.*, 2014), <sup>e</sup>Ref. (LIN *et al.*, 2013), <sup>f</sup>Ref.(GORI *et al.*, 2012), <sup>g</sup>Ref.(LIN, 2012), <sup>h</sup>Ref. (LU *et al.*, 2012), <sup>i</sup>Ref.(JAMDAGNI *et al.*, 2015), and <sup>j</sup> Ref.(HSUEH *et al.*, 2011).

DFT-1/2 method was recently applied with success to 2D allotropes of group-IV materials (MATUSALEM *et al.*, 2015). In 3D systems the transferability of self-energy corrected pseudopotentials between similar systems is verified, which is still valid for 2D systems according to our current investigations on DFT-1/2 performance on this class

of materials (GUILHON *et al.*, To be published). For some alloyed systems, VBM and CBM states exhibit significant projections on different orbitals and elements, which makes the DFT-1/2 application not straightforward. To overcome this obstacle, the removal of a fraction of half-electron proportionally to VBM and CBM states projections on atomic orbitals was proposed (ATAIDE *et al.*, 2017). As a first approximation, we assumed the carbon, silicon and germanium corrected pseudopotential transferability from LHD structures to our 2D alloys (MATUSALEM *et al.*, 2015; GUILHON *et al.*, 2015). More accurate results can be obtained by a deeper investigation of VBM and CBM orbital characters, accompanied by respective CUT parameters optimizations, for each cluster configuration  $j$  of each material.

DFT-1/2 results were optimized to ordered  $\text{Si}_{0.5}\text{C}_{0.5}$  and  $\text{Ge}_{0.5}\text{C}_{0.5}$  cluster configurations ( $j = 11$ ) considering valence and conduction corrections. The top of valence band is associated with carbon  $p_z$  orbitals, while the bottom of the conduction band is associated with silicon and germanium  $p_z$  orbitals, respectively. The application of the optimized self-energy potentials to this ordered arrangements leads to quasiparticle energy gaps of 4.38 eV and 3.87 eV, respectively, which are in very good agreement to GW calculations available in literature (SAHIN *et al.*, 2009; HSUEH *et al.*, 2011).

As one observes in Table 3.7 and Fig. 3.10, the calculated energy gaps are underestimated when quasiparticle corrections are not taken into account, as expected. However, the Kohn-Sham gaps still give correct tendencies with the composition  $x$ , so qualitative analysis and inferences can still be done. Another interesting feature of the  $\text{Si}_{1-x}\text{C}_x$  alloys is the growth temperature dependence of the computed gap curves shown in Fig.3.11 (a). The gap curves vary substantially with the growth temperature. For low temperatures, the inclusion of the configuration 11 is favored, resulting in a wider energy gap, since this configuration has a gap value of 2.53 eV in DFT-GGA. With increasing temperature other configurations begin to contribute resulting in the temperature dependence of  $E_g$ , and the maximum of the gap curves are shifted to lower average composition  $x$  as temperature increases. In Fig. 3.11 (b) we show the maximum energy gap as a function of the growth temperature. It makes more obvious the temperature dependence of the average gap of SiC. The value for the ordered configuration 11 at  $T = 0\text{K}$  is reduced to about 1 eV for  $T = 1000\text{K}$ . The results can be well fitted by the expression

$$E_g^{\max}(T) = E_g^{\max}(0)e^{-T/T_{c,ord}}, \quad (3.6)$$

with  $T_{c,ord} = (1004 \pm 22)\text{K}$ , which agrees with the temperature of about  $T = 1000\text{K}$  for which the alloy is almost random as shown previously accordingly to the SRO parameter  $L$  in Fig.3.3. Thus, this temperature dependence is mainly a consequence of increasing probabilities for other atomic configurations beyond the  $j = 11$  one.

The situation for the other carbide alloy is totally different. For  $\text{Ge}_{1-x}\text{C}_x$ , there is a clear phase separation into pure graphene-like and pure germanene-like configurations, while all other configurations do not give rise to significant contributions. In contrast, for  $\text{Si}_{1-x}\text{Ge}_x$ , from Fig. 3.10, we observe that all clusters appear and contribute to the statistics. Nevertheless, the resulting average gaps remain about few meV because of the small cluster gaps as listed in Table 3.6.

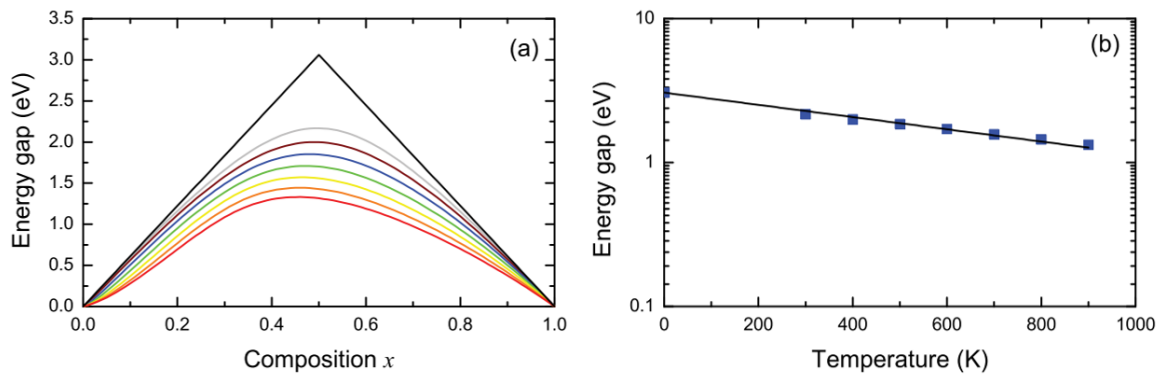


FIGURE 3.11 – (a) The gap curves of  $\text{Si}_{1-x}\text{C}_x$  for different temperatures. The black line corresponds to ordered phase 11. (b) The maximum energy gap obtained for the  $\text{Si}_{1-x}\text{C}_x$  alloy as a function of the growth temperature. The full line represent the best fit of the data using Eq. (3.6).

# 4 $(\text{BN})_{1-x}(\text{C}_2)_x$ alloy

## 4.1 Introduction

In chapter 3, one can observe a great role of strong deformations of the honeycomb structure in the total energies of the three considered binary alloys obtained from group-IV elements. This effect is very dramatic in  $\text{Si}_{1-x}\text{C}_x$ ,  $\text{Ge}_{1-x}\text{C}_x$ , where the difference between atomic radii is not negligible, while  $\text{Ge}_{1-x}\text{Si}_x$  is a random alloy and the honeycomb structure is not severely deformed by the permutation of the atoms that occupy each atomic site.

This effect should not be very strong in materials with similar atomic sizes, such as boron, carbon, and nitrogen, for example. Based on these observations, a 2D alloy formed by graphene and *h*-BN is a natural choice for study. Both materials have the same honeycomb structure with a constant mismatch of only 2% (LIU, 2013). Since graphene is a conducting material and *h*-BN is an insulator with a wide bandgap, an alloyed system of this materials can, in principle, exhibit conducting, semiconducting or insulator behavior depending on its composition.

Recently, it has been demonstrated that  $(\text{BN})_{1-x}(\text{C}_2)_x$  layers can be synthesized by Chemical Vapor Deposition (CVD) (CI, 2010; CHANG *et al.*, 2013) or via chemical substitution of C with *h*-BN in graphene (GONG *et al.*, 2014). However, the distributions of atoms in these alloys are far away from perfectly random, instead exhibit phase separation resulting in *h*-BN-rich and graphene-rich domains (YUGE, 2009; CI, 2010; CHANG *et al.*, 2013).

The alloy thermodynamics determines the miscibility of the combined materials, thereby also favor some specific atomic arrangements, which might have a strong influence on the electronic and optical properties of the alloy with a given composition  $x$ . Depending on the size of the domains produced in the phase segregation process, their effect on the observed properties of  $(\text{BN})_{1-x}(\text{C}_2)_x$  might be different. According to Ci *et al.* (CI, 2010), for domain sizes smaller than 2-3 nm, the film behaves like a BN-C alloy, with a band gap equal to the average gap of the two components, while domain sizes larger than 2-3 nm can lead to carrier localization and exhibit the electronic and optical properties of both materials.

Previous theoretical approaches have been used only to predict phase separation (YUGE, 2009; MAZZONI *et al.*, 2006; AZEVEDO, 2006), but its effects on electronic and optical properties is still an open question. Therefore, the combination of a quasiparticle electronic structure method with a statistical approach that takes into account the segregation and composition fluctuations should give rise to novel results for the prediction of the fundamental energy gap and related electronic as well as optical properties.

## 4.2 Cluster expansion and configurational counting

We chose the same supercell used for  $\text{Si}_{1-x}\text{C}_x$ ,  $\text{Ge}_{1-x}\text{C}_x$  and  $\text{Ge}_{1-x}\text{Si}_x$  alloy. Since this alloy shares the same symmetry as the previous alloys, the same procedure to reduce the total number of configurations to a set of  $J$  non-equivalent cluster configurations by symmetry considerations can be used. However, since we have a third atom in the alloy, the initial number of configurations increases from  $2^8 = 258$  up to  $3^8 = 6561$ .

To deal with this problem, only clusters  $\text{B}_{n-n_j}\text{N}_{n-n_j}\text{C}_{2n_j}$  ( $n_j = 0, 1, 2, 3, 4$  and  $2n = 8$ ) are considered. The  $2n = 8$  atomic sites can be randomly occupied by boron, carbon or nitrogen atoms, covering all the configurations with equal numbers of boron and nitrogen atoms. Besides C-C, B-N, C-B and C-N bonds, also B-B and N-N ones are allowed. This sample set result in 1107 possible atomic configurations, which can be arranged into  $J = 43$  classes with different degeneracies considering the symmetry equivalence of different cluster configurations. Such systems with equal numbers of boron and nitrogen atoms are synthesized by CVD growth using ammonia borane  $\text{NH}_3\text{-BH}_3$  as a single precursor of boron and nitrogen atoms (CI, 2010) or controlling the flux of distinct boron and nitrogen precursors (UDDIN *et al.*, 2015). The configuration cluster classes are listed in the table 4.1

Since the ratio between the number of boron and nitrogen atoms is fixed at the unity, the alloy composition is fully described the carbon fraction  $x$  and the GQCA formalism for ternary alloys can be applied to this system, as a particularization for a pseudo-binary alloy as explained in section 2.2.3.

The main difference between this set of configurations and the ones considered in the previous chapter is that in the  $(\text{BN})_{1-x}(\text{C}_2)_x$  alloys all the possible permutations between boron and nitrogen atoms are allowed. Therefore we have six different clusters configurations at  $x = 0$ , among which the ordered  $h$ -BN configuration is the most stable. One can verify by direct inspection of the equation 2.76 that the calculated set of occurrence probabilities  $x_j$  within the GQCA formalism are invariant by considering different energy values to represent the system at  $x = 0$  composition in the excess cluster energies  $\Delta\varepsilon_j$  calculation. The effect of considering a different total energy reference in this composition is incorporated by a new value for the Lagrange multiplier  $\lambda$  in the equation 2.76, which is

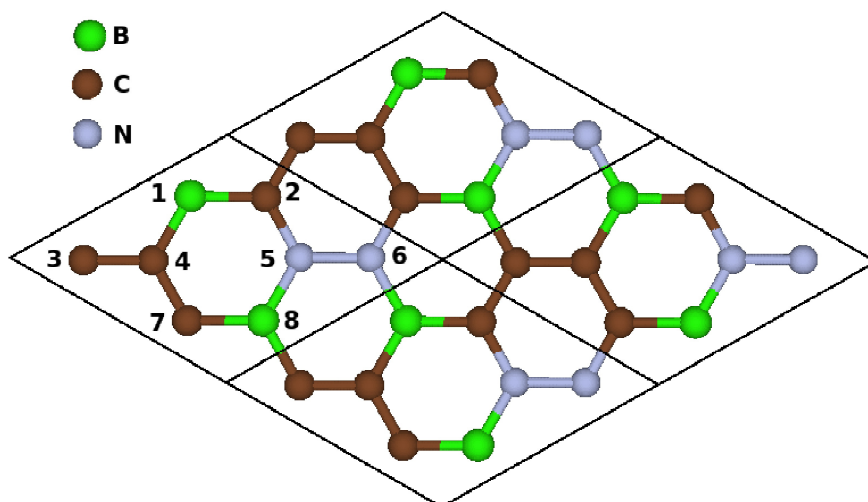


FIGURE 4.1 – An example of a 2D periodic system derived from one supercell configuration. B, C and N atoms are represented as green, brown and gray dots, respectively. Each configuration is labelled according to the represented numeration. The represented configuration is labelled as BCCCNNCB following the order of the atoms that stay in the 12345678 sites, respectively.

still determined by the average composition constraint given by equation 2.72.

TABLE 4.1 –  $(\text{BN})_{1-x}(\text{C}_2)_x$  non-equivalent cluster classes and their degeneracies  $g_j$ . The numeration of sites for cluster labelling is depicted in Fig. 4.1.

$j$	$g_j$	Label	$j$	$g_j$	Label	$j$	$g_j$	Label
1	1	CCCCCCCC	16	24	CCCNNBCB	31	48	CBCNNBBN
2	24	CCCCCBN	17	48	CCBBNINN	32	24	CBCNNBNB
3	24	CCCCBCN	18	12	CCBBNICC	33	24	CBBBNINC
4	24	CCCCBBNN	19	48	CCBBNNBN	34	24	CBBNBNCN
5	12	CCCCBNBN	20	12	CCBNBNCC	35	48	CBBNNBNC
6	24	CCCBCBNN	21	24	CCBNBNBN	36	24	CBBNNNCB
7	24	CCCBCNBN	22	24	CCBNBNNB	37	8	CBNBNBNC
8	24	CCCBBCNN	23	12	CCBNNBCC	38	6	BBBBNINN
9	24	CCCBBNCN	24	48	CCBNNBBN	39	8	BBBNBINN
10	8	CCCBNCCC	25	48	CCBNNNBB	40	24	BBBNBNBN
11	48	CCCBNCBN	26	12	CBCBCNCN	41	24	BBBNNNBN
12	48	CCCBNCNB	27	24	CBCBBNIN	42	6	BBNNNNBB
13	48	CCCBNBCN	28	24	CBCBNBNN	43	2	BNBNBNBN
14	48	CCCNBBCN	29	48	CBCNBBNN			
15	24	CCCNNCBB	30	24	CBCNBNBN			

### 4.3 Phase stability and composition fluctuation

In a macroscopic alloy the mixing free energy  $\Delta F(x, T)$  is determined by the interplay between configurational entropy and internal energy resulting in the temperature and composition dependent cluster probabilities  $x_j(x, T)$ . Thereby, the most favorable local arrangement of atoms is influenced by the alloy thermodynamics, favoring some cluster configurations with low excess energies in preference of others. The excess energy and the statistical contribution of each cluster at  $x = 0.5$  and  $T = 1600\text{K}$  are listed in Table 4.2.

TABLE 4.2 – Excess energy  $\Delta\varepsilon_j$  (eV) and statistical contribution  $x_j$  ( $x = 0.5, T = 1600\text{K}$ ) of the cluster configurations of the  $\text{C}_x(\text{BN})_{1-x}$  alloy.

Class $j$	$\Delta\varepsilon_j$ (eV)	$x_j$	Class $j$	$\Delta\varepsilon_j$ (eV)	$x_j$	Class $j$	$\Delta\varepsilon_j$ (eV)	$x_j$
1	0.00	0.057	16	4.20	0.025	31	6.92	0.004
2	2.10	0.183	17	7.79	0.002	32	5.00	0.011
3	3.31	0.061	18	8.49	0.000	33	11.43	0.000
4	6.20	0.004	19	10.41	0.000	34	7.68	0.001
5	1.87	0.102	20	4.31	0.011	35	6.96	0.004
6	5.21	0.010	21	1.97	0.167	36	9.41	0.000
7	5.41	0.008	22	10.11	0.000	37	3.42	0.015
8	4.95	0.012	23	3.98	0.015	38	14.25	0.000
9	4.06	0.028	24	5.60	0.012	39	12.29	0.000
10	3.22	0.022	25	8.16	0.001	40	11.66	0.000
11	7.36	0.003	26	6.59	0.001	41	7.45	0.001
12	3.11	0.132	27	9.01	0.000	42	6.58	0.001
13	6.30	0.007	28	7.34	0.001	43	0.00	0.074
14	6.55	0.006	29	11.23	0.000			
15	5.31	0.009	30	5.06	0.010			

The plot of the excess energies  $\Delta\varepsilon_j$  of the 43 considered cluster configurations as a function of the carbon concentration is depicted in Fig. 4.2. We verify that the configurations without B-B and N-N are strongly energetically favored. The most energetically favorable configurations are BNBNNBN ( $n_j=0$ ), CCBNNBNBN ( $n_j=1$ ), CCCBNBN ( $n_j=2$ ) and CCCCCC ( $n_j=4$ ). They show a strong tendency to eliminate B-B and N-N bonds and to maximize the number of C-C and B-N bonds, as reported in previous theoretical (YUGE, 2009) and experimental (HUANG *et al.*, 2013) works. Consequently, the cluster configurations which represent almost a mixture of *h*-BN and graphene are energetically favored. This fact explains a very strong tendency of the mixed system to segregate into graphene and *h*-BN domains as observed experimentally (CI, 2010).

Fig.4.3 depicts the resulting phase diagram, in which we observe a huge critical temperature  $T_c = 5200$  K, significantly above typical growth temperatures. This temperature is comparable to the result of  $T_c = 4500$  K calculated using Monte Carlo simulations, neglecting the lattice vibrations, which is much higher than the expected melting point

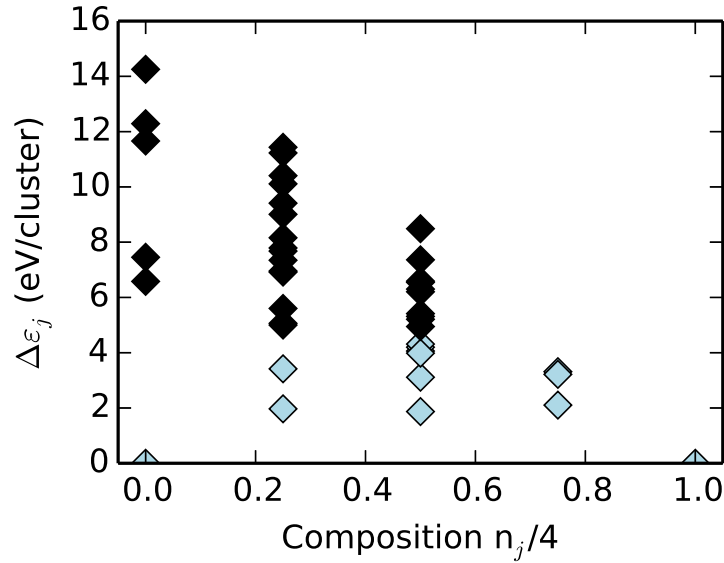


FIGURE 4.2 – (Color online) Excess energies  $\Delta\varepsilon_j$  of each atomic configuration as function of the number of carbon atoms  $n_j$ . The black diamonds represent the configurations with mainly B-B and N-N bonds, while the light blue diamonds represent the complementary subset of the possible configurations.

of the alloy (YUGE, 2009). The phase diagram in Fig. 4.3 shows that random alloys can only exist for extremely small C or  $h$ -BN concentrations and that carbon-rich alloys are more thermodynamically favored than  $h$ -BN-rich ones. For  $T=1600$  K, a typical growth temperature, we predict a very small carbon solubility in  $h$ -BN of  $x_C = 0.028$  and a  $h$ -BN solubility in graphene of  $x_{BN} = 0.042$ . These results are in very good agreement with the experimental values  $x_C^{exp} = 0.032$  and  $x_{BN}^{exp} = 0.05$  reported by Uddin *et al.* (UDDIN *et al.*, 2014; UDDIN *et al.*, 2015).

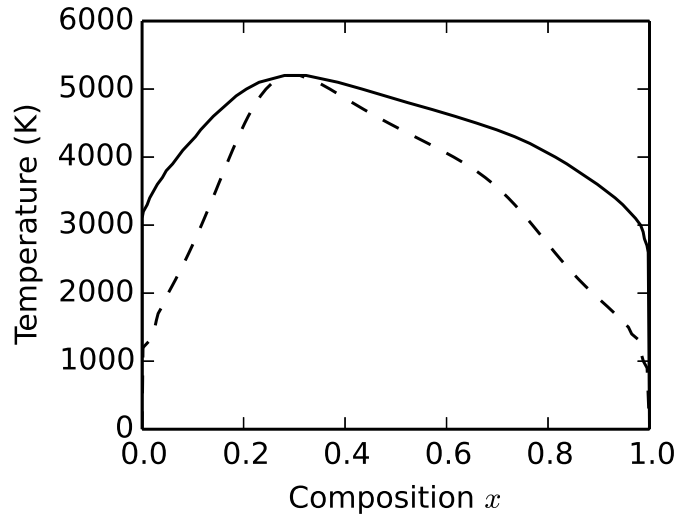


FIGURE 4.3 – The  $T$ - $x$  phase diagram of  $(\text{BN})_{1-x}(\text{C}_2)_x$ . The binodal (spinodal) curve is represented by the full (dashed) line.

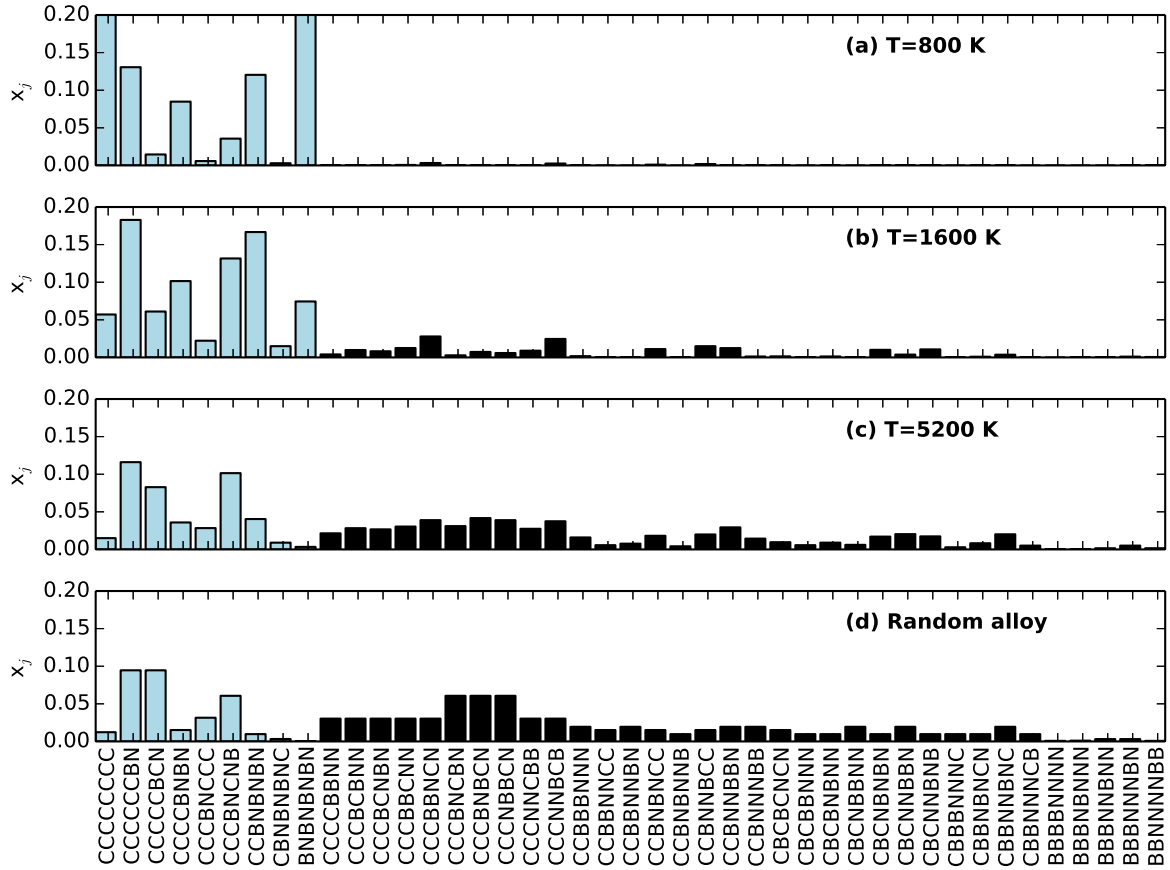


FIGURE 4.4 – The probability histogram of all cluster configuration classes of  $(\text{BN})_{1-x}(\text{C}_2)_x$  alloy with  $x=0.5$  at 800 K (a), 1600 K (b) and 5200 K (c) within GQCA formalism. Histogram obtained from a random alloy, more precisely an ideal solid solution, is depicted in (d). The black bars represent the configurations with B-B and N-N bonds, while the light blue bars represent the complementary configuration subset S.

The probabilities  $x_j(x, T)$  for the realization of a certain atomic configuration  $j$  depend mainly on the excess energies for lower temperatures. For higher temperatures the entropy term in the mixing free energy, given by equation 2.69, becomes more important. The distribution of occurrence probability among the 43 clusters starts to resemble the random distribution and more energetic configurations can be statistically relevant depending on the considered growth temperature  $T$ . This behavior is depicted by bar histograms in Fig. 4.4 for a average composition  $x = 0.5$  and increasing temperature  $T$ . In agreement with the excess energies, for lower temperatures the probability to find a cluster with B-B and N-N bonds is vanishing small. For such temperatures, mainly the cluster classes with C-C, C-N, C-B, and B-N in the subset S should be realized. Only for temperatures close to the critical one, also significant contributions from clusters with B-B and N-N bonds may occur. In this case, the cluster distribution approaches the probabilities predicted for a random alloy, i.e., an ideal solution.

The similarity between the GQCA probability  $x_j(x, T)$  and the probabilities of cluster

$j$  in an ideal solid solution  $x_j^0(x)$  can be measured by the Kullback-Leibler divergence  $D_{KL}(x_j|x_j^0)$  given in equation 2.86. This quantity rules the deviation of the actual mixing entropy from the ideal system. The Fig. 4.5 shows the behavior of the KL divergence between the distributions at average composition at  $x=0.25, 0.5$ , and  $0.75$  as a function of the temperature. The maximum divergence value at low temperatures corresponds to the occurrence of only graphene and ordered  $h$ -BN clusters. As the temperature increases the two materials start to alloy and divergence decays. The assumption of a random atomic distribution in a  $(\text{BN})_{1-x}(\text{C}_2)_x$  alloy is hardly justified for typical growth temperatures. This is in agreement with the phase diagram in Fig.4.3 and the reported alloy tendency for phase segregation.

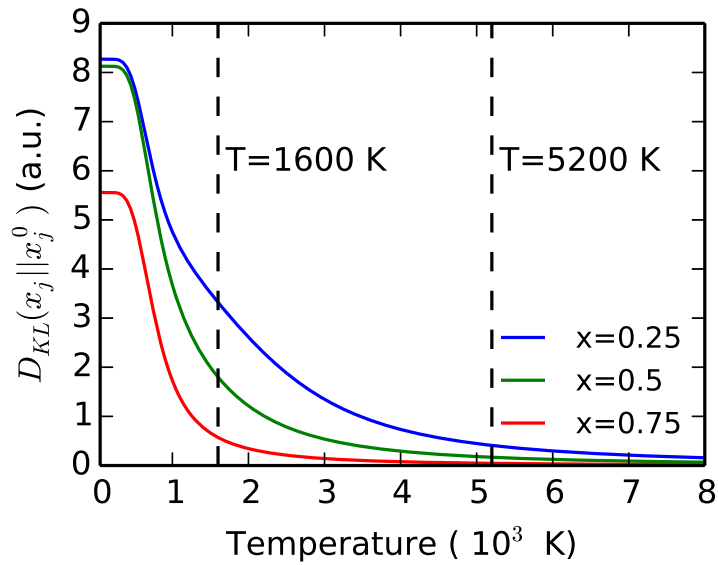


FIGURE 4.5 – Kullback-Leibler divergence between the random alloy and GQCA probability distributions as a function of temperature for different compositions  $x=0.25, 0.5$ , and  $0.75$ . Small divergence values indicate similar probability distributions. Adopted growth temperature  $T$  for alloy property estimations and critical temperature  $T_c$  are highlighted.

## 4.4 Structural properties

Considering equation 2.77 and the cluster occurrences probabilities calculated from the minimization of the free energy for given  $T$  and  $x$ , we can predict the alloy properties in the whole range of concentrations based on the properties  $p_j$  calculated for each cluster class. We perform our calculations at  $T = 1600$  K, the growth temperature found in literature (UDDIN *et al.*, 2014; RAIDONGIA *et al.*, 2010).

In the Fig. 4.6 one observes the behavior of the lattice parameter of the 2D hexagonal structure as a function of the carbon concentration. The most carbon-rich cluster with the smallest lattice constants dominate the average behavior in the alloy. The cluster

TABLE 4.3 – Layer buckling  $\Delta_j$  and lattice constant  $a_j$  of each cluster configuration class  $j$  of the  $\text{C}_x(\text{BN})_{1-x}$  alloy.

Class $j$	$\Delta_j(\text{\AA})$	$a_j(\text{\AA})$	Class $j$	$\Delta_j(\text{\AA})$	$a_j(\text{\AA})$	Class $j$	$\Delta_j(\text{\AA})$	$a_j(\text{\AA})$
1	0.00	2.469	16	0.00	2.504	31	0.00	2.53
2	0.00	2.487	17	0.01	2.55	32	0.00	2.524
3	0.00	2.492	18	0.00	2.517	33	0.05	2.521
4	0.00	2.520	19	0.02	2.536	34	0.61	2.505
5	0.00	2.497	20	0.00	2.508	35	0.00	2.527
6	0.00	2.523	21	0.01	2.510	36	0.00	2.545
7	0.00	2.505	22	0.02	2.552	37	0.01	2.511
8	0.00	2.524	23	0.00	2.504	38	0.03	2.47
9	0.00	2.510	24	0.01	2.523	39	1.00	2.466
10	0.01	2.490	25	0.01	2.534	40	0.00	2.566
11	0.00	2.517	26	0.00	2.508	41	0.01	2.562
12	0.00	2.500	27	0.01	2.541	42	0.03	2.602
13	0.00	2.521	28	0.01	2.533	43	0.00	2.515
14	0.00	2.509	29	0.00	2.525			
15	0.00	2.515	30	0.01	2.521			

with larger lattice constants do less contribute. It was verified that  $(\text{BN})_{1-x}(\text{C}_2)_x$  alloy obeys Vegard's law (DENTON; ASHCROFT, 1991) at the considered growth temperature. The calculated  $a(x, T)$  within the GQCA approach slightly deviates from the linear fit  $a(x) = a_{\text{BN}}(1 - x) + a_{\text{C}_2}x$ , with  $a_{\text{C}_2}=2.47 \text{ \AA}$  and  $a_{\text{BN}}=2.51 \text{ \AA}$ , with a rooted mean squared error (RMSE) lower than  $4 \cdot 10^{-3} \text{ \AA}$ .

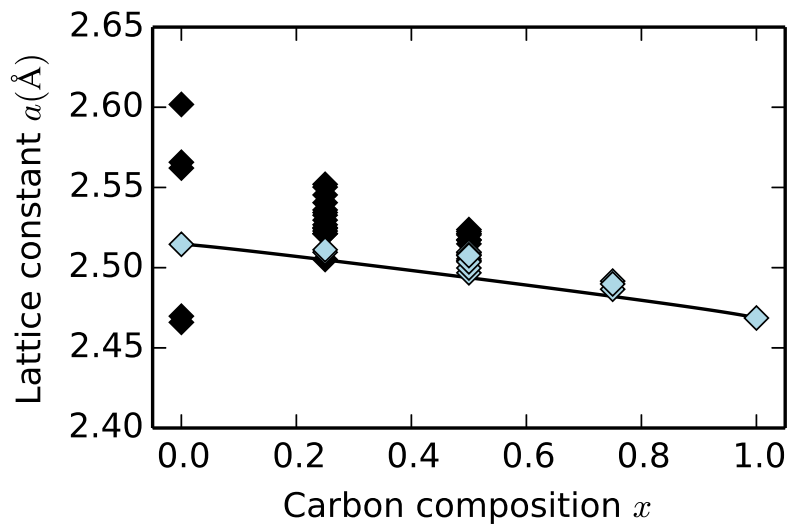


FIGURE 4.6 – The lattice parameter as a function of the carbon concentration for the  $(\text{BN})_{1-x}(\text{C}_2)_x$ . The black diamonds represent the configurations with B-B and N-N bonds, while the light blue ones represent the complementary configuration subset S. These calculations considered the growth temperature  $T=1600 \text{ K}$ .

The second structural property observed for the clusters is their buckling amplitude, which is defined as the maximum displacement of atoms from a flat configuration. The configurations CBBNBNCN ( $j = 34$ ) and BBBNBNNN ( $j = 39$ ) exhibit very high buckling values. A further investigation on those two configurations showed that the verified great layer buckling amplitudes are associated with deformations in the honeycomb structure in order to accommodate the neighbor boron atoms, which have greater atomic radii than carbon and nitrogen, as depicted in Fig.4.7. Despite of these two configurations, the mean buckling amplitude within GQCA shows that the alloy preserves the planar hexagonal structure exhibited by its end components as illustrated in Fig. 4.8.

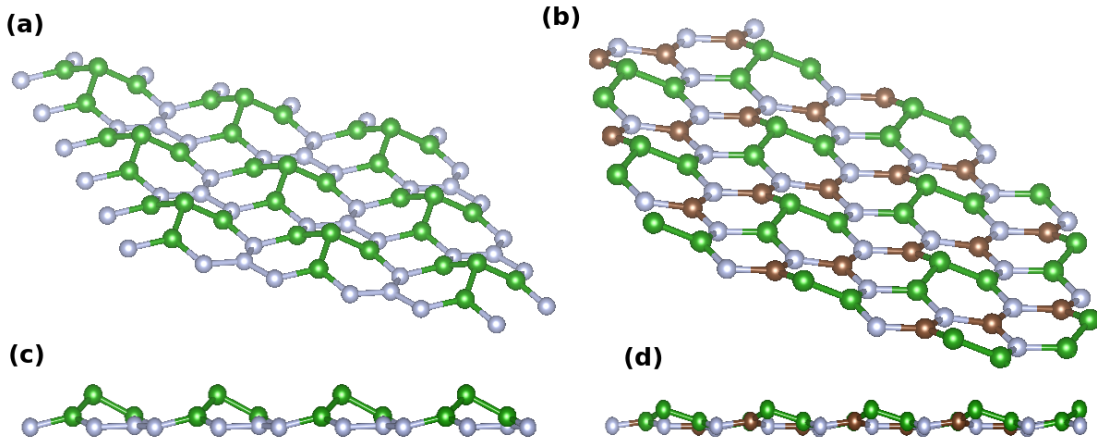


FIGURE 4.7 – Cluster configurations CBBNBNCN (a) and BBBNBNNN (b) of  $(\text{BN})_{1-x}(\text{C}_2)_x$  alloys are depicted in perspective. A lateral view of configuration CBBNBNCN is provided in (c) and one of BBBNBNNN configuration is provided in (d).

This effect is analogous to the very strong deformations depicted in Fig. 3.7 (a) and Fig. 3.7 (b) of  $\text{Ge}_{1-x}\text{C}_x$  and  $\text{Si}_{1-x}\text{C}_x$  alloy, respectively. Since the difference of atomic radii in boron and the other two element is small the effect is mitigated. One may also observe that as the number of boron atoms decreases from configuration  $j = 39$  ( $n_B = 4$ ) to  $j = 34$  ( $n_B = 3$ ), the buckling drops from  $1.00 \text{ \AA}$  to  $0.61 \text{ \AA}$ .

## 4.5 Electronic properties

In Table 4.4 we list the calculated fundamental energy gap for each cluster configuration. The values for the energy gaps of CCBNBNNB, CBCNBNNN, CBBBNNNC and BBBBNNNN configurations, which exhibit metallic behavior, are considered to be zero, in agreement with the interpretation that graphene is a zero-gap semiconductor. Metallic behavior of clusters with B-B and N-N bonds is in agreement with reported results to some  $\text{B}_x\text{C}_y\text{N}_z$  layered structures available in literature (MAZZONI *et al.*, 2006). However,

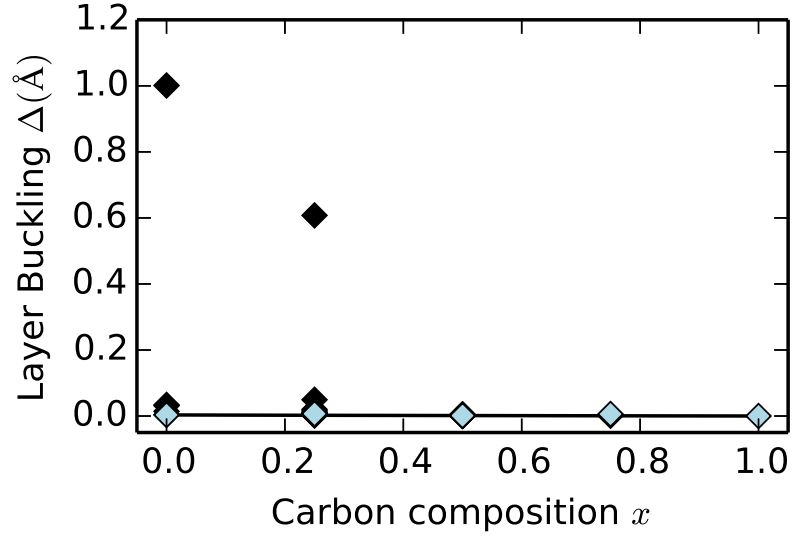


FIGURE 4.8 – The layer buckling amplitude as a function of the concentration for the  $(\text{BN})_{1-x}(\text{C}_2)_x$ . The black diamonds represent the configurations with B-B and N-N bonds, while the light blue ones represent the complementary configuration subset S.

these clusters do not have dominant influence on the alloy bandgap curve predicted within GQCA formalism.

Because of the high computational costs we restrict the electronic structure calculation using the hybrid functional HSE06 to the nine most statistically relevant configurations with the lowest excess energies, represented by the light blue diamonds in Fig.4.2. The considered configuration classes correspond up to the 99.6% of the total probability in the carbon poor phase ( $x'_1 = 0.02$ ) and to the 95.7% of the clusters in the carbon rich phase ( $x'_2 = 0.95$ ), according to GQCA calculations. As expected, the HSE06 results in larger fundamental energy gaps in comparison with DFT calculations, as can be observed comparing the dotted black and the full blue energy gap curves in Fig. 4.9.

Due the fact that only one configuration has significant statistical contribution at  $x=0$  and  $x=1$ , the energy band gap curve varies between  $E_{h-BN} = 6.06$  eV and  $E_C = 0$  eV, corresponding to pure hexagonal boron nitride and pure graphene, respectively. Without phase decomposition the system behaves like a homogeneous phase with the average concentration  $x$ . The solution of the Lagrange problem would yield to the a set of probabilities  $x_j$  that would give the energy band gap curve represented by the blue full line in Fig. 4.9. We define a concentration-dependent bowing parameter  $b(x)$  as a measure of the deviation from the linear behavior for the energy gap curve by fitting our results with the function  $E_g(x, T) = (1 - x)E_{BN} + xE_C - b(x) x(1 - x)$ . The calculated bowing parameter is  $b(x) = (5.6 - 4.9x)$  eV, with a rms deviation of 0.02 eV. This finding is a generalization of the estimated bowing parameter of 3.6 eV and 4.8 eV reported in

TABLE 4.4 – Energy gap  $E_g$  of the cluster configurations of  $\text{C}_x(\text{BN})_{1-x}$  alloys in eV. GGA calculations are performed for all configurations, while HSE06 hybrid functional is only considered for the statistically most relevant ones.

Class $j$	$E_g^{GGA}$	$E_g^{HSE}$	Class $j$	$E_g^{GGA}$	$E_g^{HSE}$	Class $j$	$E_g^{GGA}$	$E_g^{HSE}$
1	0.0	0.0	16	0.79	-	31	0.54	-
2	1.06	1.69	17	1.59	-	32	1.33	-
3	0.14	0.24	18	0.08	-	33	0.0	-
4	0.41	-	19	0.01	-	34	1.61	-
5	1.58	2.2	20	1.9	-	35	0.96	-
6	0.68	-	21	2.78	3.75	36	0.35	-
7	0.92	-	22	0.0	-	37	2.72	3.71
8	0.01	-	23	0.04	-	38	0.0	-
9	0.76	-	24	0.84	-	39	0.94	-
10	1.27	1.84	25	0.79	-	40	0.01	-
11	0.47	-	26	0.42	-	41	1.81	-
12	2.04	2.86	27	0.61	-	42	0.62	-
13	1.02	-	28	1.57	-	43	4.65	6.06
14	1.04	-	29	0.0	-			
15	0.1	-	30	1.18	-			

literature(UDDIN *et al.*, 2014; UDDIN *et al.*, 2015), based on the available experimental data for the fundamental energy gap of the two end components and samples of  $1\mu\text{m}$ -thick  $\text{BC}_2\text{N}$  ( $x=0.5$ ) films (WATANABE *et al.*, 1996).

At compositions  $x$  where the system tends to segregate in phases with compositions between  $x_1$  and  $x_2$ , visible in the phase diagram in Fig. 4.3, the set of probabilities  $x_j$  derived within GQCA does not represent the fully decomposed alloy. Rather in this case, we have to estimate  $E_g(x, T)$  as a weighted mean of the energy gaps of  $E_g(x_1, T)$  and  $E_g(x_2, T)$  of the carbon-poor and -rich phases with respective weights  $w_1$  and  $w_2$ . Since the weights  $w_1$  and  $w_2$  vary linearly with the average composition  $x$ ,  $E_g(x, T)$  should vary linearly in the range  $x_1 < x < x_2$  when phase segregation effects is included. This fact is represented by the blue dashed line in Fig. 4.9.

As one can observe in Fig. 4.9, different energy gap values are possible for different cluster configurations with the same carbon concentration. This indicates that the use of statistical approaches to account for disorder effects are mandatory due the fact that a change of the atomic arrangement of atoms can result in entirely different electronic properties. Therefore, the choice of particular cluster configurations with a defined composition might not properly represent the chemically disordered system with an average composition  $x$  and composition fluctuations derived within the GQCA formalism. For example, the non-monotonic behavior of the energy gap as a function of the concentration was reported by D'Souza and Mukherjee (D'SOUZA; MUKHERJEE, 2015) when considering particular zigzag and armchair interfaces configurations is not observed when disordered

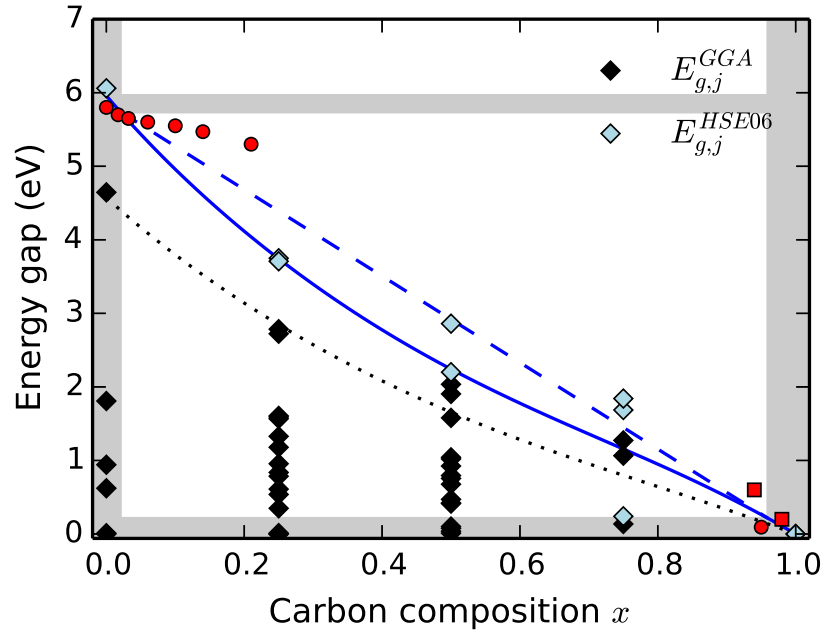


FIGURE 4.9 – The energy band gap as a function of the composition for the  $(\text{BN})_{1-x}(\text{C}_2)_x$  alloys obtained with the GGA functional (dotted black curve) and within the HSE06 approach with and without phase decomposition effects (full and dashed blue lines, respectively). The vertical grey shades indicate the  $x$  compositions where the alloy is stable and the horizontal ones corresponds to the energy gap tune range at the stable composition conditions. The black and light blue diamonds represent the energy band gap obtained by GGA and HSE06 calculations for the investigated clusters. Available experimental data are represented by red circles (UDDIN *et al.*, 2014; UDDIN *et al.*, 2015) and squares (CHANG *et al.*, 2013).

configurations and statistics are considered as illustrated in Fig.4.9.

The comparison between theoretical and experimental results displayed in Fig. 4.9 require further discussions. For carbon concentrations under the carbon solubility (vertical grey shaded areas) the experimental and the theoretical curve agree. The same behavior is observed for carbon-rich alloys, where our theoretical energy gap curve stands between the experimental findings (UDDIN *et al.*, 2015; CHANG *et al.*, 2013). For BN-rich alloys with carbon concentrations above its solubility in *h*-BN (UDDIN *et al.*, 2014), where phase segregation occurs, the decrease of the energy gap is much weaker than the predicted GQCA curve and stays near to the horizontal shaded area. This result can be explained if we consider the phase separation process: the light possibly comes from BN-rich segregated domains, leading to carrier localization.

## 4.6 Optical properties

Optical measurements for the  $(\text{BN})_{1-x}(\text{C}_2)_x$  alloy show two absorption edges at different carbon concentrations which can be associated with a carbon-rich and a BN-rich phases (CI, 2010; CHANG *et al.*, 2013). The relative intensities of the peaks depend on the alloy composition between the two end components, while their positions do not change appreciably with  $x$ .

In Fig. 4.10, we compared the estimation of the optical absorbance spectra given by equation 2.109,  $A_{GQCA}(\omega, x, T)$ , assuming local composition fluctuations and domain sizes between 2-3 nm and the absorbance spectra considering a complete phase segregation of the system  $A_{PS}(\omega, x, T)$ , as expressed by equation 2.110. The optical absorbance of the carbon-rich and BN-rich phases have pronounced absorbance peaks in the considered wavelength region. The peak of the carbon-rich phase is associated with  $\pi$ - $\pi^*$  transitions at M point in graphene (CHANG *et al.*, 2013; MAK *et al.*, 2008), while the peak of the BN-rich phase is associated with the optical transition associated with the  $h$ -BN band gap in the UV region. In the long-wavelength limit the absorption almost vanishes for  $h$ -BN-rich phase due to its large gap, approaching 6 eV. On the contrary, in the case of the graphene-rich phase the in-plane absorbance reaches a value  $\pi\alpha$  ( $\alpha$  - Sommerfeld fine structure constant). This has been demonstrated experimentally (NAIR *et al.*, 2008). It goes back to the linear bands of graphene forming Dirac cones at K and K' points in the Brillouin zone (MATTHES *et al.*, 2013a; MATTHES *et al.*, 2014).

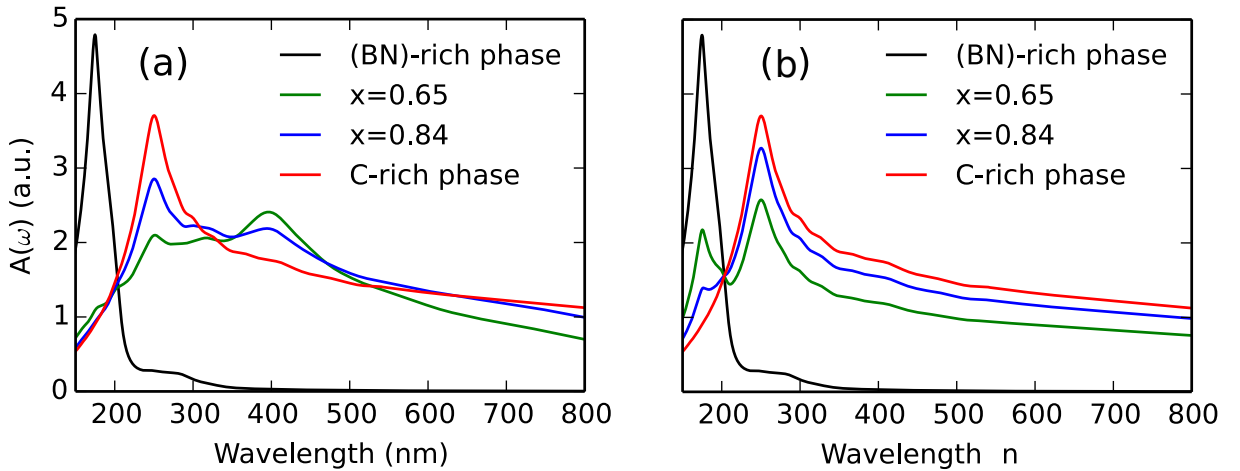


FIGURE 4.10 – Optical absorbance as a function of the wavelength for  $(\text{BN})_{1-x}(\text{C}_2)_x$  alloys with different carbon compositions. The red (black) full line stands for the carbon-rich (BN-rich) phase for comparison with intermediate compositions  $x=0.65$  and  $x=0.84$ , represented by green and blue lines. The absorption spectra predictions are calculated considering local composition fluctuations (a) and complete phase segregation (b).

The difference between the blue and green lines in Fig. 4.10(a) and Fig. 4.10(b) for average composition  $x=0.65$  and  $x=0.84$  shows a very strong effect of phase decomposition

on the absorbance spectrum of alloys with intermediate compositions. When small clusters and composition fluctuations are assumed in Fig. 4.10(a), clusters with intermediary composition and lower fundamental energy gap are favored. Therefore, besides a reduction of the intensity of the graphene absorption peak additional red-shifted absorption peaks appear, which however are not experimentally observed. Otherwise, if the phase segregation is considered as in Fig. 4.10(b), the absorbance spectra  $A_{PS}(\omega, x)$  is given by a weighted mean between the spectra of the two segregated phases and have the same qualitative behavior as the experimental findings (CI, 2010; CHANG *et al.*, 2013).

These results confirm the strong evidence for the  $(\text{BN})_{1-x}(\text{C}_2)_x$  phase segregation in the measured absorbance spectra. The absorption peak associated with poor-carbon phase is less pronounced than in the experiment due the neglect of excitonic effects (WATANABE; KANDA, 2004), which enhances the absorption peak observed at about 200 nm in *h*-BN in particular due to the formation of exciton bound states with energies of 5.822 eV (ARNAUD *et al.*, 2006).

# 5 Graphene Oxide

## 5.1 Introduction

Alloying methodologies are not the only alternatives to obtain chemically controlled properties of 2D materials. There are different chemically functionalized 2D sheets obtained through oxidation (MAO *et al.*, 2012; LOH *et al.*, 2010), hydrogenation (SOFO *et al.*, 2007; ELIAS *et al.*, 2009) or halogenation (POH *et al.*, 2013; LIAO *et al.*, 2014) processes that exhibit distinct properties as their original counterparts. Partial functionalization processes are able to obtain tunable properties from both counterpart in an analogous methodology as electronic and optical properties tuning by alloying.

Fully oxidized graphene, or graphene oxide (GO), opens energy gaps and exhibit significantly different electronic and optical properties from graphene (EIGLER; HIRSCH, 2014; LOH *et al.*, 2010; MAO *et al.*, 2012; DREYER *et al.*, 2010; PULCI *et al.*, 2012). This material paves the way for a new class of two-dimensional (2D) graphene-based materials. GO has its own applications in 2D sensor devices (ROBINSON *et al.*, 2008; DUA *et al.*, 2010), electronics (GOMEZ-NAVARRO *et al.*, 2007; WEI *et al.*, 2010; WU *et al.*, 2008), optoelectronics (LOH *et al.*, 2010; WU *et al.*, 2008) and supercapacitors (ZHANG; ZHAO, 2012). The first GO samples were chemically exfoliated about 150 years ago by Bodie (BRODIE, 1859) from graphite oxide. However, due to its amorphous nature, the details of its atomic structure are still under debate (EIGLER; HIRSCH, 2014; MAO *et al.*, 2012). Experimental findings indicate that the epoxy and hydroxyl groups tend to adsorb close to each other (CAI *et al.*, 2008). GO is synthesized from graphite powder using chemical solutions with oxidant compounds and subsequent exfoliation (MAO *et al.*, 2012). Wet chemical treatment of graphene and the exposure to oxygen plasma are successful ways to obtain GO samples (NOURBAKHSH *et al.*, 2010).

Besides the structural disorder, the resulting GO may also be understoichiometric by the incomplete oxidation of graphene. The incomplete oxidation may also be reached by chemical reduction of fully-oxidized GO (KIM *et al.*, 2009). The understoichiometric oxides allow to tune their properties between those of GO and graphene. In this thesis, we have investigated the potential of tunable properties of understoichiometric GO studying the

effect of  $-\text{OH}$  and  $-\text{O}-$  adsorption on graphene with a cluster expansion of the system. The considered clusters have 8 C atoms and can have from 0 to 8 (0 to 4) adsorbed hydroxyl (epoxy) groups. The section 5.2 describes the considered configuration labels of the cluster expansion in the following sections. They may be interpreted as variations between graphene (C), fully oxidized graphene with only  $-\text{OH}$  groups (COH), and fully oxidized graphene with only  $-\text{O}-$  groups ( $\text{CO}_{1/2}$ ). The understoichiometric GO systems are initially investigated considering the effect of adsorption of only hydroxyl or epoxy groups, separately, in sections 5.4 and 5.5 respectively. The effect of different oxidant groups on the energetic stability, atomic geometry and accompanying electronic and optical properties are less studied and, therefore, widely not understood.

At last, in section 5.6, we investigate the simultaneous adsorption of hydroxyl and epoxy groups on graphene. The resulting non-stoichiometric GOs exhibit structural and chemical disorder. We focus here on new phenomena due to the simultaneous appearance of two different oxidant groups. We report on unambiguous features of GO energetics, for instance the increase of energetic stability, as for low-energy fully oxidized graphene with both hydroxyl and epoxy groups. Such structures give rise to larger energy gap ranges for band gap engineering. Ordered geometries may indicate that the oxidant groups agglomerate in a unique oxygen-rich phase.

## 5.2 Cluster expansion and configurational counting

Here, we generalize the method for simultaneous occurrence of  $-\text{OH}$  and  $-\text{O}-$  groups. We chose 2D supercells with  $n = 8$  carbon sites, where the hydroxyl groups can be adsorbed, and  $n = 12$  carbon-carbon bonds, that can be bridged by epoxy groups, as illustrated in Fig. 5.1. We consider the possible arrangements of oxidant groups, which fulfill the following conditions: (i) carbon atoms are three- or fourfold-coordinated after adsorption, and (ii) hydroxyl groups are not allowed to adsorb on first-nearest-neighbor carbon atoms at the same side of the graphene basal plane. These conditions reduce the considered atomic arrangements to configurations with moderate formation energies, as will be demonstrated in Sec. 5.3. The described constraints result in a set of 16343 possible arrangements, with  $n_{\text{OH},j}$   $-\text{OH}$  groups and  $n_{\text{O},j}$   $-\text{O}-$  groups. They can be reorganized in  $J = 308$  symmetry equivalent classes considering all possible symmetry operations, with different degeneracies  $g_j$ . For discussion of specific atomic arrangements, a labeling procedure is explained and exemplified in the caption of Fig. 5.1.

Among the set of 308 symmetry equivalent classes, we selected for preliminary studies the 31 configurations with the adsorption of  $-\text{OH}$  groups, and 24 configuration with  $-\text{O}-$  groups. The obtained results from the investigation of these configuration sets are

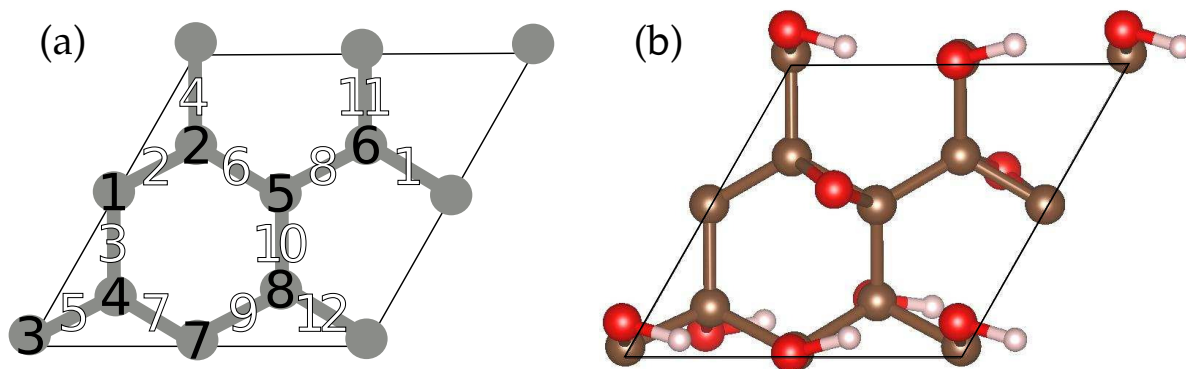


FIGURE 5.1 – (a) The atomic sites (carbon-carbon bonds) are labeled with integer numbers from 1 to 8 in black (1 to 12 in white). Sites without oxygen groups are represented as 0, oxygen groups above the graphene layer as ‘u’ and oxygen groups down the graphene layer as ‘d’. The configuration label is obtained by the combination of atomic site labels followed by the carbon-carbon bond ones. (b) An example of a cluster configuration. Carbon, oxygen and hydrogen are respectively illustrated by brown, red and white spheres. According to the labeling system described in (a), the configuration of the represented atomic arrangement is 00ud00ud-d0000u000000.

described in sections 5.4 and 5.5. In the study of the configurations with only hydroxyl (epoxy) adsorption, we simplify the configuration notation to only the 8 atomic sites (12 carbon-carbon bonds) occupation description.

### 5.3 Fully oxidized sheets

In order to describe completely oxidized graphene we study the two oxidant groups, epoxy and hydroxyl, separately. In both cases, we investigate the possible arrangement of these groups on both sides of the graphene sheet. We start with the full hydroxyl decoration of graphene. Thereby, in case of the adsorption of the  $-OH$  groups, we restrict to their alternating bonding to the single carbon atoms on top and below the graphene sheet. This leads to 8  $-OH$  groups ( $n_S = n_{OH} = 8$ ) per 2x2 graphene unit cell as depicted in Fig. 5.2 (a) (generalized Ruess model (MAO *et al.*, 2012)). The illustrated configuration is used as an example of labelling and is further explained in the caption, following the defined labels and symbols. We avoid atomic configurations with too large formation energies. These thermodynamically unfavorable arrangements with small statistical weights in the GQCA approach are atomic arrangements with two neighboring hydroxyl groups bonded to the same side of the carbon sheet. This disregard was verified by comparing the total energies of the clusters 000000++ and 000000+- with two hydroxyl groups at adjacent carbon sites in parallel or antiparallel orientation. The repulsive interaction between two neighboring hydroxyl groups at the same side of the sheet results in an energy increase of 1.31 eV/cluster. The strong electrostatic repulsion between neighboring hydroxyl groups is

due the large electronegativity of oxygen compared with the hydrogen and carbon values (MÖNCH, 1993). The negatively charged oxygen ions in the  $-\text{OH}$  group are responsible for the repulsion if they come too close to each other.

In the case of graphene oxide decorated only by epoxy groups, one oxygen atom bridges two carbon atoms along one carbon  $sp^2$  bond (generalized Hofmann model (MAO *et al.*, 2012)). The constraints of alternate bonding (hydroxyls) and fourfold-coordinated carbon atoms (epoxides) are kept for a reasonable number of significant atomic arrangements with oxidant groups. Consequently, no adjacent C–C bonds can be occupied by another oxygen atom.

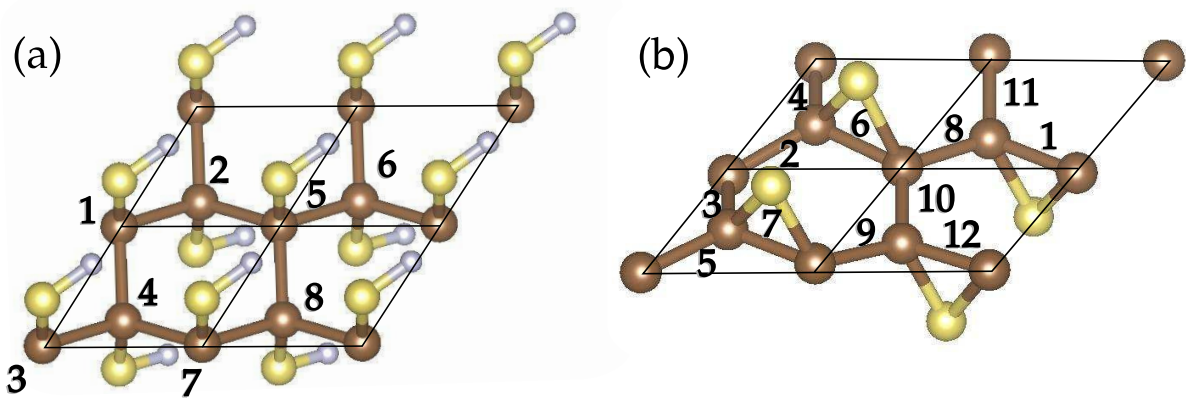


FIGURE 5.2 – Illustration of cluster configurations of graphene with a maximum number of oxidant groups: (a)  $n_{\text{OH}} = 8$  alternately bonded hydroxyl groups and (b)  $n_{\text{epo}} = 4$  epoxy groups. Carbon, oxygen and hydrogen atoms are respectively represented by brown, golden and grey spheres. In case that only hydroxyl (epoxy) group adsorption is considered, the configuration label described in Fig. 5.1 can be simplified to 8 sites (12 C-C bonds) label. Consequently, the represented atomic arrangements are (a)  $+-+-+-$ , and (b)  $-0000++0000-$ .

Because of the pairing character of the oxidation by epoxy groups, we have to count  $n_B = 12$  carbon-carbon bonds per cluster because of the constraint for three-fold or four-fold coordination of carbon atoms. Only four bridging  $-\text{O}-$  groups can be adsorbed by a  $2 \times 2$  clusters in total. Each carbon is only allowed to bond to one epoxide group. Since neighboring C-C bonds cannot be occupied by  $-\text{O}-$ , the repulsion of the negatively charged oxygen atoms is mitigated. Therefore, all the possible manners of arranging epoxide groups on both sheet sides are considered. One of these eight possible cluster atomic arrangements with epoxide groups  $-0000++0000-$  is shown in Fig. 5.2 (b) explaining also the labelling of the twelve C-C bonds.

In the GQCA formalism, presented in Sec. 2.2.4, the configurational entropy formula expressed in Eq. (2.93) allows us to impose different constraints and consider both substitutional alloys or group adsorption on sites or bonds in a unified theoretical formalism. Besides the chemical disorder due to fluctuating number of sites or bonds occupied by

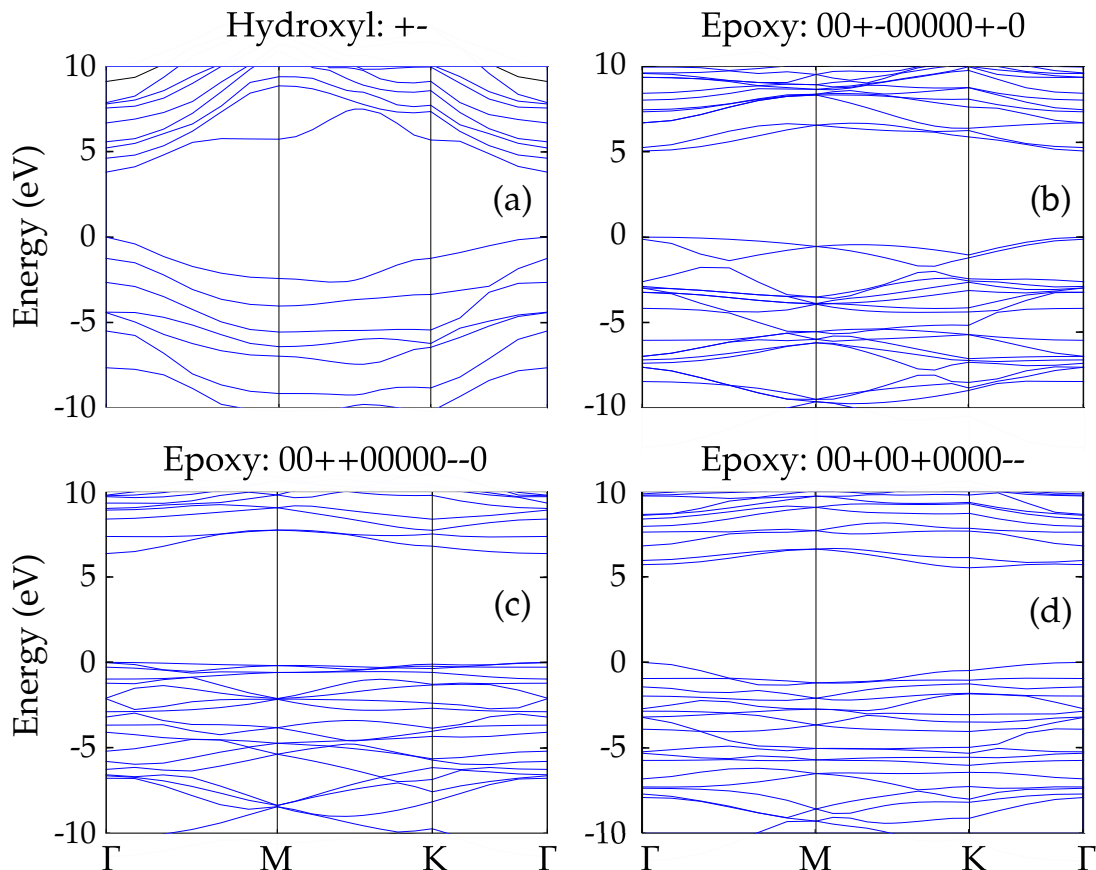


FIGURE 5.3 – Electronic band structures for fully oxidized cluster configurations ( $x = 1$ ) obtained from HSE06 calculations: (a) carbon sheet completely oxidized with  $-OH$  groups is described within the  $1 \times 1$  unit cell in order to avoid band folding associated with the use of the  $2 \times 2$  supercell, and (b,c,d) thermodynamically favorable epoxy-oxidized systems studied within  $2 \times 2$  supercells used in the cluster expansion of the disordered system. The valence band maximum (VBM) is chosen as energy reference.

oxidant groups, also structural disorder, e.g. due to the arrangement of the oxidizing groups on both sides of the carbon layer, is accounted.

In order to use the canonical ensemble, the average number of oxygen groups per cluster in the system  $\overline{n_O}$  can be characterized according to the oxidation level  $x$ , defined as the fraction of carbon atoms functionalized with oxygen atoms in the carbon sheet. For the hydroxyl (epoxy) oxidation process, the atom ratio C/O is given by  $1/x$  ( $2/x$ ). In this sense  $x$  describes the average composition of the non-stoichiometric oxides  $C_{1-x}(COH)_x$  or  $C_{1-x}(CO_{1/2})_x$ , depending on the oxidant group considered. A more general formalism that considers a grandcanonical ensemble with the number of oxygen groups determined by chemical environment conditions may be explored, but will be left as a future work.

Within the described framework the fully oxidized system with hydroxyl groups (in which  $x = 1$ ) is a honeycomb structure with  $sp^3$  hybridized carbons, labelled as  $+ - + - + -$  (cf. Fig. 5.2(a)). This cluster configuration exhibits a lattice constant of  $a_{COH} = 2.63 \text{ \AA}$ ,

which is larger than graphene lattice constant  $a_C = 2.47 \text{ \AA}$ , leading to a lattice constant mismatch of 6.5%. Due to the tendency for  $sp^3$  hybridization, the carbon layer exhibits a buckling amplitude of  $\Delta = 0.50 \text{ \AA}$ . The obtained carbon-oxygen and oxygen-hydrogen bonds show respective lengths of  $d_{CO} = 1.42 \text{ \AA}$  and  $d_{OH} = 0.99 \text{ \AA}$ , which determine an angle of  $\theta_{OH} = 107^\circ$  between them. The structural parameters are similar to those obtained using a  $5 \times 5$  graphene supercell (LU *et al.*, 2011). We investigated the influence of hydroxyl orientation on calculated energy gap for the fully decorated configuration, but no changes above 0.1 eV were observed.

The fully oxidized configuration in Fig. 5.3 exhibits a direct energy gap of 3.78 eV at the  $\Gamma$  point according to the HSE06 calculation, showing the potential of the oxygen groups to significantly change the electronic structure of the graphene sheet. The zero-gap semimetal graphene becomes as graphene oxide a wide-gap semiconductor or insulator as other functionalized graphene layers, e.g. hydrogenated graphene (PULCI *et al.*, 2012). The obtained electronic band structure for this oxide is illustrated in Fig. 5.3(a). Other HSE calculations even suggest a larger gap of 4.32 eV (JIANG *et al.*, 2013).

Differently from the oxidation based on hydroxyl groups, a fully oxidized graphene sheet with epoxy groups is not unique. There are a total of 8 fully oxidized configurations with  $n_{\text{epo},j} = 4$  epoxide groups. The possible clusters exhibit different arrangements of epoxy groups with respect to which side of the carbon sheet the oxygen groups are bonded and in which ordering the epoxy groups are distributed along the carbon honeycomb structure. Because of such structural disorder, a statistical treatment is necessary even for a fully oxidized system, in which the occurrence probability of each configuration is determined by the cluster energetics and the cluster degeneracy. The equilibrium state is calculated by the minimization of the system free energy considering  $x = 1$ . The lattice constants of the fully oxidized configurations stand between  $2.55 \text{ \AA}$  and  $2.67 \text{ \AA}$ . They lead to a mean lattice constant of  $2.57 \text{ \AA}$  at  $200 \text{ }^\circ\text{C}$ . The average lattice mismatch in comparison to the pure graphene amounts to 4%. The graphene oxide layer possesses an average buckling amplitude of  $0.36 \text{ \AA}$  at  $200 \text{ }^\circ\text{C}$  and does not significantly change until temperatures of order of  $1100 \text{ }^\circ\text{C}$ . The epoxy groups are characterized by C-O bond lengths of  $1.43 \text{ \AA}$  and a C-O-C bond angle close to  $63^\circ$  in rough agreement with calculations for isolated groups (KIM *et al.*, 2009; LU *et al.*, 2011).

The band structures of the three most energetically stable configurations with  $n_{\text{epo},j} = 4$  are illustrated in Figs. 5.3(b,c,d) for comparison. The different arrangements of the epoxy groups lead to distinct electronic structures. The fundamental energy gaps calculated for the 00+-00000+-0, 00++00000-0 and 00+00+0000- configurations are respectively 5.05, 6.37 and 5.50 eV from the HSE06 calculations. Both the direct  $\Gamma - \Gamma$  gap and the indirect  $\Gamma - K$  gap are observed in the studied configurations. Our gap findings are close to the HSE value of 6.2 eV found by Jiang *et al.* (JIANG *et al.*, 2013).

In Fig. 5.4, we show the in-plane components of the absorbance obtained from the DFT calculations for graphene and carbon sheets fully decorated with  $-\text{OH}$  or  $-\text{O}-$  groups as a function of the incident photon energy. While graphene and  $-\text{OH}$  decorated carbon sheet spectra are calculated directly from periodic structures, the illustrated spectra of the graphene fully oxidized with epoxy groups is obtained from a weighted average of the 8 possible epoxy arrangements in a  $2 \times 2$  unit cell at  $T = 300$  K. The absorbance spectrum of graphene exhibits an absorbance of  $\pi\alpha$  ( $\alpha$  is the Sommerfeld fine structure constant), while a very pronounced peak at about 4.0 eV associated with the saddle point of the valence and conduction  $\pi$ -band difference. These spectral features have been previously discussed in theoretical (MATTHES *et al.*, 2013a) and experimental (NAIR *et al.*, 2008) works. In the case of oxidized graphene sheets, the band gap opening forbids optical transitions for small photon energies and the sheets are transparent for low energy radiation. For these materials, the optical absorbance significantly increases for photon energies above 4 eV in agreement with the calculated gaps.

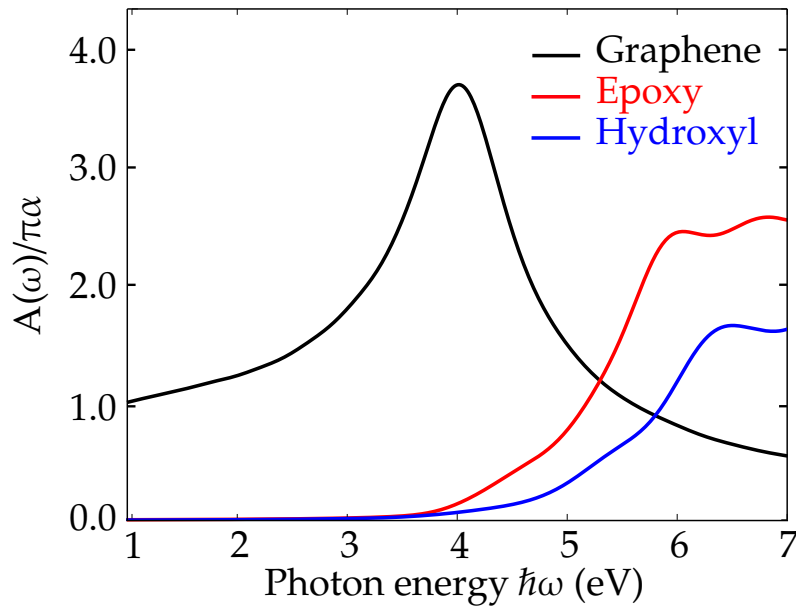


FIGURE 5.4 – Optical absorbance  $A(\omega)$  of graphene (black curve), and carbon sheets fully decorated with hydroxyl (blue curve) or epoxy (red curve) groups as a function of the incident photon energy. The statistical weights of the different arrangement of configurations with  $n_{\text{epo},j} = 4$  are calculated considering a preparation temperature of  $T = 300$  K.

## 5.4 Partial hydroxyl oxidation

The considered cluster size, combined with the assumption that first-neighbor hydroxyl groups must have anti-parallel orientations, results in 743 possible arrangements, containing between  $n_{\text{OH},j} = 0$  and  $n_{\text{OH},j} = 8$  hydroxyl groups per cluster, which can be organized in

$J_{\text{epo}} = 31$  symmetry-equivalence classes considering all possible space-group symmetry operations. The quantities characterizing the 31 clusters with respect to the cluster statistics and their electronic structure are summarized in Table 5.1.

We start the investigation of the thermodynamic stability for intermediate oxidation levels by considering the excess energies  $\Delta E_j$  of the 31 considered cluster classes versus the number of bonded hydroxyl groups per cluster  $n_{\text{OH},j}$ . The considered energies were obtained from spin-polarized calculations. The calculated values are depicted in Fig. 5.5 and listed in Table 5.1.

TABLE 5.1 – Cluster classes  $j$ , their labels, their degeneracies  $g_j$ , numbers of hydroxyl groups per cluster  $n_{\text{OH},j}$ , excess energies  $E_j$  per cluster, and fundamental energy gaps from PBE ( $E_{g,j}^{\text{PBE}}$ ) and HSE06 calculations ( $E_{g,j}^{\text{HSE}}$ ). Metallic configurations are indicated by ‘Metal’.

$j$	Label	$n_{\text{OH},j}$	$g_j$	$\Delta E_j$ (eV)	$E_{g,j}^{\text{PBE}}$ (eV)	$E_{g,j}^{\text{HSE}}$ (eV)
1	00000000	0	1	0.00	Metal	Metal
2	0000000+	1	16	1.50	1.32	1.92
3	000++000	2	8	1.29	2.68	3.92
4	000+-000	2	8	1.63	2.75	3.96
5	00000+0+	2	24	2.97	Metal	Metal
6	00000+0-	2	24	3.14	Metal	Metal
7	000000+-	2	24	1.19	0.32	0.46
8	000++00-	3	48	2.02	0.54	1.04
9	000+-00+	3	48	1.98	0.88	1.53
10	000+0+0+	3	16	3.73	Metal	Metal
11	000+0+0-	3	48	5.10	Metal	Metal
12	00000+-+	3	48	1.71	1.11	1.51
13	0+0+0+0+	4	4	7.87	Metal	Metal
14	0+0+0+0-	4	16	2.51	Metal	Metal
15	0+0+0-0-	4	12	5.18	Metal	Metal
16	00+-+00	4	12	2.09	1.61	3.21
17	00+-+00	4	12	1.84	2.14	3.68
18	000++-0-	4	48	3.05	Metal	Metal
19	000+-+0+	4	48	2.06	2.02	3.11
20	000+-0+	4	48	1.13	2.39	3.53
21	000+0+-+	4	16	3.53	Metal	0.02
22	0000+-+-	4	12	0.19	0.18	0.59
23	0+0+0+-+	5	16	5.86	0.02	0.26
24	0+0-0+-	5	16	4.63	Metal	0.32
25	00+-+0-	5	48	3.26	Metal	0.05
26	000+-+-+	5	48	1.63	0.43	1.20
27	0+-+--0	6	8	3.46	Metal	0.37
28	0+0+-+-+	6	24	3.35	Metal	0.79
29	00+-+--	6	24	1.01	2.40	3.96
30	0+-+--+	7	16	1.74	Metal	0.04
31	+--+--+	8	2	0.00	2.25	3.78

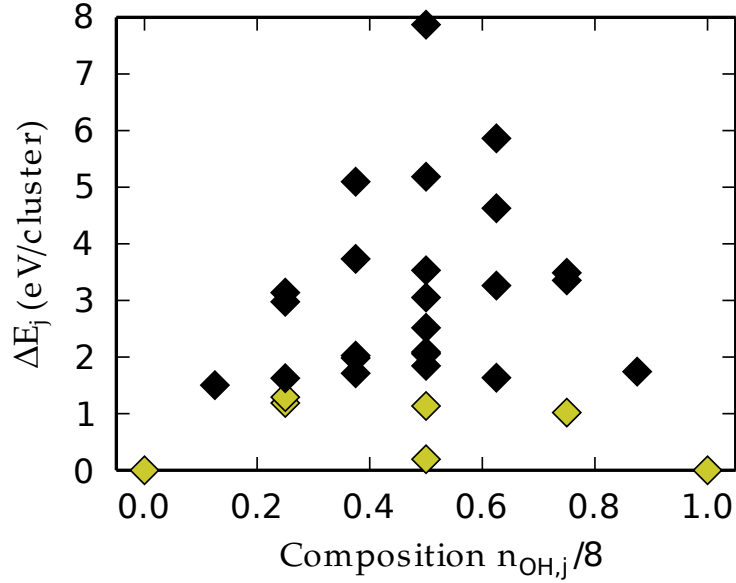


FIGURE 5.5 – Excess energies  $\Delta E_j$  of cluster configurations functionalized with hydroxyl groups as function of the number of oxygen groups per cluster  $n_{\text{OH},j}$ . The cluster configurations with  $\Delta E_j < 1.5$  eV/cluster are represented as golden diamonds, while the complementary set is represented in black.

For intermediate oxidation levels the excesses energies  $\Delta E_j$  are distributed in a very wide range between 0.19 eV/cluster and 7.87 eV/cluster, indeed occurring when  $n_{\text{OH},j} = 4$ . There is a clear tendency that the most stable configurations with  $\Delta E_j < 2$  eV favor the hydroxyl clustering, as can be observed for configurations 000000+- ( $j=7$ ), 00000+-+ ( $j=12$ ), 0000+-+- ( $j=22$ ), 000+-+--+ ( $j=26$ ), and 00+-+--+ ( $j=29$ ) (see Table 5.1 and Fig. 5.6). These are the most stable configurations for each possible number of hydroxyl groups per cluster,  $2 \leq n_{\text{OH},j} \leq 6$ . The most energetically unfavored configuration is 0+0+0+0+ ( $j=13$ ), which does not exhibit pairs of neighboring hydroxyls. Apart from the pure graphene ( $j=1$ ) and graphene oxide ( $j=31$ ) the most stable intermediate configuration 0000+-+- ( $j=22$ ) represents an ordered structure with parallel zig-zag chains of alternately arranged  $-\text{OH}$  groups in the direction of a hexagonal lattice vector (see Fig. 5.6). This chain ordering significantly reduces the total energy, since the repulsion of  $-\text{OH}$  groups in vertical direction of the chains is practically not present, which is in agreement with previous investigations on graphene oxide energetics (YAN *et al.*, 2009; YAN; CHOU, 2010). As the consequence of the resulting adjacent graphene-like chains the gap opening of the half-oxidized system  $j=22$  is small, only of 0.6 eV. The  $-\text{OH}$  groups in understoichiometric graphene oxide with  $x=0.5$  prefer to aggregate along the armchair direction of graphene as one-dimensional chains on the basal plane has been demonstrated also in the other theoretical studies (WANG *et al.*, 2010; JIANG *et al.*, 2013).

The thermodynamic stability of a non-stoichiometric graphene oxide is investigated by the construction of the  $T$ - $x$  phase diagram, depicted in Fig. 5.7, from the temperature- and composition-dependent mixing free energy  $\Delta F(x, T)$ . A double-peak pattern is observed

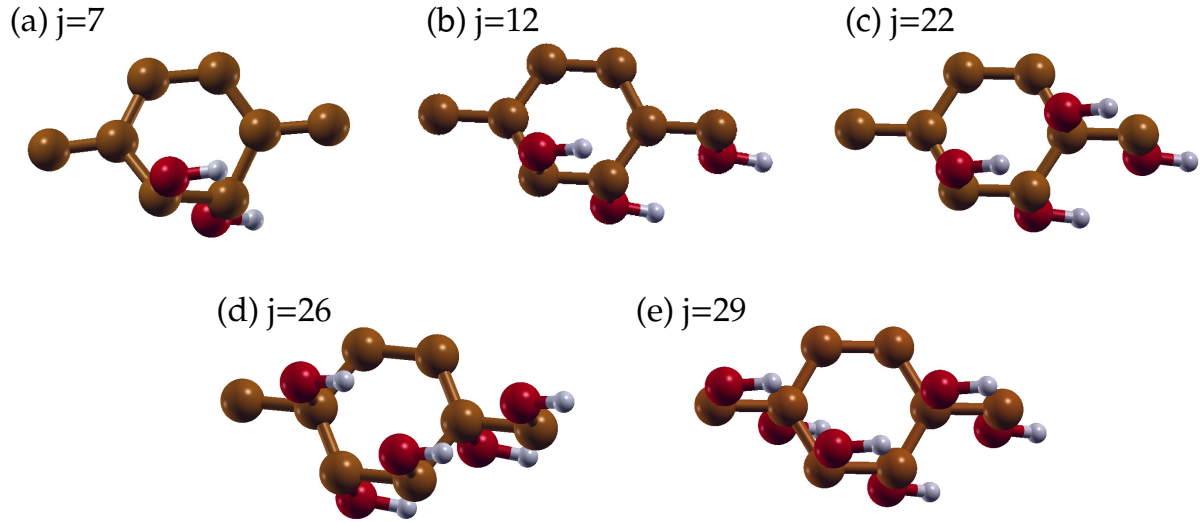


FIGURE 5.6 – Energetically favored ( $\Delta E_j < 2$  eV) graphene oxide cluster configurations with partial hydroxyl decoration: (a) 000000+-, (b) 00000+--+, (c) 0000+--+-, (d) 000+--+-+, (e) 00+--+-+, and (f) 0+--+-+-. The indicated cluster numbering  $j$  refers to Table 5.1. Carbon, oxygen and hydrogen atoms are respectively represented by brown, red and grey spheres.

in the binodal and spinodal curves, because of the low-energy chain structure  $j = 22$  but also the linear chain arrangement  $j = 17$  and its slightly distorted version  $j = 20$ . An extremely large critical temperature of  $T_c = 6000$  K is calculated, meaning that graphene oxide exposed to hydroxyl groups cannot be prepared as a homogeneous phase at any oxidation level  $x$  and common growth temperatures. Both findings indicate a strong phase segregation tendency of the hydroxyl-covered graphene into oxygen-poor and -rich phases, which has been also indicated by experimental findings (HE *et al.*, 1998; LERF *et al.*, 1998) and other theoretical investigations (YAN *et al.*, 2009; YAN; CHOU, 2010; ZHOU *et al.*, 2013). For higher-temperature preparation conditions and  $x = 0.5$ , however, one cannot exclude a partial decomposition in a third phase mainly consisting by the ordered armchair chain structure  $j=22$ .

We investigate, besides room temperature, typical temperatures of  $200^\circ\text{C}$  (473 K) and  $1100^\circ\text{C}$  (1373 K), which represent different possible preparation conditions at which the graphene oxide samples can be produced (PEI; CHENG, 2012). The average properties of non-stoichiometric graphene oxide are estimated according to Eq.(2.77).

The mean lattice constant as a function of the oxidation level  $x$  can be approximated as  $a(x) = xa_{COH} + (1-x)a_C - bx(1-x)$ , where  $b$  is known as the bowing parameter of the curve, because it represents the deviation of the system from the Vegard's law (VEGARD, 1921; DENTON; ASHCROFT, 1991). Bowing parameters of  $b = 0.10 \text{ \AA}$  and  $b = 0.11 \text{ \AA}$  are calculated for the growth temperatures of  $T = 473 \text{ K}$  and  $1373 \text{ K}$ , respectively. Therefore, mainly a linear variation with composition with only a small, almost temperature-independent bowing is found. The buckling parameter  $\Delta$  (not shown)

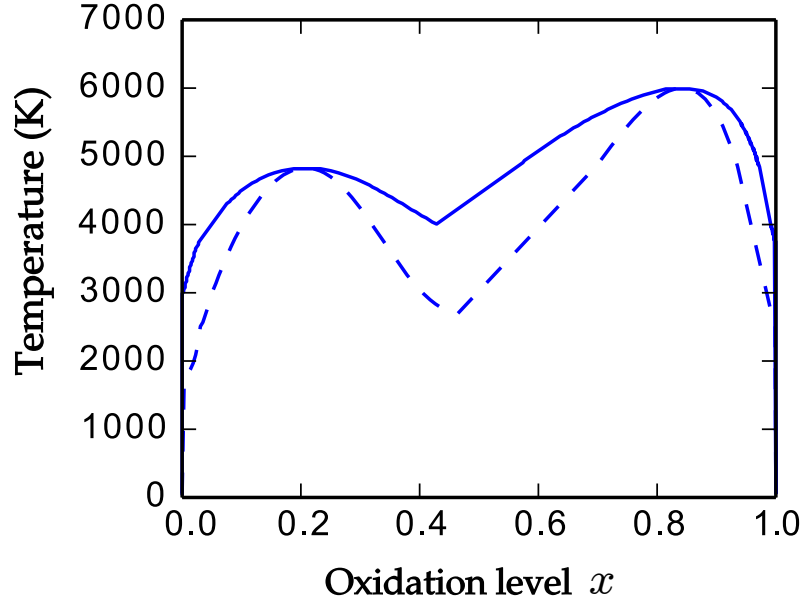


FIGURE 5.7 – The  $T$ - $x$  phase diagram of graphene functionalized with hydroxyl groups  $C_{1-x}(COH)_x$ . The binodal (spinodal) curve is represented by the full (dashed) line.

varies non-linearly and non-monotonically with composition from zero to the graphene oxide value. A maximum average buckling amplitude of  $\Delta = 0.57$  ( $0.65$ )  $\text{\AA}$  is calculated at  $x = 0.64$  ( $0.49$ ) for a preparation temperature of  $T = 473$  K ( $1373$  K). The observed non-monotonic behavior of the buckling amplitude comes from cluster classes with intermediate oxidation levels that exhibit buckling amplitudes larger than  $0.9$   $\text{\AA}$  due to their particular arrangement of  $sp^2$  and  $sp^3$  carbon atoms, e.g.  $j=9, 19, 24, 26$ , and  $28$ , whose realization probabilities are enhanced for higher temperatures.

The magnetic properties of the clusters were investigated within spin-polarized simulations, considering ferromagnetic and antiferromagnetic initial configurations. In agreement with investigations made by Wang *et al.* (WANG *et al.*, 2011), some arrangements of hydroxyl groups on the graphene sheet may exhibit ferromagnetism, electrons with unpaired spins and non-zero magnetic moment for the ground state, e.g.  $j=13, 14$ , and  $23$ . All the configurations with excess energy  $\Delta E_j < 1.5$  eV/cluster, exhibit nonmagnetic ground states. In addition, we verified that class  $j = 27$  exhibits an antiferromagnetic ground state. One observes that hydroxyl arrangements with such ferromagnetic and antiferromagnetic properties are restricted to large excess energies and, therefore, their realization is suppressed by thermodynamics. The average magnetic moment per cluster was calculated for the typical growth temperatures and no significant magnetization was verified.

Studying the electronic properties, we focus on the fundamental energy gap of each configuration and their average value versus oxidation level  $x$ . The definition of a fundamental gap is sometimes difficult in the case of oxidation via hydroxyl groups. The delocalized 2D  $\pi$ -electron distribution observed in graphene is locally or globally distorted by adsorption

of hydroxyl groups. A  $Cp_z$  orbital is filled with one electron which is attracted to the oxygen atom of the  $-OH$  group to form a noble gas octet shell. The interaction and  $\pi$ -bonding of the remaining  $Cp_z$  orbitals may lead to insulating or metallic cluster systems. This is illustrated in Fig. 5.8 for two clusters with an odd number of hydroxyls performing spin-polarized calculations. The 0000000+ ( $j=2$ ) cluster class exhibits in Fig. 5.8 (a) an insulating electronic structure, with a splitting of the energy bands with different spin components large enough, so that only fully occupied or empty bands are observed. Therefore, an energy gap can be determined for such a configuration. In Fig. 5.8 (b) the electronic band structure of 000+0+0+ ( $j=10$ ) cluster class is illustrated, exhibiting half-occupied bands and, therefore, a metallic behavior.

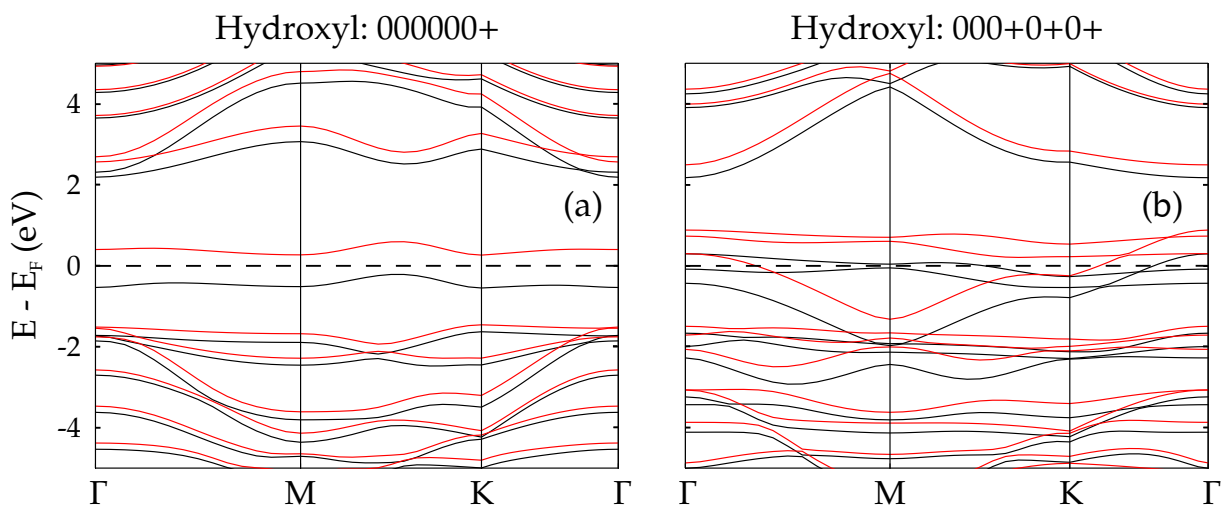


FIGURE 5.8 – Electronic band structures for cluster class configurations decorated with an odd number of hydroxyl groups per cluster obtained from spin-polarized PBE calculations. The Fermi energy level is chosen as the reference. One observes that (a) 0000000+ ( $j=2$ ) cluster arrangement exhibit for each different spin channel fully (un)occupied bands, showing an insulating electronic structure; (b) 000+0+0+ ( $j=10$ ) cluster class exhibits half occupied bands, being therefore a metallic atomic arrangement.

Fortunately, the cluster classes identified to be metallic usually have large excess energies. For that reason, we can take them into the calculation of the average fundamental gaps, since their occurrence probability is extremely small. A gap curve for intermediary compositions is obtained within GQCA approach, weighting the fundamental gaps of the different 31 cluster configurations listed in Table 5.1 for each oxidation level. The obtained curves are depicted in Fig. 5.9 for three preparation temperatures.

The comparison of the gap values computed within different XC approaches in Table 5.1 shows that the hybrid functional enhances the fundamental energy gaps of semiconductor and insulator configurations compared with the PBE functional. In addition, for six highly oxidized configurations that were predicted within PBE calculations to have a metallic behavior, finite band gaps are calculated within the hybrid functional description (see Table 5.1).

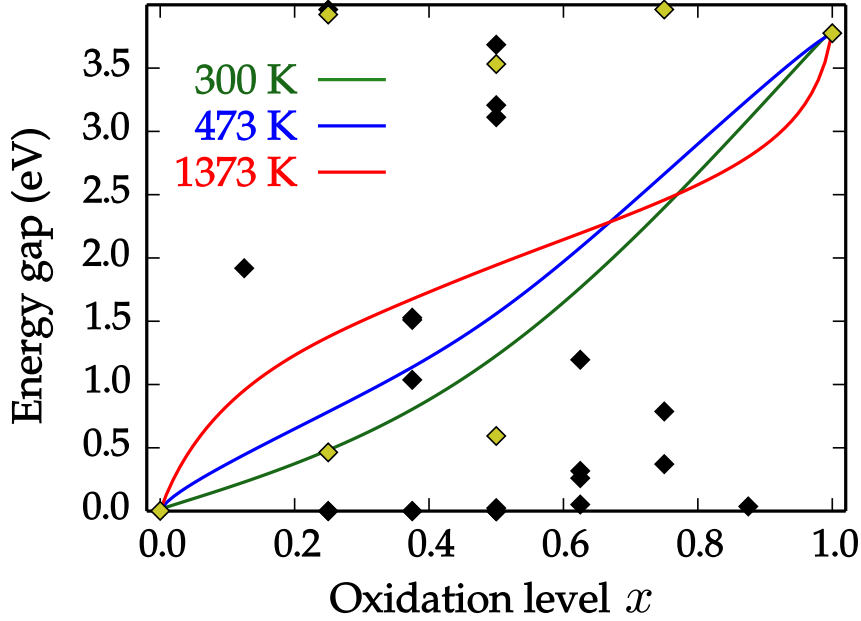


FIGURE 5.9 – Energy gap curve of graphene functionalized with hydroxyl groups as a function of the oxidation level within HSE06 framework. The diamonds represent the HSE06 energy gaps of all the cluster configurations considered, the set of cluster configurations with  $\Delta E_j < 1.5$  eV/cluster are represented as golden diamonds, while the complementary set is represented with black diamonds. Metallic behavior is identified with a zero energy gap.

When the electronic properties are related to the excess energies, one observes a clear relationship between high excess energies and metallic behavior: all the configurations predicted to be metallic exhibit excess energies per cluster above 2.5 eV. Therefore, the realization of these high-energy  $-OH$  distributions is energetically less probable, i.e. these configurations are unfavorable. However, these configurations influence the average energy gap curve versus composition in Fig. 5.9, in particular for higher temperatures. For lower temperatures, the energy gap curve is monotonically crescent, despite of the existence of metallic configurations, and only a small gap bowing is visible. For higher temperatures the energy gap curve becomes S-shaped. Larger gap systems with excess energies  $\Delta E_j$  near 2 eV influence the findings. Figure 5.9 shows that, independently of the preparation temperature, the gap can be tuned between tenths of eV until about 3.5 eV with the coverage by  $-OH$  groups. The big dispersion of energy gaps  $E_{g,j}^{HSE}$  of the considered clusters and the temperature influence of the average energy gap curves observed in Fig. 5.9 show the importance of taking statistics and growth conditions into account. These results are in agreement with other calculations with a screened hybrid functional (JIANG *et al.*, 2013), but also measurements of typical band gaps of 2.3-3.6 eV (YEH *et al.*, 2011), 3.26 eV (KRISHNAMOORTHY *et al.*, 2012), 3.6 eV (PENG *et al.*, 2012), and 2.4-4.3 eV (YEH *et al.*, 2010) for graphene oxides.

The effect of synthesis temperature can be observed comparing the curves for  $T = 300$

K, 473 K and 1373 K in Fig. 5.9. As the temperature increases, more configurations with larger excess energies have a bigger statistical relevance and change the average energy gap curve profile. When low-oxidation levels are considered, this effect leads to enhanced occurrence probabilities of configurations with intermediate oxidation levels with larger fundamental energy gaps. For high oxidation levels, the average oxidation level constraints the statistics favoring configurations with more hydroxyl groups, and the temperature increase results into smaller energy gaps due a probability enhance of the  $0+-+--+$  configuration.

In Fig. 5.10(a) we display the absorbance spectra considering average oxidation levels  $x = 0.25, 0.50$  and  $0.75$  considering local composition fluctuation effects, i.e. homogeneous alloys, at  $T = 473$  K and  $1373$  K according to Eq.2.83. For low temperature, one can observe that the absorbance spectra progressively change from the graphene pattern to the absorbance spectra of a fully decorated graphene sheet with  $-OH$  groups (see Fig. 5.4). At an oxidation level  $x = 0.50$  a very wide absorbance range is expected in this case. The increase of temperature at  $x = 0.25$  exhibits a secondary adsorption peak around  $2.5$  eV mainly associated with the  $0000000+$  ( $j=2$ ) configuration. The effect of complete phase segregation is illustrated in Fig. 5.10(b) as obtained from Eq.2.83. In this case, the  $j=2$  cluster class still significantly contributes to the average spectrum, especially for higher temperature. However, the qualitative behavior of the optical spectra of fully phase segregated systems is dominated by the absorbance peaks associated with the graphene and fully oxidized GO phases, when the complete phase segregation is considered.

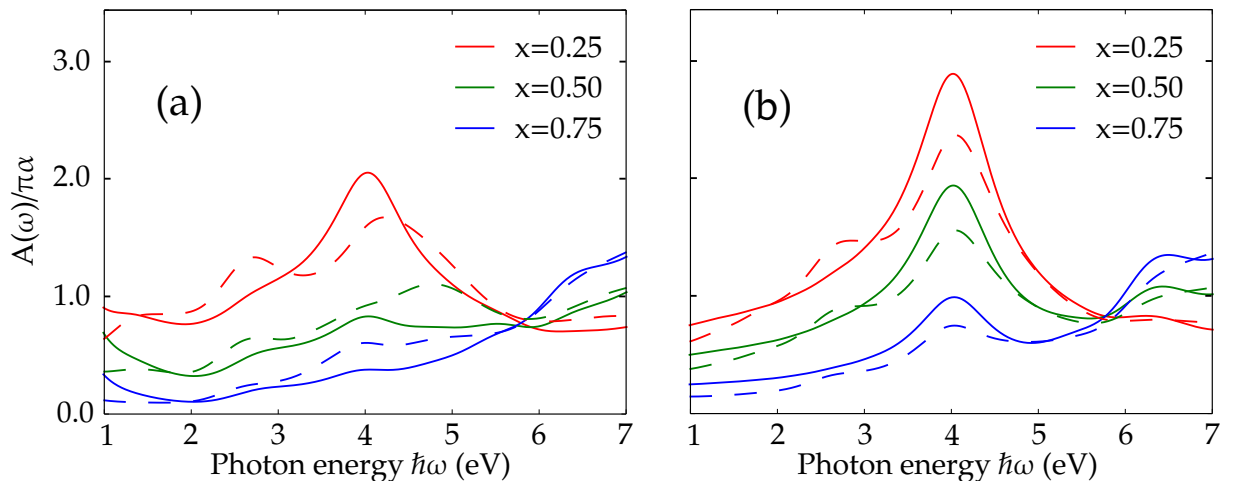


FIGURE 5.10 – Average optical absorbance as a function of the photon energy for GO systems decorated with  $-OH$  groups with oxidation levels  $x=0.25, 0.50,$  and  $0.75,$  represented as red, green and blue curves, respectively. The average spectra are calculated at  $T = 473$  K (full lines) and  $1373$  K (dashed lines). The adsorption spectra predictions are calculated considering only local composition fluctuations, i.e. a homogeneous alloy (a), and complete phase segregation (b).

## 5.5 Partial epoxy oxidation

We consider 689 possible arrangements, containing between  $n_{\text{epo},j} = 0$  and  $n_{\text{epo},j} = 4$  epoxy groups per 2x2 cluster cell, which can be organized in  $J_{\text{epo}} = 24$  symmetry-equivalence classes with different degeneracies  $g_j$  (see Table 5.2).

TABLE 5.2 – Cluster classes  $j$ , their labels, their degeneracies  $g_j$ , numbers of epoxys groups per cluster  $n_{\text{epo},j}$ , excess energies  $\Delta E_j$  per cluster and fundamental energy gaps from PBE ( $E_{g,j}^{PBE}$ ) and HSE06 calculations ( $E_{g,j}^{HSE}$ ).

$j$	Label	$n_{\text{epo},j}$	$g_j$	$\Delta E_j$ (eV)	$E_{g,j}^{PBE}$ (eV)	$E_{g,j}^{HSE}$ (eV)
1	000000000000	0	1	0.00	Metal	Metal
2	00000000000+	1	24	0.96	0.63	0.82
3	00000++00000	2	12	1.67	1.67	3.30
4	00000+-00000	2	12	1.09	2.52	3.81
5	000000000++0	2	24	1.48	0.49	0.95
6	000000000+-0	2	24	0.67	0.13	0.42
7	0000000000++	2	48	1.74	1.41	2.35
8	0000000000+-	2	48	1.15	1.98	2.92
9	0000++0000+0	3	16	3.69	Metal	0.03
10	0000++0000-0	3	48	3.00	Metal	Metal
11	00000++0000+	3	24	1.95	1.96	3.64
12	00000++0000-	3	24	0.63	2.34	3.78
13	00000+-0000+	3	48	0.73	3.30	4.50
14	000000++000+	3	48	2.17	2.53	3.84
15	000000++000-	3	96	0.74	2.81	4.03
16	000000+-000+	3	48	0.98	2.95	4.17
17	00++00000++0	4	6	2.21	3.37	4.81
18	00++00000+-0	4	24	0.64	3.32	5.17
19	00++00000- -0	4	12	0.03	4.52	6.37
20	00+-00000+-0	4	6	0.00	3.12	5.05
21	00+00+0000++	4	12	2.81	3.96	5.58
22	00+00+0000+-	4	48	0.77	4.31	6.24
23	00+00+0000- -	4	24	0.01	4.09	5.50
24	00+00-0000+-	4	12	0.29	4.36	6.33

In Fig. 5.12 the excess energies of the 24 cluster classes listed in Table 5.2 are plotted as a function of the number of epoxy groups adsorbed per cluster. One observes that the configurations with alternated epoxy groups on top and below the graphene sheet have lower excess energies, as verified for classes 00++00000-0 ( $j=19$ ), 00+-00000+-0 ( $j=20$ ), and 00+00+0000- ( $j=23$ ). These energy favored configurations are depicted in Fig. 5.11. Cluster configurations with epoxy exposure just on one side of the carbon sheet result in larger excess energies, as occurs for the 0000000000++ ( $j=7$ ), 0000++0000+0 ( $j=9$ ) and 00+00+0000++ ( $j=21$ ) cluster classes. In average, the excess energies  $\Delta E_j$  are smaller for the -O- groups (Table 5.2) compared to the -OH groups (Table 5.1). Apart from

zero-gap graphene the two cluster classes  $j = 9$  and 10 with the largest excess energies again tend to be metallic.

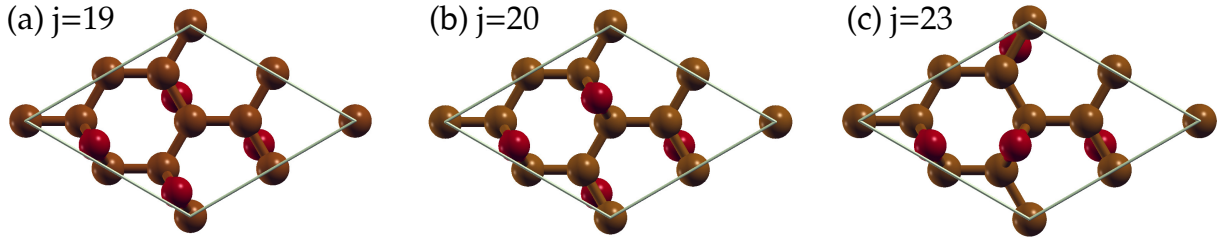


FIGURE 5.11 – The most energetically favored ( $\Delta E_j \leq 0.03$  eV) graphene oxide cluster configurations with complete epoxy decoration ( $n_{\text{epo},j} = 4$ ): (a) 00++00000–0, (b) 00++00000+–0, and (c) 00+00+0000–. The indicated cluster numbering  $j$  refers to Table 5.2. Carbon and oxygen and hydrogen atoms are respectively represented by brown and red spheres.

The cluster configurations with  $n_{\text{epo},j} = 4$ , apart configurations  $j=17$  and 21 which have epoxy groups only at on side of the graphene sheet, possess very small excess energies. Therefore, for the oxidation level  $x = 1$ , the fully oxidized system represents a structurally disordered system composed by clusters with a complete occupation by –O– groups (as discussed in Sec. 5.3). The configurations  $j = 19, 20$ , and 23 with  $n_{\text{epo},j} = 4$  and almost vanishing excess energies can be considered as ordered structures, i.e. as alternating arrangements of –O– groups along armchair directions ( $j=20$ ). However, because of the chosen 2x2 cells no isolated chains can be extracted as in the case of 5x5 cells (JIANG *et al.*, 2013; WANG *et al.*, 2010).

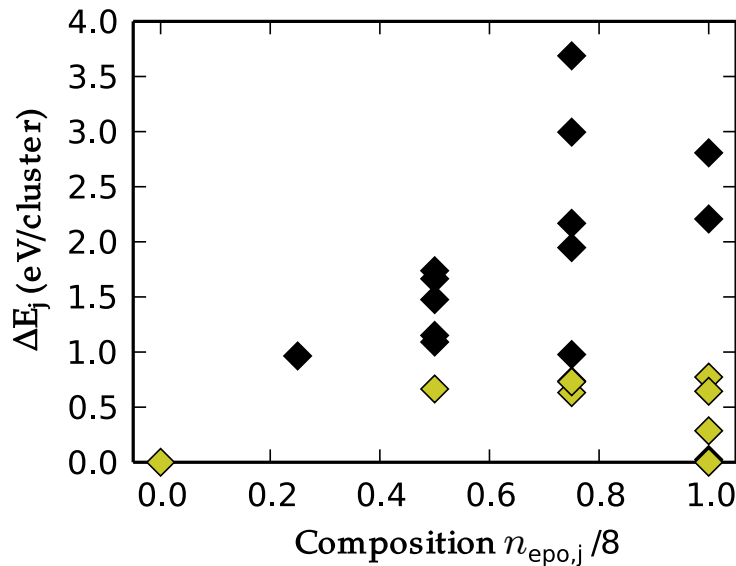


FIGURE 5.12 – Excess energies  $\Delta E_j$  of cluster configurations functionalized with hydroxyl groups as function of the number of oxygen groups per cluster  $n_{\text{epo},j}$ . The cluster configurations with  $\Delta E_j < 0.8$  eV/cluster are represented as golden diamonds, while the complementary set is represented in black.

A  $T$ - $x$  phase diagram of graphene functionalized with epoxy groups is constructed and displayed in Fig. 5.13. A critical temperature  $T_{c,epo} = 3550$  K is calculated. One can verify that temperatures above 500 K result in a pronounced increase of the possible range of oxidation level in which stable homogeneous phases can be obtained. One observes that the asymmetry of excess energies  $\Delta E_j$  distribution in Fig. 5.12 is not reflected in the  $T$ - $x$  phase diagram displayed in Fig. 5.13. This result is explained by the fact that clusters with high oxidation levels and excess energies above 2.0 eV/cluster have significantly lower statistical weights than the ones with lower excess energies for  $T < T_{c,epo}$ .

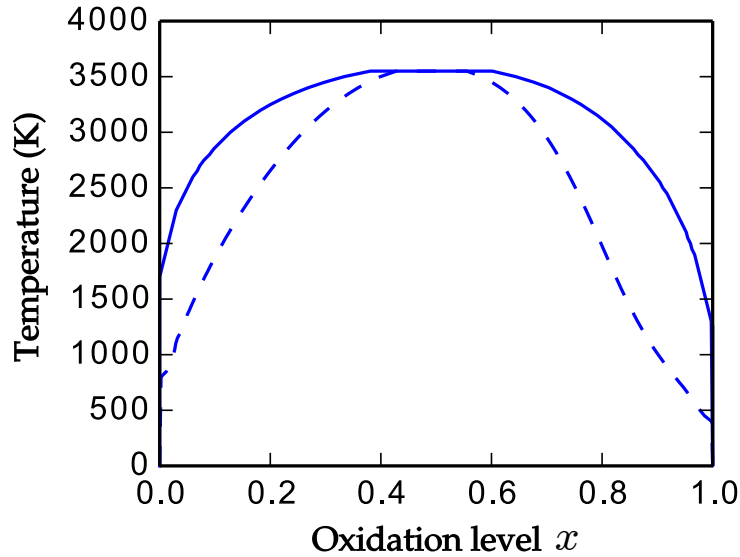


FIGURE 5.13 – The  $T$ - $x$  phase diagram of graphene functionalized with epoxy groups. The binodal (spinodal) curve is represented by the full (dashed) line.

Comparing the two phase diagrams in Figs. 5.7 and 5.13, a tendency is visible that the epoxy groups are more likely to produce homogeneous phases with partial oxidation than hydroxyl groups. The phase diagram in Fig. 5.13 displays a wide range between the spinodal and binodal curves. This fact indicates that for low and high oxygen compositions the decomposition of the alloy into graphene and graphene oxide phase can be hampered.

The GQCA approach predicts an almost linear behavior of the lattice constant as a function of the oxidation level  $x$ , with deviations not larger than  $0.006 \text{ \AA}$ . Therefore, understoichiometric graphene oxides covered by epoxy groups follow Vegard's law (DENTON; ASHCROFT, 1991; VEGARD, 1921). The average buckling amplitude for intermediate oxidation levels can be well approximated as  $\Delta(x) = (1-x)\Delta_C + x\Delta_{epo}(T) - bx(1-x)$ , where the bowing parameters for  $T = 473$  K and  $1373$  K are respectively  $-0.27 \text{ \AA}$  and  $-0.42 \text{ \AA}$ , i.e. exhibit an anti-bowing. The lengths and angles between oxygen bonds in the epoxy groups show no significant changes versus the oxidation level. Therefore, we conclude that the geometry of the epoxy groups is rather insensitive to the occupation and the orientation of the  $-\text{O}-$  groups.

Energy gap curves are plotted versus composition in Fig. 5.14. The average gap curve

for epoxy functionalization varies between 0 eV and 5.58 eV according to the oxidation level of the samples made by understoichiometric graphene oxide. As a general tendency the addition of epoxy groups leads to an enhancement of the fundamental gap. This can be observed both in the average gap curve but also for the energy gap of the considered clusters. The energy gap curves are calculated at  $T = 300$  K, 473 K and 1373 K for comparison. One sees that the increase of the growth temperature results in a larger bowing parameter of the energy gap curve. However, the temperature dependence is less pronounced compared with the hydroxyl oxidation. A striking effect of the epoxy treatment is a further increase of the gap compared to the hydroxyl oxidation (see Fig. 5.9) in agreement with other *ab initio* studies (JIANG *et al.*, 2013). The photoluminescence measurement of graphene samples subjected to  $O_2$  plasma and annealing at  $250$  °C show emission in the 350-850 nm wavelength range with a maximum emission near a photon energy of 2 eV (NOURBAKHSH *et al.*, 2010). Fluorescence studies of as-synthesised GO and such underlying a controlled deoxidation by hydrazine vapor exhibit values slightly below our prediction of about 5.6 eV for a complete decoration of graphene with epoxy groups.

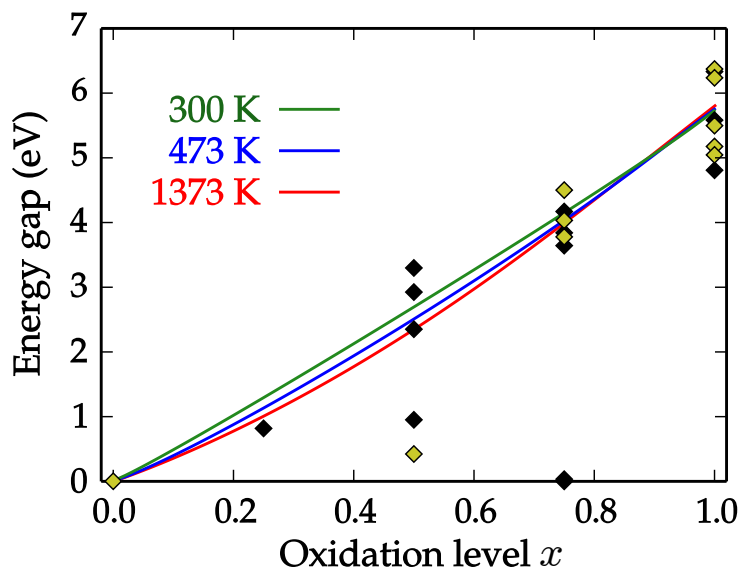


FIGURE 5.14 – Energy gap curve of graphene functionalized with epoxy groups as a function of the oxidation level within HSE06 framework. The diamonds represent the HSE06 energy gaps of the all the cluster configurations considered, the set of cluster configurations with  $\Delta E_j < 0.8$  eV/cluster are represented as golden diamonds, while the complementary set is represented with black diamonds. Metallic behavior is identified with zero energy gap.

Similarly to the case of graphene decoration with  $-OH$  groups, we have calculated average absorbance spectra for graphene decorated with epoxy groups for oxidation levels  $x = 0.25$ , 0.50 and 0.75 at  $T = 473$  K and 1373 K. Figure 5.15(a) illustrates the optical absorption taking only composition fluctuations into account as in homogeneous alloys. Three peaks can be identified around 1.5 eV, 4.0 eV and 7.0 eV depending on the composition and temperature. The peak at 1.5 eV is mainly associated with 00000000000+

( $j=2$ ), especially for small oxidation levels and high temperatures. The peak near 4.0 eV is associated not only to the graphene cluster class ( $j=1$ ) but also to configurations with intermediate oxygen composition as  $j=8, 12, 13$ , and 16, which give rise to a peak broadening increasing the preparation temperature for  $x=0.50$ , for example. The peak in the UV region is associated with the average of the fully oxidized cluster configurations with  $-O-$  groups. When the phase segregation effect is considered, as illustrated in Fig. 5.15(b), the statistical weight of configurations with intermediate oxidation levels is suppressed, and the intensity of the peak at 1.5 eV and the spectra dependence on the temperature become less pronounced.

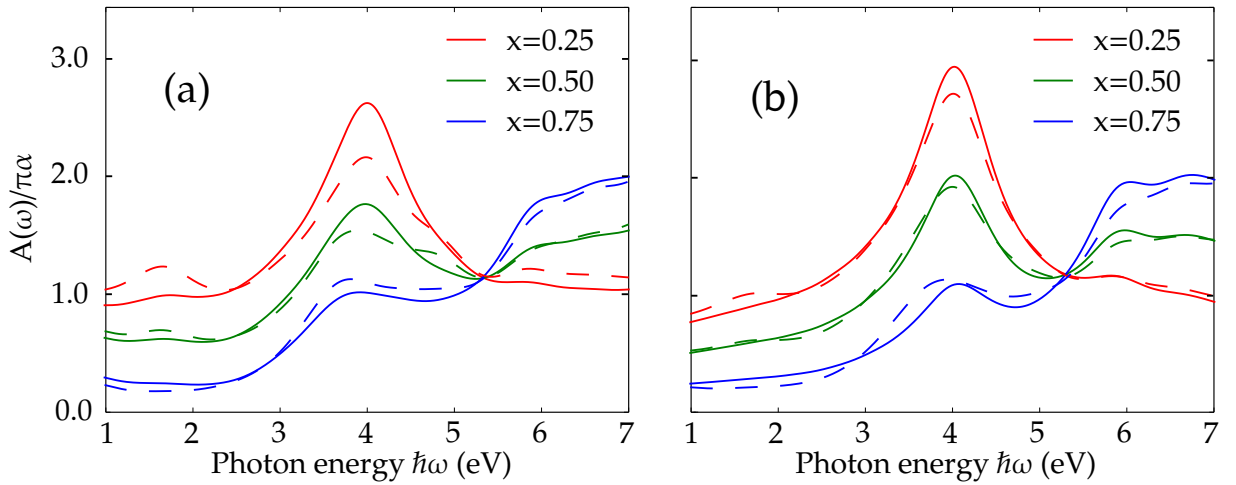


FIGURE 5.15 – Average optical absorbance as a function of the photon energy for GO systems decorated with  $-O-$  groups with oxidation levels  $x=0.25, 0.50$  and  $0.75$ , represented as red, green and blue curves, respectively. The average spectra are calculated at  $T = 473$  K (full lines) and  $1373$  K (dashed lines). The adsorption spectra are calculated considering local composition fluctuations, i.e., homogeneous alloys (a), and complete phase segregation (b).

## 5.6 Simultaneous oxidation with hydroxyl and epoxy groups

### 5.6.1 Thermodynamic stability

The energetics of the clusters classes is investigated by defining the excess total energy of each atomic arrangement as

$$\Delta E_j = E_j - \frac{n_{C,j}}{8} E_C - \frac{n_{OH,j}}{8} E_{COH} - \frac{n_{O,j}}{4} E_{CO_{1/2}}, \quad (5.1)$$

where  $n_{C,j}$  represents the number of three-fold coordinated carbons in cluster class  $j$ .

Expression (5.1) represents the formation energy of a cluster class  $j$ , with respect to the three end components, pure graphene with total energy  $E_C$ , fully oxidized GO with only  $-\text{OH}$  groups and energy  $E_{\text{OH}}$ , and fully oxidized GO with only  $-\text{O}-$  groups and energy  $E_{\text{CO}_{1/2}}$ . The atomic geometry of the end components are displayed in Figs. 5.16 a, b, and c, which illustrate graphene ( $x=1$ ), a cluster fully decorated with hydroxyl ( $y=1$ ), and 00000000-00ud00000ud0, the cluster class with four epoxy groups per cluster ( $z=1$ ) with the lowest internal energy. Configurations with large excess total energies  $\Delta E_j$  are inhibited by the minimization of the Helmholtz mixing free energy. They are realized only at high growth temperatures, while configurations with negative formation energy indicate that such atomic arrangements are thermodynamically favored and realized even for low temperatures.

In previous sections, we reported only positive excess energies for oxidation of graphene sheets with hydroxyl or epoxy groups. If only one oxidant group is adsorbed on an atomic sheet, the GO system tends to decompose into oxygen-poor and -rich domains. Here, we investigate the simultaneous oxidation with  $-\text{OH}$  and  $-\text{O}-$  groups and explore new features that emerge from the interaction between both oxidant groups.

The vast majority of cluster configurations still exhibits positive excess energies, especially for understoichiometric configurations. However, eight different classes of fully oxidized configurations with hydroxyl and epoxy groups exhibit negative excess energies, indicating great energetic stability even at low temperatures. Four of these configurations with negative excess energies occur at  $(n_{\text{C},j}/8, n_{\text{OH},j}/8, n_{\text{O},j}/4) = (0, 0.5, 0.5)$ , corresponding to four  $-\text{OH}$  and two  $-\text{O}-$  groups per 8-carbon cluster. The other four energetically favorable arrangements occur at  $(n_{\text{C},j}/8, n_{\text{OH},j}/8, n_{\text{O},j}/4) = (0, 0.25, 0.75)$ , corresponding to two  $-\text{OH}$  and three  $-\text{O}-$  per cluster. These findings agree with the indication by NMR measurements that to a large extent hydroxyl and epoxy groups prefer to oxidize carbons simultaneously (CAI *et al.*, 2008), and theoretical works that indicate the total energies are considerably lowered when epoxy and hydroxyl groups are adsorbed together (YAN *et al.*, 2009; YAN; CHOU, 2010). Oxidized domains with both oxidant groups are, therefore, thermodynamically favored over a spatial segregation of the oxidant groups. The lowest energy configurations at  $(n_{\text{C},j}/8, n_{\text{OH},j}/8, n_{\text{O},j}/4) = (0, 0.5, 0.5)$  and  $(0, 0.25, 0.75)$  are u0d00d0u-00000ud00000 and d000000d-0000uu0000u0, respectively, which are illustrated in Figs. 5.16 d and e.

The thermodynamic stability of the graphene oxide systems with respect to its chemical composition is investigated by the mixing free energy  $\Delta F(x, y, T)$  at typical growth temperatures of  $200^\circ\text{C}$  and  $1100^\circ\text{C}$  (MARCANO *et al.*, 2010; JUNG *et al.*, 2009; EDA; CHHOWALLA, 2010; DREYER *et al.*, 2010), considering all possible chemical compositions  $x = 1 - y - z$ ,  $y$ , and  $z$ . The results are represented by the two color maps depicted in Fig. 5.17. The most favorable configurations of the three end components C (graphene), COH (GO with

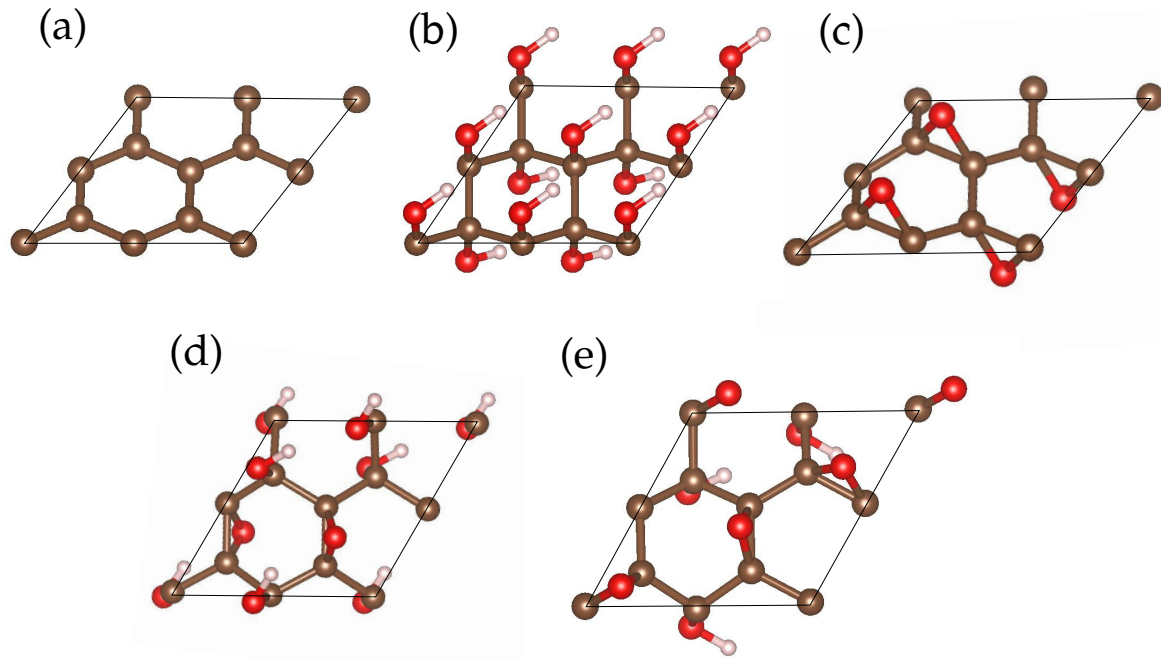


FIGURE 5.16 – Important cluster configurations representing (a) pristine graphene, (b) COH, (c) 00000000-00ud00000ud0, which corresponds to the most energetically favored cluster fully oxidized by epoxy groups, (d) u0d00d0u-00000ud00000, with  $\Delta E_j = -0.72$  eV/cluster, and (e) d00000d-0000uu0000u0, with  $\Delta E_j = -0.67$  eV/cluster. Carbon, oxygen and hydrogen atoms are respectively represented by brown, red and grey spheres.

hydroxyl), and  $\text{CO}_{1/2}$  (GO with epoxy) are chosen as the corner points of the displayed triangles. Their edges represent the variation of one composition  $x$ ,  $y$ , or  $z$ , while the other two compositions are zero. The oxidation processes with one single oxidant group, which correspond to the  $\text{C}-\text{COH}$  and  $\text{C}-\text{CO}_{1/2}$  edges of the color maps, exhibit positive mixing energies for lower temperatures, indicating strong phase decomposition tendency. When higher temperatures are considered, the entropy term becomes more important and contributes to the system stability for intermediate oxidation level, which very intense for highly oxidized limit of  $\text{C}-\text{CO}_{1/2}$  edge, being represented in green color.

For intermediate oxidation levels, for both chosen growth temperatures, the red and orange areas indicate an enhance of mixing free energy, and, therefore, a strong tendency for phase decomposition into pristine graphene (C vertex) and fully oxidized domains with both oxidants ( $\text{CO}_{1/2}$ -COH edge). These results are in agreement with other theoretical investigations (YAN *et al.*, 2009; YAN; CHOU, 2010; ZHOU; BONGIORNO, 2013) and experimental findings that non-oxidized domains may exist in GO samples (HE *et al.*, 1998; LERF *et al.*, 1998).

The reasons for the gain of mixing free energy along the  $\text{COH}-\text{CO}_{1/2}$  edges of the color maps in Fig. 5.17 are illustrated in Fig. 5.18. The mixing free energy  $\Delta F$  is decomposed into the internal energy contribution  $\Delta U$  and the configurational entropy term  $-T\Delta S$ . The mixing free energy  $\Delta F$  is dominated by the entropy contribution  $-T\Delta S$  at high

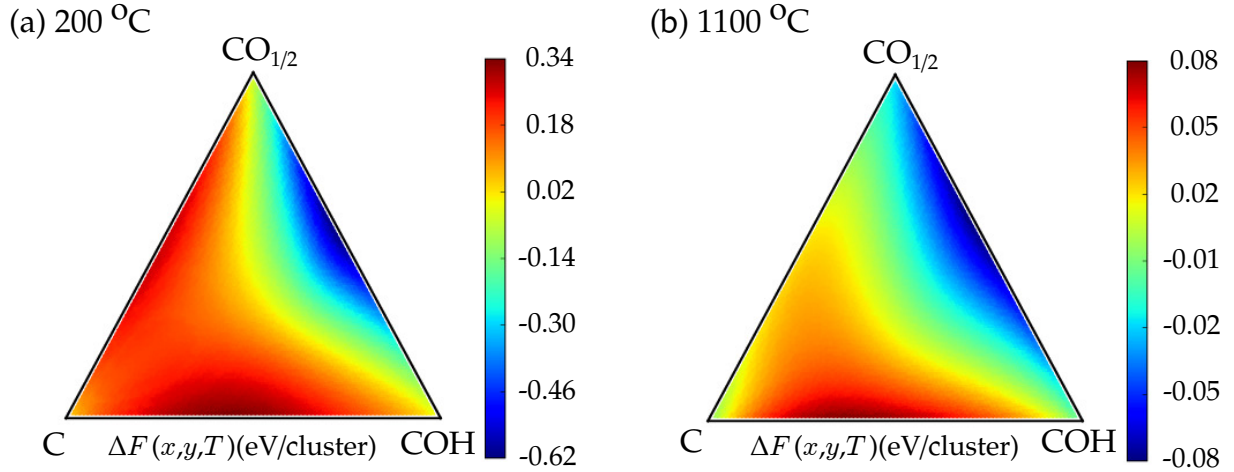


FIGURE 5.17 – The mixing free energy of the understoichiometric GO systems as a function of the average compositions at synthesis temperature of (a)  $200^{\circ}\text{C}$  and (b)  $1100^{\circ}\text{C}$ .

temperatures. However, for low temperatures, the occurrence of atomic arrangements with negative excess energies is reflected on  $\Delta U$ . After the cluster statistics is considered, fully oxidized domains decorated with hydroxyl and epoxy groups are demonstrated to be stable for both considered growth temperatures.

In the hydroxyl-rich limit ( $y \rightarrow 1$ ), nearly all clusters correspond to the COH end component. This situation leads to  $\Delta U = 0$ , while an entropy per cluster of  $\Delta S = k_b \ln(2)$  is calculated by Eq.2.93 for the cluster expansion. Since  $g_{COH} = 2$ , the COH clusters are free to ‘flip’ independently from the oxidant groups in the neighborhood due to GQCA energetic independence between neighbor clusters hypothesis. In the epoxy-rich limit ( $z \rightarrow 1$ ) there is a competition between different possible epoxy arrangements in the sheets. At low temperature (see the solid lines in Fig. 5.18), the configurations with lower internal energy of mixing are strongly favored, yielding low  $\Delta U$  and  $\Delta S$ . As the temperature increases, the occurrence probability of cluster classes corresponding to more energetic configurations is enhanced, leading to larger  $\Delta U$  and  $T\Delta S$  contributions to the total excess free energy.

## 5.6.2 Structural properties

We obtained the lattice constants of  $a_C = 2.47 \text{ \AA}$ ,  $a_{COH} = 2.63 \text{ \AA}$  and  $a_{CO_{1/2}} = 2.57 \text{ \AA}$  for the pure end compounds. A maximum lattice mismatch of 7% is calculated between graphene, and GO with only  $-\text{OH}$  groups. Average lattice constants  $a(y, z, T)$  of the GO systems as a function of the chemical compositions are calculated within the GQCA statistics and depicted in Fig. 5.19. A gradual change between the end component lattice constant is observed and the linear fit  $a = xa_C + ya_{COH} + za_{CO_{1/2}}$  gives the calculated lattice constant with an maximal error below 1.5% for both considered temperatures. That

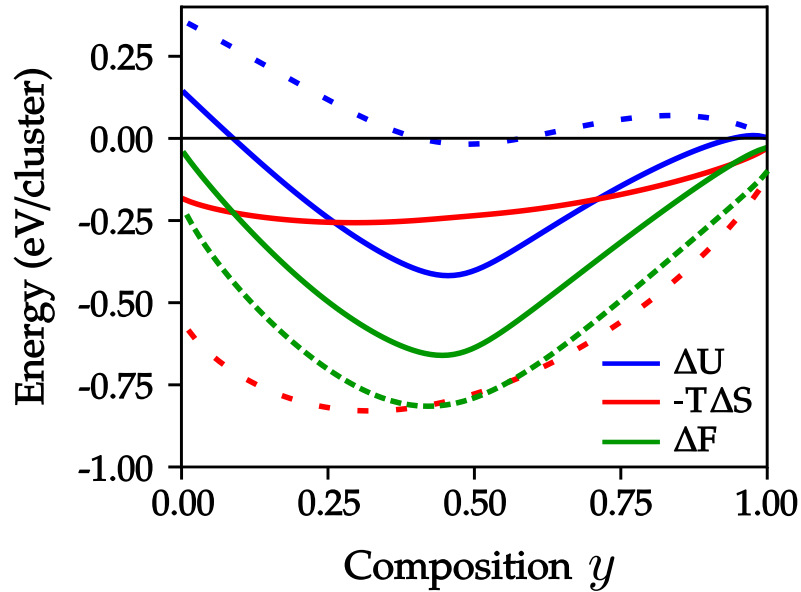


FIGURE 5.18 – The mixing internal energy  $\Delta U$ , free energy entropic contribution  $-T\Delta S$ , and mixing Helmholtz free energy  $\Delta F$  curves for a fully oxidized system  $(\text{COH})_y(\text{CO}_{1/2})_{1-y}$ . The solid lines are obtained for a growth temperature of  $200^\circ\text{C}$ , while the dashed lines are for a growth temperature of  $1100^\circ\text{C}$ . The zero-energy line is given as a guideline.

means that Vegard's rule is widely fulfilled.

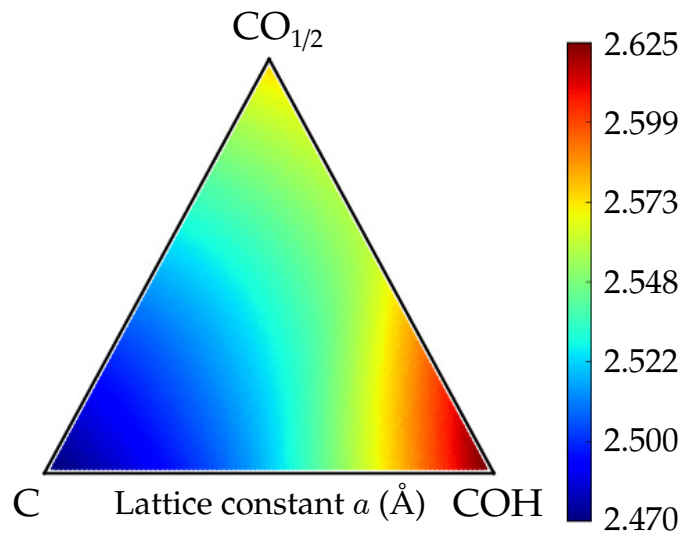


FIGURE 5.19 – The average lattice constant  $a$  of the GO systems calculated within the GQCA approach at synthesis temperature of  $200^\circ\text{C}$  as second-nearest neighbor C distances.

The buckling amplitude  $\Delta(y, z, T)$  of the carbon sheet is also investigated. The graphene layer exhibits a honeycomb planar structure with  $\Delta_j = 0.00 \text{ \AA}$ , while the COH system exhibits a buckling amplitude of  $\Delta_j = 0.51 \text{ \AA}$ , which is associated with a pure  $sp^3$  hybridization of the carbon atomic orbitals. The  $\text{CO}_{1/2}$  end component fully decorated by epoxy groups exhibits a different distortion of the planar honeycomb structure, depending on how the epoxy groups are distributed. Buckling amplitudes between  $\Delta_j = 0.00 \text{ \AA}$  and  $0.50 \text{ \AA}$  are observed, that results in an average buckling amplitude of  $0.36 \text{ \AA}$  for the

considered range of temperatures. The dependence of the average buckling amplitude  $\Delta(y, z, T)$  on the chemical compositions at 200°C is displayed in Fig. 5.20.

One observes a pronounced maximum buckling amplitude of 0.71 Å for fully oxidized graphene oxide systems with both oxidant groups in proportions near  $n_{\text{OH}}/n_{\text{O}} = 1$ , which is larger than any buckling amplitude observed in the end components. This is the result of large statistical contributions of configurations  $\text{u0d00d0u-00000ud00000}$  and  $\text{udud0000-00000ud0}$ , which are thermodynamically favored due to their negative excess energies ( $\Delta E_j = -0.72$  and  $-0.58$  eV/cluster, respectively). They exhibit buckling amplitudes significantly larger than the pure  $sp^3$  buckling ( $\Delta_j = 0.75\text{Å}$  and  $0.62$ , respectively). This is due the fact that some  $-\text{OH}/-\text{O}-$  distributions induce low energy long-range distortions of the planar honeycomb structure.

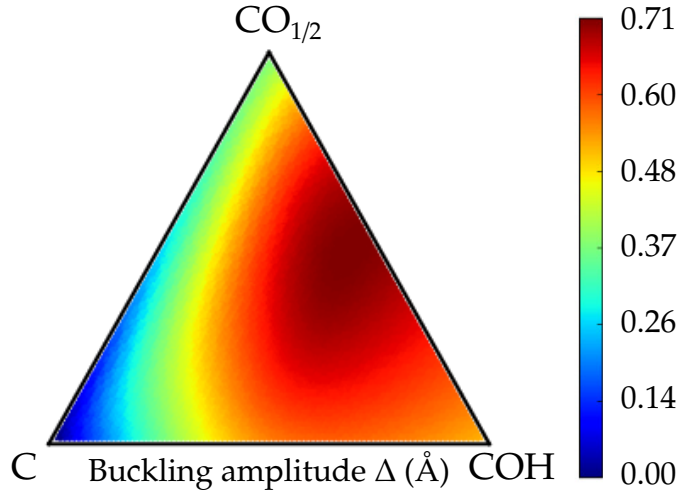


FIGURE 5.20 – The average buckling amplitude  $\Delta$  of the GO systems calculated within the GQCA approach at synthesis temperature of 200°C.

The most stable configuration at  $(x, y, z) = (0, 0.5, 0.5)$  exhibits alternated stripes of carbon atoms synthesized by hydroxyl and epoxy groups, as illustrated in Fig. 5.16(d), which is constituted by an small-range stripe-like pattern of carbons oxidized by hydroxyl and epoxy groups. The most stable configuration at  $(x, y, z) = (0, 0.25, 0.75)$  shows a new discovered favorable structure, constituting of hexagons synthesized by epoxy groups embedded by carbons synthesized by  $-\text{OH}$  groups. This can be verified by the 2D-periodic repetition of the structure illustrated by Fig. 5.16(e).

### 5.6.3 Electronic and optical properties

The qualitative aspects of electronic and optical properties of the 308 cluster configurations are investigated within the GGA-PBE exchange and correlation functional. This pure DFT approach leads to fundamental energy gaps of  $E_{g,\text{C}} = 0$  eV,  $E_{g,\text{COH}} = 2.25$  eV, and  $E_{g,\text{CO}_{1/2}} = 4.00$  eV at 200 °C for the considered end components. As we demonstrated for

adsorption of one oxidant group on the graphene sheet in Sec. 5.4 and 5.5, the Kohn-Sham energy gap values obtained within GGA-PBE functional show the same trends as those computed with screened hybrid functionals.

The fundamental energy gap depends on the stoichiometry, i.e., the general oxidation state of the GO but also the average compositions  $y$  and  $z$  related to oxidation by means of the hydroxyl and epoxy groups, respectively. The average gap  $E_g(y, z, T)$ , however, not only depends on the average compositions  $x$ ,  $y$ , and  $z$  and the growth temperature  $T$  but also on the fluctuations from the average compositions. They lead to deviations of the gaps from its linear behavior with the compositions, the so-called gap bowing, due to the convex behavior of the curves. We investigate the energy gap bowing  $\Delta E_g(y, z, T)$  defined as

$$E_g(y, z, T) = xE_{g,C} + yE_{g,COH} + zE_{g,CO_{1/2}} + \Delta E_g(y, z, T). \quad (5.2)$$

An estimate of the absolute values of the energy gap can be made by applying a scissor operator approximation, considering quasiparticle corrections to the fundamental energy gaps of the COH and  $CO_{1/2}$ , and the gap bowing estimated from the GGA-PBE calculations. The average gaps are calculated within GQCA at  $200^\circ\text{C}$  and  $1100^\circ\text{C}$ . The energy gap bowings  $\Delta E_g(y, z, T)$  obtained using the gaps  $E_{g,j}$  for each configuration class  $j$  and formula (2.77) ruled by the statistical weights  $x_j$  for the considered growth temperatures are depicted in the color maps in Fig. 5.21.

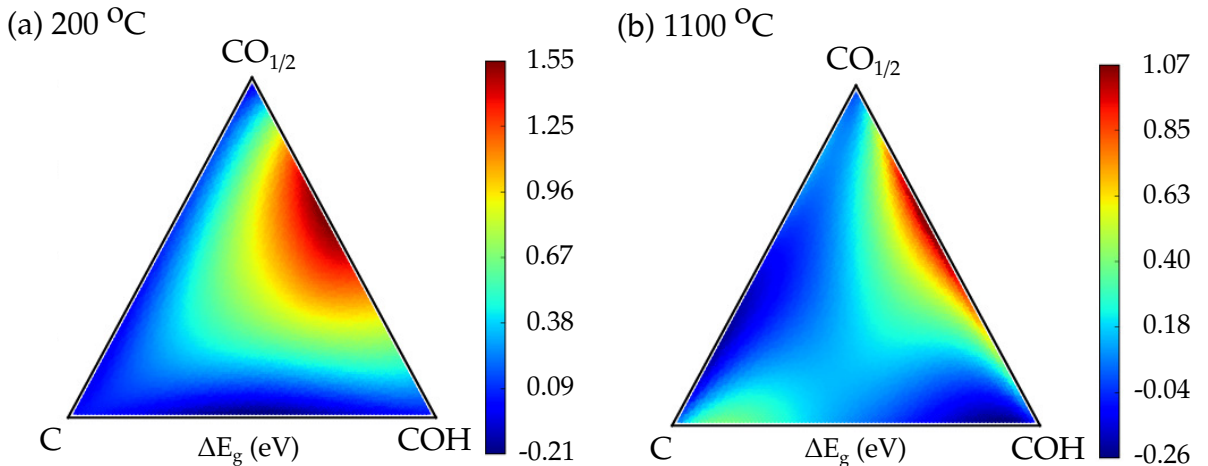


FIGURE 5.21 – The average energy gap bowing of the GO systems as a function of the average compositions at growth temperature of (a)  $200^\circ\text{C}$  and (b)  $1100^\circ\text{C}$ .

In agreement with previous results for graphene oxide systems decorated with single oxidant groups, the energy gap bowing for a  $-\text{O}-$  rich oxidation does not significantly change with temperature increase, while the energy gap bowing for a  $-\text{OH}$  rich oxidation changes from regular bowing ( $\Delta E_g < 0$ ) at  $200^\circ\text{C}$  to a profile that may exhibit regular

bowing or anti-bowing ( $\Delta E_g > 0$ ) at 1100°C, depending on the oxidation level of the system. The gap bowings along the C–CO<sub>1/2</sub> edge are almost given as  $\Delta E_g(x, T) = -b(T)x(1-x)$ , while along the C–COH edge the gap may exhibit positive and negative bowing depending on the chemical composition for large growth temperatures.

The energy gap bowing along the CO<sub>1/2</sub>–COH edge ( $y = 1-z$ ), i.e., for the simultaneous deposition of –OH and –O– groups in the limit of complete oxidation, exhibit larger values for  $\Delta E_g$  for fully oxidized systems with –O–/–OH ratios between 1 and 3 for both growth temperatures. This enhancement of the energy gaps is explained by the significant contributions of favorable configurations with negative excess energies and large energy gap values, e.g., 4.40 eV (u0d00d0u–00000ud00000) and 4.68 eV (d000000d–0000uu0000u0). The application of a statistical approach on a larger set of configurations results into an even larger energy gap range for band gap engineering than the one obtained by Yan *et al.* (YAN *et al.*, 2009; YAN; CHOU, 2010), who suggested an obtained energy gap bowing between 0.8-1.1 eV for fully oxidized configurations, when the system is prepared at low growth temperature. Our calculated  $\Delta E_g(x, T)$  values are depicted in Fig. 5.21 indicate significant changes for different temperatures.

The increase of the growth temperature induces more configurational disorder in the GO system and the contributions of the configurations with lower energies decrease with the rising temperature. One verifies this effect by the shrinkage of the red area in Fig. 5.21(b), compared with Fig. 5.21(a). This result shows the big potential of graphene oxide to provide a 2D platform for novel 2D electronics, whose electronic properties can be tuned controlling both the chemical composition and growth conditions. Thereby, the coadsorption of hydroxyl and epoxy groups opens a new tune window not only in the limit of full oxidation but also for intermediate decorations with structures similar to those in Figs. 5.16 d and e.

The gap bowing  $\Delta E_g(y, z, T)$  illustrated in Fig. 5.21 can be fitted with the following expression

$$\Delta E_g(y, z, T) = c_0 + c_1(1-x)yz + c_2(1-y)zx + (1-z)xy(c_3x + c_4y) + c_5xyz, \quad (5.3)$$

where  $c_0$ ,  $c_1$ ,  $c_2$ ,  $c_3$ ,  $c_4$ , and  $c_5$  are parameters calculated by minimizing the total squared error. We calculated these fitting parameters for  $T = 300$  K, 473 K, 1000 K, and 1473 K using Nelder-Mead algorithm (NELDER; MEAD, 1965). The obtained coefficients and the fitting average error at each temperature are listed in Table 5.3. The maximal error for all considered chemical compositions and temperatures was 0.27 eV.

The dependence of the optical absorbance on the –O–/–OH ratio of a fully oxidized

TABLE 5.3 – Fitting parameters for gap bowing  $\Delta E_g(y, z, T)$  as defined in Eq.5.3 for different growth temperatures. The average fitting error  $\bar{e}$  is given for each temperature. Parameters for intermediate temperatures can be estimated by interpolation.

Temperature (K)	$c_0$	$c_1$	$c_2$	$c_3$	$c_4$	$c_5$	$\bar{e}$ (eV)
300	0.01	5.87	0.32	0.03	-4.52	16.60	0.09
473	0.04	5.76	0.18	-0.04	-2.31	9.44	0.04
1000	0.08	4.78	0.07	2.30	-2.36	0.11	0.07
1373	0.08	4.28	0.11	3.22	-3.54	-2.39	0.07

system is represented in Fig. 5.22. The spectra  $A_j(\omega)$  for all cluster classes have been computed and averaged using the probabilities  $x_j(y, z, T)$  in (2.77). One observes that temperature increase does not strongly influence optical absorption in the fully oxidized limit of GO systems with coadsorption of  $-\text{OH}$  and  $-\text{O}-$  groups. This insensitivity suggests that the statistics is dominated by the low energy configurations in a wide temperature range. One also observes that the first pronounced peak in optical absorbance for intermediate compositions  $y \approx z \approx 0.5$  of the two oxidant groups is blue shifted for very large photon energies, above 7 eV, which is consistent with the large energy gap anti-bowing observed in Fig. 5.21 for such compositions. The strength of the absorption decreases, however, monotonically from full decoration by epoxy groups to the hydroxyl decorated graphene.

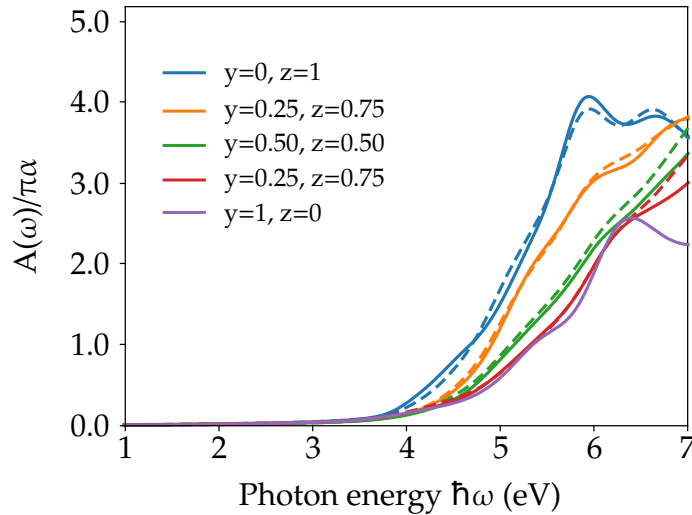


FIGURE 5.22 – The average optical absorbance of fully oxidized GO systems for different  $-\text{O}-/-\text{OH}$  ratio measured in units  $\pi\alpha$  ( $\alpha$  - fine structure constant), represented curves in different colors. The full lines represent the averages obtained within the GQCA statistical approach considering a growth temperature of  $200^\circ\text{C}$ , while the dashed lines have been computed for a growth temperature of  $1100^\circ\text{C}$ .

## 6 Conclusion

Using first-principles calculations combined with a generalized quasichemical approach we have studied the properties of different alloys,  $\text{Ge}_{1-x}\text{C}_x$ ,  $\text{Si}_{1-x}\text{Ge}_x$ ,  $\text{Si}_{1-x}\text{C}_x$  and  $(\text{BN})_{1-x}(\text{C}_2)_x$ . The standard GQCA approach was generalized to any system that can be modeled with a cluster expansion with a given chemical content, which enable us to study functionalized sheets, as graphene oxide under different growth conditions. We have described the properties of these materials as a function of their average compositions, and reported a big diversity of thermodynamic stability behaviors, which influence in their optical and electronic properties. Different features were observed in each case.

For  $\text{Si}_{1-x}\text{C}_x$  the contribution of cluster configuration ( $j = 11$ ), which corresponds to a planar, stoichiometric, graphene-like SiC geometry, as well as pure silicene and graphene are energetically favored. This fact induces an ordered phase for growth temperatures under 1000 K and has direct consequences on the possibilities of band gap engineering by composition and growth temperature control on this alloy.

For the germanium-containing alloys, the obtained  $T$ - $x$  diagrams show extremely different critical temperatures. They are related to the significantly different excess energies of the individual cluster configurations, which differ by about one order of magnitude between  $\text{Si}_{8-n_j}\text{Ge}_{n_j}$  and  $\text{Ge}_{8-n_j}\text{C}_{n_j}$  clusters. For  $\text{Ge}_{1-x}\text{C}_x$ , for which the majority of configurations have high excess energies, the preparation of the respective random alloys is not likely to be achievable beyond the very small solubility reported so far. A strong tendency for phase separation is expected to occur. For  $\text{Ge}_{1-x}\text{Si}_x$  the critical temperature approaches values of characteristic growth temperatures. Indeed, for higher temperatures random alloys should exist. For lower temperatures also the tendency to phase separation is visible. However, the two random alloys, which determine the decomposed  $\text{Ge}_{1-x}\text{Si}_x$  system, are not so close to the pure materials as in the case of  $\text{Ge}_{1-x}\text{C}_x$ .

For  $(\text{BN})_{1-x}(\text{C}_2)_x$ , we verified that this alloy system has a strong tendency to phase separation and that B-B and N-N bonds are energetically unfavored, resulting in a tendency for decomposition into a C-rich and a ( $h$ -BN)-rich phases, in agreement with experimental findings. Showing a different behavior when compared to the 3D alloys, for which the lattice mismatch is the main reason for the immiscibility. In this case, we have a chemical

reason.

The thermodynamic properties together with the ionicity of the bonds in the described alloys drastically influence the average fundamental energy gap versus composition. Whereas significant gaps appear for  $(\text{BN})_{1-x}(\text{C}_2)_x$  and  $\text{Si}_{1-x}\text{C}_x$  systems, they almost vanish for  $\text{Ge}_{1-x}\text{Si}_x$  and  $\text{Ge}_{1-x}\text{C}_x$ . Different aspects of these systems have been investigated and discussed, such as the effects of disorder induced by temperature growth on  $\text{Si}_{1-x}\text{C}_x$  electronic properties, or the consequences of phase segregation and composition fluctuation on  $(\text{BN})_{1-x}(\text{C}_2)_x$  optical properties. We developed a methodology to obtain the optical absorbance spectra considering the phase-separated alloys within the GQCA statistical approach. The absorption results with a double-peak show very good agreement with experimental findings.

The proposed extension of the GQCA approach to functionalized sheets was applied to graphene oxide. We demonstrated that the addition of oxidant groups can open large energy band gaps in this material. We investigated the oxidations processes with only hydroxyl and epoxy groups, corresponding to the wet and dry environments, and also the simultaneous adsorption of both groups in the carbon basal plane. The agglomeration of oxidant groups was demonstrated in terms of phase diagrams for both hydroxyl and epoxy groups. The agglomeration of oxidant groups occurs also for the simultaneous adsorption process, in which the interactions between  $-\text{OH}$  and  $-\text{O}-$  may lead to ordered structures with both groups and enhance the energy gap range to performing band gap engineering.

While most of literature neglect disorder effects of such 2D disordered systems, we extended and applied GQCA to this new class of materials. Relevant and innovative results were obtained and recently published in periodic journals as regular papers during the PhD project (GUILHON *et al.*, 2015; GUILHON *et al.*, 2017a; GUILHON *et al.*, 2017b). We showed the thermodynamic features have a determinant role in the determination of the electronic and optical properties of the considered 2D systems. Our results indicate that the use of a statistical approach to account for disorder effects is mandatory due the fact that atomic arrangement changes can result in entirely different electronic and optical properties. Moreover, our generalized approach is ready to be applied on other 2D disordered systems in future works.

# Bibliography

ADAMO, C.; BARONE, V. Toward reliable density functional methods without adjustable parameters: The PBE0 model. **The Journal of Chemical Physics**, v. 110, n. 13, p. 6158–6170, 1999. Disponível em: <<http://scitation.aip.org/content/aip/journal/jcp/110/13/10.1063/1.478522>>.

ADOLPH, B.; GAVRILENKO, V. I.; TENELSEN, K.; BECHSTEDT, F.; SOLE, R. D. Nonlocality and many-body effects in the optical properties of semiconductors. **Phys. Rev. B**, American Physical Society, v. 53, p. 9797–9808, Apr 1996. Disponível em: <<http://link.aps.org/doi/10.1103/PhysRevB.53.9797>>.

ALLEN, M. J. Honeycomb carbon: A review of graphene. **Science Direct**, v. 48, p. 2127–2150, 2010.

ARNAUD, B.; LEBÈGUE, S.; RABILLER, P.; ALOUANI, M. Huge excitonic effects in layered hexagonal boron nitride. **Phys. Rev. Lett.**, American Physical Society, v. 96, p. 026402, Jan 2006. Disponível em: <<http://link.aps.org/doi/10.1103/PhysRevLett.96.026402>>.

ASHCROFT, N. W.; MERMIN, N. D. **Solid State Physics**. [S.l.]: John Wiley Sons, 1960.

ATAIDE, C. A.; PELÁ, R. R.; MARQUES, M.; TELES, L. K.; FURTHMÜLLER, J.; BECHSTEDT, F. Fast and accurate approximate quasiparticle band structure calculations of zno, cdo, and mgo polymorphs. **Phys. Rev. B**, American Physical Society, v. 95, p. 045126, Jan 2017. Disponível em: <<https://link.aps.org/doi/10.1103/PhysRevB.95.045126>>.

AYARI, A.; COBAS, E.; OGUNDADEGBE, O.; FUHRER, M. S. Realization and electrical characterization of ultrathin crystals of layered transition-metal dichalcogenides. **Journal of Applied Physics**, v. 101, n. 1, p. –, 2007. Disponível em: <<http://scitation.aip.org/content/aip/journal/jap/101/1/10.1063/1.2407388>>.

AZEVEDO, S. Energetic stability of B-C-N monolayer. **Physics Letters A**, v. 351, n. 1-2, p. 109 – 112, 2006. ISSN 0375-9601. Disponível em: <<http://www.sciencedirect.com/science/article/pii/S0375960105016233>>.

BAMPOULIS, P.; ZHANG, L.; SAFAEI, A.; GASTEL, R. van; POELSEMA, B.; ZANDVLIET, H. J. W. Germanene termination of Ge<sub>2</sub>Pt crystals on Ge(110). **Journal of Physics: Condensed Matter**, v. 26, n. 44, p. 442001, 2014. Disponível em: <<http://stacks.iop.org/0953-8984/26/i=44/a=442001>>.

- BECHSTEDT, F. **Many-body approach to electronic excitations: concepts and applications**. [S.l.]: Springer, 2015.
- BECKE, A. D. Density-functional exchange-energy approximation with correct asymptotic behavior. **Phys. Rev. A**, American Physical Society, v. 38, p. 3098–3100, Sep 1988. Disponível em: <<http://link.aps.org/doi/10.1103/PhysRevA.38.3098>>.
- BECKE, A. D. A new mixing of hartree-fock and local density-functional theories. **The Journal of Chemical Physics**, v. 98, n. 2, p. 1372–1377, 1993. Disponível em: <<http://scitation.aip.org/content/aip/journal/jcp/98/2/10.1063/1.464304>>.
- BLOCHL, P. E. Projector augmented-wave method. **Phys. Rev. B**, American Physical Society, v. 50, p. 17953–17979, Dec 1994. Disponível em: <<http://link.aps.org/doi/10.1103/PhysRevB.50.17953>>.
- BRODIE, B. C. On the atomic weight of graphite. **Philosophical Transactions of the Royal Society of London**, The Royal Society, v. 149, p. 249–259, 1859. ISSN 02610523. Disponível em: <<http://www.jstor.org/stable/108699>>.
- CAHANGIROV, S.; TOPSAKAL, M.; AKTÜRK, E.; SAHIN, H.; CIRACI, S. Two- and one-dimensional honeycomb structures of silicon and germanium. **Phys. Rev. Lett.**, American Physical Society, v. 102, p. 236804, Jun 2009. Disponível em: <<http://link.aps.org/doi/10.1103/PhysRevLett.102.236804>>.
- CAI, W.; PINER, R. D.; STADERMANN, F. J.; PARK, S.; SHAIBAT, M. A.; ISHII, Y.; YANG, D.; VELAMAKANNI, A.; AN, S. J.; STOLLER, M.; AN, J.; CHEN, D.; RUOFF, R. S. Synthesis and solid-state nmr structural characterization of <sup>13</sup>C-labeled graphite oxide. **Science**, American Association for the Advancement of Science, v. 321, n. 5897, p. 1815–1817, 2008.
- CHANG, C.-K.; KATARIA, S.; KUO, C.-C.; GANGULY, A.; WANG, B.-Y.; HWANG, J.-Y.; HUANG, K.-J.; YANG, W.-H.; WANG, S.-B.; CHUANG, C.-H.; CHEN, M.; HUANG, C.-I.; PONG, W.-F.; SONG, K.-J.; CHANG, S.-J.; GUO, J.-H.; TAI, Y.; TSUJIMOTO, M.; ISODA, S.; CHEN, C.-W.; CHEN, L.-C.; CHEN, K.-H. Band gap engineering of chemical vapor deposited graphene by in situ BN doping. **ACS Nano**, v. 7, n. 2, p. 1333–1341, 2013. PMID: 23273110. Disponível em: <<http://dx.doi.org/10.1021/nn3049158>>.
- CHEN, A. B.; SHER, A. **Semiconductor Alloys**. New York: Plenum, 1995.
- CHEN, Y.; XI, J.; DUMCENCO, D. O.; LIU, Z.; SUENAGA, K.; WANG, D.; SHUAI, Z.; HUANG, Y.-S.; XIE, L. Tunable band gap photoluminescence from atomically thin transition-metal dichalcogenide alloys. **ACS Nano**, v. 7, n. 5, p. 4610–4616, 2013. PMID: 23600688. Disponível em: <<http://dx.doi.org/10.1021/nn401420h>>.
- CHIAPPE, D.; GRAZIANETTI, C.; TALLARIDA, G.; FANCIULLI, M.; MOLLE, A. Local electronic properties of corrugated silicene phases. **Advanced Materials**, WILEY-VCH Verlag, v. 24, n. 37, p. 5088–5093, 2012. ISSN 1521-4095. Disponível em: <<http://dx.doi.org/10.1002/adma.201202100>>.
- CI, L. Atomic layers of hybridized boron nitride and graphene domains. **Nature Material**, v. 9, n. 2711, p. 430–435, 2010.

- D'AVILA, M.; ROMA, F.; RICCARDO, J.; RAMIREZ-PASTOR, A. Quasi-chemical approximation for polyatomics: Statistical thermodynamics of adsorption. **Surface Science**, v. 600, n. 10, p. 2011 – 2025, 2006. ISSN 0039-6028. Disponível em: <<http://www.sciencedirect.com/science/article/pii/S0039602806002184>>.
- DAVILA, M. E.; XIAN, L.; CAHANGIROV, S.; RUBIO, A.; LAY, G. L. Germanene: a novel two-dimensional germanium allotrope akin to graphene and silicene. **New Journal of Physics**, v. 16, n. 9, p. 095002, 2014. Disponível em: <<http://stacks.iop.org/1367-2630/16/i=9/a=095002>>.
- DENTON, A. R.; ASHCROFT, N. W. Vegard's law. **Phys. Rev. A**, American Physical Society, v. 43, p. 3161–3164, Mar 1991. Disponível em: <<http://link.aps.org/doi/10.1103/PhysRevA.43.3161>>.
- DREYER, D. R.; PARK, S.; BIELAWSKI, C. W.; RUOFF, R. S. The chemistry of graphene oxide. **Chem. Soc. Rev.**, The Royal Society of Chemistry, v. 39, p. 228–240, 2010. Disponível em: <<http://dx.doi.org/10.1039/B917103G>>.
- D'SOUZA, R.; MUKHERJEE, S. Electronic structure, phase stability and resistivity of hybrid hexagonal two-dimensional nanomaterial: A first-principles study. **Physica E: Low-dimensional Systems and Nanostructures**, v. 69, n. 0, p. 138 – 144, 2015. ISSN 1386-9477. Disponível em: <<http://www.sciencedirect.com/science/article/pii/S1386947715000272>>.
- DUA, V.; SURWADE, S.; AMMU, S.; AGNIHOTRA, S.; JAIN, S.; ROBERTS, K.; PARK, S.; RUOFF, R.; MANOHAR, S. All-organic vapor sensor using inkjet-printed reduced graphene oxide. **Angewandte Chemie**, WILEY-VCH Verlag, v. 122, n. 12, p. 2200–2203, 2010. ISSN 1521-3757. Disponível em: <<http://dx.doi.org/10.1002/ange.200905089>>.
- DUAN, X.; WANG, C.; FAN, Z.; HAO, G.; KOU, L.; HALIM, U.; LI, H.; WU, X.; WANG, Y.; JIANG, J.; PAN, A.; HUANG, Y.; YU, R.; DUAN, X. Synthesis of ws<sub>2</sub>xse<sub>2</sub> alloy nanosheets with composition-tunable electronic properties. **Nano Letters**, v. 16, n. 1, p. 264–269, 2016. PMID: 26633760. Disponível em: <<http://dx.doi.org/10.1021/acs.nanolett.5b03662>>.
- DURIG, J. **Molecular Approach to Solids**. [S.l.]: Elsevier, 1998.
- EDA, G.; CHHOWALLA, M. Chemically derived graphene oxide: Towards large-area thin-film electronics and optoelectronics. **Advanced Materials**, WILEY-VCH Verlag, v. 22, n. 22, p. 2392–2415, 2010. ISSN 1521-4095. Disponível em: <<http://dx.doi.org/10.1002/adma.200903689>>.
- EHRENREICH, H.; COHEN, M. H. Self-consistent field approach to the many-electron problem. **Phys. Rev.**, American Physical Society, v. 115, p. 786–790, Aug 1959. Disponível em: <<http://link.aps.org/doi/10.1103/PhysRev.115.786>>.
- EIGLER, S.; HIRSCH, A. Chemistry with graphene and graphene oxide—challenges for synthetic chemists. **Angewandte Chemie International Edition**, WILEY-VCH Verlag, v. 53, n. 30, p. 7720–7738, 2014. ISSN 1521-3773. Disponível em: <<http://dx.doi.org/10.1002/anie.201402780>>.

- ELIAS, D. C.; NAIR, R. R.; MOHIUDDIN, T. M. G.; MOROZOV, S. V.; BLAKE, P.; HALSALL, M. P.; FERRARI, A. C.; BOUKHVALOV, D. W.; KATSNELSON, M. I.; GEIM, A. K.; NOVOSELOV, K. S. Control of graphene's properties by reversible hydrogenation: Evidence for graphane. **Science**, American Association for the Advancement of Science, v. 323, n. 5914, p. 610–613, 2009. ISSN 0036-8075. Disponível em: <<http://science.sciencemag.org/content/323/5914/610>>.
- FAZZIO, A. **Teoria quântica de moléculas e sólidos**. [S.l.]: Plenum Press, 1995.
- FENG, B.; DING, Z.; MENG, S.; YAO, Y.; HE, X.; CHENG, P.; CHEN, L.; WU, K. Evidence of silicene in honeycomb structures of silicon on Ag(111). **Nano Letters**, v. 12, n. 7, p. 3507–3511, 2012. PMID: 22658061. Disponível em: <<http://dx.doi.org/10.1021/nl301047g>>.
- FERREIRA, L. G.; MARQUES, M.; TELES, L. K. Approximation to density functional theory for the calculation of band gaps of semiconductors. **Phys. Rev. B**, American Physical Society, v. 78, p. 125116, Sep 2008. Disponível em: <<http://link.aps.org/doi/10.1103/PhysRevB.78.125116>>.
- FERREIRA, L. G.; MARQUES, M.; TELES, L. K. Slater half-occupation technique revisited: the LDA-1/2 and GGA-1/2 approaches for atomic ionization energies and band gaps in semiconductors. **AIP Advances**, v. 1, n. 3, 2011. Disponível em: <<http://scitation.aip.org/content/aip/journal/adva/1/3/10.1063/1.3624562>>.
- FLEURENCE, A.; FRIEDLEIN, R.; OZAKI, T.; KAWAI, H.; WANG, Y.; YAMADA-TAKAMURA, Y. Experimental evidence for epitaxial silicene on diboride thin films. **Phys. Rev. Lett.**, American Physical Society, v. 108, p. 245501, Jun 2012. Disponível em: <<http://link.aps.org/doi/10.1103/PhysRevLett.108.245501>>.
- FLYNN, G. W. Perspective: The dawning of the age of graphene. **The Journal of Chemical Physics**, v. 135, n. 5, 2011. Disponível em: <<http://scitation.aip.org/content/aip/journal/jcp/135/5/10.1063/1.3615063>>.
- GAJDOS, M.; HUMMER, K.; KRESSE, G.; FURTHMÜLLER, J.; BECHSTEDT, F. Linear optical properties in the projector-augmented wave methodology. **Phys. Rev. B**, American Physical Society, v. 73, p. 045112, Jan 2006. Disponível em: <<http://link.aps.org/doi/10.1103/PhysRevB.73.045112>>.
- GOKCEN, N. A. **Statistical Thermodynamics of Alloys**. [S.l.]: New York: Plenum Press, 1986.
- GOMEZ-NAVARRO, C.; WEITZ, R. T.; BITTNER, A. M.; SCOLARI, M.; MEWS, A.; BURGHARD, M.; KERN, K. Electronic transport properties of individual chemically reduced graphene oxide sheets. **Nano Letters**, v. 7, n. 11, p. 3499–3503, 2007. PMID: 17944526. Disponível em: <<http://dx.doi.org/10.1021/nl072090c>>.
- GONG, Y.; SHI, G.; ZHANG, Z.; ZHOU, W.; JUNG, J.; GAO, W.; MA, L.; YANG, Y.; YANG, S.; YOU, G.; VAJTAI, R.; XU, Q.; MACDONALD, A. H.; YAKOBSON, B. I.; LOU, J.; LIU, Z.; AJAYAN, P. M. Direct chemical conversion of graphene to boron- and nitrogen- and carbon-containing atomic layers. **Nat Commun**, Nature Publishing Group, a division of Macmillan Publishers Limited. All Rights Reserved., v. 5, 01 2014. Disponível em: <<http://dx.doi.org/10.1038/ncomms4193>>.

GORI, P.; PULCI, O.; MARSILI, M.; BECHSTEDT, F. Side-dependent electron escape from graphene- and graphane-like sic layers. **Applied Physics Letters**, v. 100, n. 4, p. –, 2012. Disponível em:

<<http://scitation.aip.org/content/aip/journal/apl/100/4/10.1063/1.3679175>>.

GUILHON, I.; KODA, D.; FERREIRA, L. G.; MARQUES, M.; TELES, L. K. Dft-1/2 quasiparticle corrections on band gap calculation of 2d materials: a comparison with hse06 and gw approaches. To be published.

GUILHON, I.; MARQUES, M.; TELES, L. K.; BECHSTEDT, F. Optical absorbance and band-gap engineering of  $(\text{BN})_{1-x}(\text{C}_2)_x$  two-dimensional alloys: Phase separation and composition fluctuation effects. **Phys. Rev. B**, American Physical Society, v. 95, p. 035407, Jan 2017. Disponível em:

<<http://link.aps.org/doi/10.1103/PhysRevB.95.035407>>.

GUILHON, I.; MARQUES, M.; TELES, L. K.; BECHSTEDT, F. Our first paper about graphene oxides. **Phys. Rev. B**, American Physical Society, v. 112344, p. 035407, Jan 2017. Disponível em: <<http://link.aps.org/doi/10.1103/PhysRevB.95.035407>>.

GUILHON, I.; TELES, L. K.; MARQUES, M.; PELA, R. R.; BECHSTEDT, F. Influence of structure and thermodynamic stability on electronic properties of two-dimensional SiC, SiGe, and GeC alloys. **Phys. Rev. B**, American Physical Society, v. 92, p. 075435, Aug 2015. Disponível em: <<http://link.aps.org/doi/10.1103/PhysRevB.92.075435>>.

HE, H.; KLINOWSKI, J.; FORSTER, M.; LERF, A. A new structural model for graphite oxide. **Chemical Physics Letters**, v. 287, n. 1, p. 53 – 56, 1998. ISSN 0009-2614. Disponível em: <<http://www.sciencedirect.com/science/article/pii/S0009261498001444>>.

HEYD, J.; SCUSERIA, G. E.; ERNZERHOF, M. Hybrid functionals based on a screened coulomb potential. **The Journal of Chemical Physics**, v. 118, n. 18, p. 8207–8215, 2003. Disponível em:

<<http://scitation.aip.org/content/aip/journal/jcp/118/18/10.1063/1.1564060>>.

HEYD, J.; SCUSERIA, G. E.; ERNZERHOF, M. Erratum:hybrid functionals based on a screened coulomb potential [J. Chem. Phys.118, 8207 (2003)]. **The Journal of Chemical Physics**, v. 124, n. 21, p. –, 2006. Disponível em:

<<http://scitation.aip.org/content/aip/journal/jcp/124/21/10.1063/1.2204597>>.

HOUSSA, M.; BROEK, B. van den; SCALISE, E.; EALET, B.; POURTOIS, G.; CHIAPPE, D.; CINQUANTA, E.; GRAZIANETTI, C.; FANCIULLI, M.; MOLLE, A.; AFANAS'EV, V.; STESMANS, A. Theoretical aspects of graphene-like group {IV} semiconductors. **Applied Surface Science**, v. 291, n. 0, p. 98 – 103, 2014. ISSN 0169-4332. E-MRS 2013 Spring Meeting , Symposium I: The route to post-Si {CMOS} devices: from high mobility channels to graphene-like 2D nanosheets. Disponível em: <<http://www.sciencedirect.com/science/article/pii/S0169433213017030>>.

HOUSSA, M.; POURTOIS, G.; HEYNS, M. M.; AFANASEV, V. V.; STESMANS, A. Electronic properties of silicene: Insights from first-principles modeling. **Journal of The Electrochemical Society**, v. 158, n. 2, p. H107–H110, 2011. Disponível em:

<<http://jes.ecsdl.org/content/158/2/H107.abstract>>.

HSUEH, H. C.; GUO, G. Y.; LOUIE, S. G. Excitonic effects in the optical properties of a sic sheet and nanotubes. **Phys. Rev. B**, American Physical Society, v. 84, p. 085404, Aug 2011. Disponível em: <<http://link.aps.org/doi/10.1103/PhysRevB.84.085404>>.

HUANG, Z.; CRESPI, V. H.; CHELIKOWSKY, J. R. Electronic properties of mixed-phase graphene/*h*-bn sheets using real-space pseudopotentials. **Phys. Rev. B**, American Physical Society, v. 88, p. 235425, Dec 2013. Disponível em: <<http://link.aps.org/doi/10.1103/PhysRevB.88.235425>>.

IVANOVSKII, A. L. Graphene-based and graphene-like materials. **Russian Chemical Reviews**, v. 81, n. 7, p. 571, 2012. Disponível em: <<http://stacks.iop.org/0036-021X/81/i=7/a=R01>>.

JAMDAGNI, P.; KUMAR, A.; THAKUR, A.; PANDEY, R.; AHLUWALIA, P. K. Stability and electronic properties of sige-based 2d layered structures. **Materials Research Express**, v. 2, n. 1, p. 016301, 2015. Disponível em: <<http://stacks.iop.org/2053-1591/2/i=1/a=016301>>.

JANAK, J. F. Proof that  $\frac{\partial e}{\partial n_i} = \epsilon$  in density-functional theory. **Phys. Rev. B**, American Physical Society, v. 18, p. 7165–7168, Dec 1978. Disponível em: <<http://link.aps.org/doi/10.1103/PhysRevB.18.7165>>.

JIANG, X.; NISAR, J.; PATHAK, B.; ZHAO, J.; AHUJA, R. Graphene oxide as a chemically tunable 2-d material for visible-light photocatalyst applications. **Journal of Catalysis**, v. 299, p. 204 – 209, 2013. ISSN 0021-9517. Disponível em: <<http://www.sciencedirect.com/science/article/pii/S0021951712004150>>.

JUNG, I.; FIELD, D. A.; CLARK, N. J.; ZHU, Y.; YANG, D.; PINER, R. D.; STANKOVICH, S.; DIKIN, D. A.; GEISLER, H.; VENTRICE, C. A.; RUOFF, R. S. Reduction kinetics of graphene oxide determined by electrical transport measurements and temperature programmed desorption. **The Journal of Physical Chemistry C**, v. 113, n. 43, p. 18480–18486, 2009. Disponível em: <<http://dx.doi.org/10.1021/jp904396j>>.

KAN, M.; ZHOU, J.; WANG, Q.; SUN, Q.; JENA, P. Tuning the band gap and magnetic properties of bn sheets impregnated with graphene flakes. **Phys. Rev. B**, American Physical Society, v. 84, p. 205412, Nov 2011. Disponível em: <<http://link.aps.org/doi/10.1103/PhysRevB.84.205412>>.

KIM, M. C.; HWANG, G. S.; RUOFF, R. S. Epoxide reduction with hydrazine on graphene: A first principles study. **The Journal of Chemical Physics**, v. 131, n. 6, p. 064704, 2009. Disponível em: <<http://aip.scitation.org/doi/abs/10.1063/1.3197007>>.

KOHN, W. Self-consistent equations including exchange and correlation effects. **Physical Review**, v. 140, p. A1133, 1965.

KOKOTT, S.; PFLUGRADT, P.; MATTHES, L.; BECHSTEDT, F. Nonmetallic substrates for growth of silicene: an ab initio prediction. **Journal of Physics: Condensed Matter**, v. 26, n. 18, p. 185002, 2014. Disponível em: <<http://stacks.iop.org/0953-8984/26/i=18/a=185002>>.

KOSKI, K. J.; CUI, Y. The new skinny in two-dimensional nanomaterials. **ACS Nano**, v. 7, n. 5, p. 3739–3743, 2013. PMID: 23678956. Disponível em: <<http://dx.doi.org/10.1021/nn4022422>>.

KRESSE, G. From ultrasoft pseudopotentials to the projector augmented-wave method. **Phys. Rev. B**, v. 59, p. 1758, 1999.

KRESSE, G. **VASP the GUIDE**. [S.l.]: Universitat Wien, 2012.

KRISHNAMOORTHY, K.; VEERAPANDIAN, M.; MOHAN, R.; KIM, S.-J. Investigation of raman and photoluminescence studies of reduced graphene oxide sheets. **Applied Physics A**, v. 106, n. 3, p. 501–506, 2012. ISSN 1432-0630. Disponível em: <<http://dx.doi.org/10.1007/s00339-011-6720-6>>.

KULLBACK, S.; LEIBLER, R. A. On information and sufficiency. **Ann. Math. Statist.**, The Institute of Mathematical Statistics, v. 22, n. 1, p. 79–86, 03 1951. Disponível em: <<http://dx.doi.org/10.1214/aoms/1177729694>>.

LEE, C.; YANG, W.; PARR, R. G. Development of the Colle-Salvetti correlation-energy formula into a functional of the electron density. **Phys. Rev. B**, American Physical Society, v. 37, p. 785–789, Jan 1988. Disponível em: <<http://link.aps.org/doi/10.1103/PhysRevB.37.785>>.

LEITE, J. R.; FERREIRA, L. G. Effects of the Coulomb correlation on the calculated results for atoms with and without spin polarization. **Phys. Rev. A**, American Physical Society, v. 3, p. 1224–1230, Apr 1971. Disponível em: <<http://link.aps.org/doi/10.1103/PhysRevA.3.1224>>.

LERF, A.; HE, H.; FORSTER, M.; KLINOWSKI, J. Structure of graphite oxide revisited. **The Journal of Physical Chemistry B**, v. 102, n. 23, p. 4477–4482, 1998. Disponível em: <<http://dx.doi.org/10.1021/jp9731821>>.

LI, B.; HUANG, L.; ZHONG, M.; HUO, N.; LI, Y.; YANG, S.; FAN, C.; YANG, J.; HU, W.; WEI, Z.; LI, J. Synthesis and transport properties of large-scale alloy Co<sub>0.16</sub>Mo<sub>0.84</sub>S<sub>2</sub> bilayer nanosheets. **ACS Nano**, v. 9, n. 2, p. 1257–1262, 2015. PMID: 25584859. Disponível em: <<http://dx.doi.org/10.1021/nm505048y>>.

LI, H.; DUAN, X.; WU, X.; ZHUANG, X.; ZHOU, H.; ZHANG, Q.; ZHU, X.; HU, W.; REN, P.; GUO, P.; MA, L.; FAN, X.; WANG, X.; XU, J.; PAN, A.; DUAN, X. Growth of alloy MoS<sub>2</sub>xSe<sub>2</sub>(1-x) nanosheets with fully tunable chemical compositions and optical properties. **Journal of the American Chemical Society**, v. 136, n. 10, p. 3756–3759, 2014. PMID: 24564365. Disponível em: <<http://dx.doi.org/10.1021/ja500069b>>.

LI, L.; LU, S.; PAN, J.; QIN, Z.; WANG, Y.; WANG, Y.; CAO, G.; DU, S.; GAO, H.-J. Buckled germanene formation on Pt(111). **Advanced Materials**, v. 26, n. 28, p. 4820–4824, 2014. ISSN 1521-4095. Disponível em: <<http://dx.doi.org/10.1002/adma.201400909>>.

LIAO, L.; PENG, H.; LIU, Z. Chemistry makes graphene beyond graphene. **Journal of the American Chemical Society**, v. 136, n. 35, p. 12194–12200, 2014. PMID: 25126670. Disponível em: <<http://dx.doi.org/10.1021/ja5048297>>.

LIN, S. S. Light-emitting two-dimensional ultrathin silicon carbide. **The Journal of Physical Chemistry C**, v. 116, n. 6, p. 3951–3955, 2012. Disponível em: <<http://dx.doi.org/10.1021/jp210536m>>.

LIN, X.; LIN, S.; XU, Y.; HAKRO, A. A.; HASAN, T.; ZHANG, B.; YU, B.; LUO, J.; LI, E.; CHEN, H. Ab initio study of electronic and optical behavior of two-dimensional silicon carbide. **J. Mater. Chem. C**, The Royal Society of Chemistry, v. 1, p. 2131–2135, 2013. Disponível em: <<http://dx.doi.org/10.1039/C3TC00629H>>.

LIU, Z. In-plane heterostructures of graphene and hexagonal boron nitride with controlled domain sizes. **Nature Nanotechnology**, v. 8, p. 119–124, 2013. ISSN 1748-3387. Disponível em: <<http://dx.doi.org/10.1038/nnano.2012.256>>.

LOGINOVA, E.; BARTELT, N. C.; FEIBELMAN, P. J.; MCCARTY, K. F. Evidence for graphene growth by C cluster attachment. **New Journal of Physics**, v. 10, n. 9, p. 093026, 2008. Disponível em: <<http://stacks.iop.org/1367-2630/10/i=9/a=093026>>.

LOH, K. P.; BAO, Q.; EDA, G.; CHHOWALLA, M. Graphene oxide as a chemically tunable platform for optical applications. **Nature Chemistry**, v. 2, n. 12, p. 1015–1024, 2010.

LU, N.; YIN, D.; LI, Z.; YANG, J. Structure of graphene oxide: Thermodynamics versus kinetics. **The Journal of Physical Chemistry C**, v. 115, n. 24, p. 11991–11995, 2011. Disponível em: <<http://dx.doi.org/10.1021/jp204476q>>.

LU, T.-Y.; LIAO, X.-X.; WANG, H.-Q.; ZHENG, J.-C. Tuning the indirect-direct band gap transition of sic, gec and snc monolayer in a graphene-like honeycomb structure by strain engineering: a quasiparticle gw study. **J. Mater. Chem.**, The Royal Society of Chemistry, v. 22, p. 10062–10068, 2012. Disponível em: <<http://dx.doi.org/10.1039/C2JM30915G>>.

MAK, K. F.; SFEIR, M. Y.; WU, Y.; LUI, C. H.; MISEWICH, J. A.; HEINZ, T. F. Measurement of the optical conductivity of graphene. **Phys. Rev. Lett.**, American Physical Society, v. 101, p. 196405, Nov 2008. Disponível em: <<http://link.aps.org/doi/10.1103/PhysRevLett.101.196405>>.

MAO, S.; PU, H.; CHEN, J. Graphene oxide and its reduction: modeling and experimental progress. **RSC Adv.**, The Royal Society of Chemistry, v. 2, p. 2643–2662, 2012. Disponível em: <<http://dx.doi.org/10.1039/C2RA00663D>>.

MARCANO, D. C.; KOSYNKIN, D. V.; BERLIN, J. M.; SINITSKII, A.; SUN, Z.; SLESAREV, A.; ALEMANY, L. B.; LU, W.; TOUR, J. M. Improved synthesis of graphene oxide. **ACS Nano**, v. 4, n. 8, p. 4806–4814, 2010. PMID: 20731455. Disponível em: <<http://dx.doi.org/10.1021/nm1006368>>.

MARDER, M. P. **Condensed Matter Physics**. [S.l.]: Harcourt College Publishers, 1976.

MARQUES, M.; TELES, L. K.; FERREIRA, L. G.; SCOLFARO, L. M. R.; FURTHMULLER, J.; BECHSTEDT, F. Statistical model applied to  $a_x b_y c_{1-x-y} D$  quaternary alloys: Bond lengths and energy gaps of  $a_x g_a y_{in_{1-x-y}} X$  ( $X = As, p, \text{ or } n$ ) systems. **Phys. Rev. B**, American Physical Society, v. 73, p. 235205, Jun 2006. Disponível em: <<http://link.aps.org/doi/10.1103/PhysRevB.73.235205>>.

MARQUES, M.; TELES, L. K.; SCOLFARO, L. M. R.; LEITE, J. R.; FURTHMULLER, J.; BECHSTEDT, F. Lattice parameter and energy band gap of cubic  $Al_x Ga_y In_{1-x-y} N$  quaternary alloys. **Appl. Phys. Lett.**, v. 83, p. 890, 2003.

MARTIN, R. Ground state of the electron gas by a stochastic method. **Phys. Rev. Lett.**, v. 45, p. 566, 1980.

MATTHES, L.; GORI, P.; PULCI, O.; BECHSTEDT, F. Universal infrared absorbance of two-dimensional honeycomb group-IV crystals. **Phys. Rev. B**, American Physical Society, v. 87, p. 035438, Jan 2013. Disponível em: <<http://link.aps.org/doi/10.1103/PhysRevB.87.035438>>.

MATTHES, L.; PULCI, O.; BECHSTEDT, F. Massive Dirac quasiparticles in the optical absorbance of graphene, silicene, germanene, and tinene. **Journal of Physics: Condensed Matter**, v. 25, n. 39, p. 395305, 2013. Disponível em: <<http://stacks.iop.org/0953-8984/25/i=39/a=395305>>.

MATTHES, L.; PULCI, O.; BECHSTEDT, F. Optical properties of two-dimensional honeycomb crystals graphene, silicene, germanene, and tinene from first principles. **New Journal of Physics**, v. 16, n. 10, p. 105007, 2014. Disponível em: <<http://stacks.iop.org/1367-2630/16/i=10/a=105007>>.

MATUSALEM, F.; MARQUES, M.; TELES, L. K.; BECHSTEDT, F. Stability and electronic structure of two-dimensional allotropes of group-iv materials. **Phys. Rev. B**, American Physical Society, v. 92, p. 045436, Jul 2015. Disponível em: <<https://link.aps.org/doi/10.1103/PhysRevB.92.045436>>.

MAZZONI, M. S. C.; NUNES, R. W.; AZEVEDO, S.; CHACHAM, H. Electronic structure and energetics of  $B_xC_yN_z$  layered structures. **Phys. Rev. B**, American Physical Society, v. 73, p. 073108, Feb 2006. Disponível em: <<http://link.aps.org/doi/10.1103/PhysRevB.73.073108>>.

MENG, L.; WANG, Y.; ZHANG, L.; DU, S.; WU, R.; LI, L.; ZHANG, Y.; LI, G.; ZHOU, H.; HOFER, W. A.; GAO, H.-J. Buckled silicene formation on Ir(111). **Nano Letters**, v. 13, n. 2, p. 685–690, 2013. PMID: 23330602. Disponível em: <<http://dx.doi.org/10.1021/nl304347w>>.

MIRO, P.; AUDIFFRED, M.; HEINE, T. An atlas of two-dimensional materials. **Chem. Soc. Rev.**, The Royal Society of Chemistry, v. 43, p. 6537–6554, 2014. Disponível em: <<http://dx.doi.org/10.1039/C4CS00102H>>.

MÖNCH, W. **Semiconductor Surfaces and Interfaces**. [S.l.]: Springer Berlin Heidelberg, 1993.

NAIR, R. R.; BLAKE, P.; GRIGORENKO, A. N.; NOVOSELOV, K. S.; BOOTH, T. J.; STAUBER, T.; PERES, N. M. R.; GEIM, A. K. Fine structure constant defines visual transparency of graphene. **Science**, American Association for the Advancement of Science, v. 320, n. 5881, p. 1308–1308, 2008. ISSN 0036-8075. Disponível em: <<http://science.sciencemag.org/content/320/5881/1308>>.

NELDER, J. A.; MEAD, R. A simplex method for function minimization. **The Computer Journal**, v. 7, n. 4, p. 308–313, 1965. Disponível em: <<http://comjnl.oxfordjournals.org/content/7/4/308.abstract>>.

NI, M.; WANG, Y.; YANG, Q.; ZHU, W.; TANG, Q.; LI, Z. Stability and electronic properties of hexagonal boron nitride monolayer with irregular graphene domains embedded. **Modern Physics Letters B**, v. 28, n. 18, p. 1450144, 2014. Disponível em: <<http://www.worldscientific.com/doi/abs/10.1142/S0217984914501449>>.

NOBEL. **Press Release: The 1998 Nobel Prize in Chemistry**. [S.l.: s.n.], 1998.

NOURBAKHS, A.; CANTORO, M.; VOSCH, T.; POURTOIS, G.; CLEMENTE, F.; VEEN, M. H. van der; HOFKENS, J.; HEYNS, M. M.; GENDT, S. D.; SELS, B. F. Bandgap opening in oxygen plasma-treated graphene. **Nanotechnology**, v. 21, n. 43, p. 435203, 2010. Disponível em: <<http://stacks.iop.org/0957-4484/21/i=43/a=435203>>.

NOVOSELOV, K. Electric field effect in atomically thin carbon films. **Science**, p. 501686, 2004.

NOVOSELOV, K. S.; FAL'KO, V. I.; COLOMBO, L.; GELLERT, P. R.; SCHWAB, M. G.; KIM, K. A roadmap for graphene. **Nature**, Nature Publishing Group, a division of Macmillan Publishers Limited. All Rights Reserved., v. 490, n. 7419, p. 192–200, 10 2012. Disponível em: <<http://dx.doi.org/10.1038/nature11458>>.

PACILE, D.; MEYER, J. C.; GIRIT Ç. O.; ZETTL, A. The two-dimensional phase of boron nitride: Few-atomic-layer sheets and suspended membranes. **Appl. Phys. Lett.**, v. 92, n. 13, p. –, 2008. Disponível em: <<http://scitation.aip.org/content/aip/journal/apl/92/13/10.1063/1.2903702>>.

PADILHA, J. E.; SEIXAS, L.; PONTES, R. B.; SILVA, A. J. R. da; FAZZIO, A. Quantum spin Hall effect in a disordered hexagonal SixGe1-x alloy. **Phys. Rev. B**, v. 88, p. 201106, 2013.

PARR, R. G. **Density-Functional Theory of Atoms and Molecules**. [S.l.]: Oxford University Press, 1989.

PEI, S.; CHENG, H.-M. The reduction of graphene oxide. **Carbon**, v. 50, n. 9, p. 3210 – 3228, 2012. ISSN 0008-6223. Festschrift dedicated to Peter A. Throer, Editor-in-Chief, 1972 - 2012. Disponível em: <<http://www.sciencedirect.com/science/article/pii/S0008622311008967>>.

PELA, R.; CAETANO, C.; MARQUES, M.; FERREIRA, L. G.; FURTHMÜLLER, J.; TELES, L. K. Accurate band gaps of AlGa<sub>N</sub>, InGa<sub>N</sub>, and AlIn<sub>N</sub> alloys calculations based on LDA-1/2 approach. **Applied Physics Letters**, v. 98, n. 15, p. –, 2011. Disponível em: <<http://scitation.aip.org/content/aip/journal/apl/98/15/10.1063/1.3576570>>.

PELA, R. R.; MARQUES, M.; TELES, L. K. Comparing LDA-1/2, HSE03, HSE06 and G0W0 approaches for band gap calculations of alloys. **Journal of Physics: Condensed Matter**, v. 27, n. 50, p. 505502, 2015. Disponível em: <<http://stacks.iop.org/0953-8984/27/i=50/a=505502>>.

PENG, X.; TANG, F.; COPPLE, A. Engineering the work function of armchair graphene nanoribbons using strain and functional species: a first principles study. **Journal of Physics: Condensed Matter**, v. 24, n. 7, p. 075501, 2012. Disponível em: <<http://stacks.iop.org/0953-8984/24/i=7/a=075501>>.

- PERDEW, J. P.; ERNZERHOF, M.; BURKE, K. Rationale for mixing exact exchange with density functional approximations. **The Journal of Chemical Physics**, v. 105, n. 22, p. 9982–9985, 1996. Disponível em: <<http://scitation.aip.org/content/aip/journal/jcp/105/22/10.1063/1.472933>>.
- PERDEW, J. P.; YUE, W. Accurate and simple density functional for the electronic exchange energy: Generalized gradient approximation. **Phys. Rev. B**, American Physical Society, v. 33, p. 8800–8802, Jun 1986. Disponível em: <<http://link.aps.org/doi/10.1103/PhysRevB.33.8800>>.
- PIZA, A. F. R. de T. **Mecânica Quântica**. [S.l.]: EDUSP, 2003.
- POH, H. L.; SIMEK, P.; SOFER, Z.; PUMERA, M. Halogenation of graphene with chlorine, bromine, or iodine by exfoliation in a halogen atmosphere. **Chemistry & A European Journal**, WILEY-VCH Verlag, v. 19, n. 8, p. 2655–2662, 2013. ISSN 1521-3765. Disponível em: <<http://dx.doi.org/10.1002/chem.201202972>>.
- PORTER, D. A.; EASTERLING, K. E. **Phase Transformations in Metals and Alloys**. UK: Van Nostrand Reinhold, 1981.
- PULCI, O.; GORI, P.; MARSILI, M.; GARBUIO, V.; SOLE, R. D.; BECHSTEDT, F. Strong excitons in novel two-dimensional crystals: Silicene and germanene. **EPL (Europhysics Letters)**, IOP Publishing, v. 98, n. 3, p. 37004, 2012.
- PUMERA, M.; WONG, C. H. A. Graphene and hydrogenated graphene. **Chem. Soc. Rev.**, The Royal Society of Chemistry, v. 42, p. 5987–5995, 2013. Disponível em: <<http://dx.doi.org/10.1039/C3CS60132C>>.
- RAIDONGIA, K.; NAG, A.; HEMBRAM, K.; WAGHMARE, U.; DATTA, R.; RAO, C. Bcn: A graphene analogue with remarkable adsorptive properties. **Chemistry - A European Journal**, WILEY-VCH Verlag, v. 16, n. 1, p. 149–157, 2010. ISSN 1521-3765. Disponível em: <<http://dx.doi.org/10.1002/chem.200902478>>.
- REINA, A. Large area, few-layer graphene films on arbitrary substrates by chemical vapor deposition. **J. Nano Letters**, v. 9, p. 30, 2009.
- RIGOSI, A. F.; HILL, H. M.; RIM, K. T.; FLYNN, G. W.; HEINZ, T. F. Electronic band gaps and exciton binding energies in monolayer  $\text{Mo}_x\text{W}_{1-x}\text{S}_2$  transition metal dichalcogenide alloys probed by scanning tunneling and optical spectroscopy. **Phys. Rev. B**, American Physical Society, v. 94, p. 075440, Aug 2016. Disponível em: <<https://link.aps.org/doi/10.1103/PhysRevB.94.075440>>.
- ROBINSON, J. T.; PERKINS, F. K.; SNOW, E. S.; WEI, Z.; SHEEHAN, P. E. Reduced graphene oxide molecular sensors. **Nano Letters**, v. 8, n. 10, p. 3137–3140, 2008. PMID: 18763832. Disponível em: <<http://dx.doi.org/10.1021/nl8013007>>.
- ROLDAN, R.; SILVA-GUILLEN, J. A.; LOPEZ-SANCHO, M. P.; GUINEA, F.; CAPPELLUTI, E.; ORDEJON, P. Electronic properties of single-layer and multilayer transition metal dichalcogenides  $\text{MX}_2$  ( $\text{M} = \text{Mo}, \text{W}$  and  $\text{X} = \text{S}, \text{Se}$ ). **Annalen der Physik**, v. 526, n. 9-10, p. 347–357, 2014. ISSN 1521-3889. Disponível em: <<http://dx.doi.org/10.1002/andp.201400128>>.

- ROMA, F.; RAMIREZ-PASTOR, A. J.; RICCARDO, J. L. Multisite occupancy adsorption: A comparative study of new different analytical approaches. **Langmuir**, v. 19, n. 17, p. 6770–6777, 2003. Disponível em: <<http://dx.doi.org/10.1021/la0209785>>.
- SAHIN, H.; CAHANGIROV, S.; TOPSAKAL, M.; BEKAROGLU, E.; AKTURK, E.; SENGER, R. T.; CIRACI, S. Monolayer honeycomb structures of group-IV elements and III-V binary compounds: First-principles calculations. **Phys. Rev. B**, v. 80, p. 155453, 2009.
- SALINAS, S. R. A. **Introducao a Fisica Estatistica**. BR: EDUSP, 1997.
- SHER, A.-B. C. e A. **Semiconductor Alloys**. [S.l.]: Plenum Press, 1995.
- SLATER, J. C.; JOHNSON, K. H. Self-consistent-field  $x\alpha$  cluster method for polyatomic molecules and solids. **Phys. Rev. B**, American Physical Society, v. 5, p. 844–853, Feb 1972. Disponível em: <<https://link.aps.org/doi/10.1103/PhysRevB.5.844>>.
- SOFO, J. O.; CHAUDHARI, A. S.; BARBER, G. D. Graphane: A two-dimensional hydrocarbon. **Phys. Rev. B**, American Physical Society, v. 75, p. 153401, Apr 2007. Disponível em: <<https://link.aps.org/doi/10.1103/PhysRevB.75.153401>>.
- SONE, J.; YAMAGAMI, T.; AOKI, Y.; NAKATSUJI, K.; HIRAYAMA, H. Epitaxial growth of silicene on ultra-thin Ag(111) films. **New Journal of Physics**, v. 16, n. 9, p. 095004, 2014. Disponível em: <<http://stacks.iop.org/1367-2630/16/i=9/a=095004>>.
- STEPHENS, P. J.; DEVLIN, F. J.; ASHVAR, C. S.; BAK, K. L.; TAYLOR, P. R.; FRISCH, M. J. Comparison of local, nonlocal, and hybrid density functionals using vibrational absorption and circular dichroism spectroscopy. In: \_\_\_\_\_. [s.n.], 1996. cap. 7, p. 105–113. Disponível em: <<http://pubs.acs.org/doi/abs/10.1021/bk-1996-0629.ch007>>.
- SUTTER, P. W. Epitaxial graphene on ruthenium. **Nature Materials**, v. 7, p. 406, 2008.
- SUZUKI, T. Theoretical discovery of stable structures of group III-V monolayers: The materials for semiconductor devices. **Applied Physics Letters**, v. 107, n. 21, 2015. Disponível em: <<http://scitation.aip.org/content/aip/journal/apl/107/21/10.1063/1.4936553>>.
- SUZUKI, T.; YOKOMIZO, Y. Energy bands of atomic monolayers of various materials: Possibility of energy gap engineering. **Physica E: Low-dimensional Systems and Nanostructures**, v. 42, n. 10, p. 2820 – 2825, 2010. ISSN 1386-9477. 14th International Conference on Modulated Semiconductor Structures. Disponível em: <<http://www.sciencedirect.com/science/article/pii/S1386947710002729>>.
- TELES, L. K.; FURTHMÜLLER, J.; SCOLFARO, L. M. R.; LEITE, J. R.; BECHSTEDT, F. First-principles calculations of the thermodynamic and structural properties of strained  $\text{In}_x\text{Ga}_{1-x}\text{N}$  and  $\text{Al}_x\text{Ga}_{1-x}\text{N}$  alloys. **Phys. Rev. B**, American Physical Society, v. 62, p. 2475–2485, Jul 2000. Disponível em: <<http://link.aps.org/doi/10.1103/PhysRevB.62.2475>>.
- TELES, L. K.; FURTHMÜLLER, J.; SCOLFARO, L. M. R.; LEITE, J. R.; BECHSTEDT, F. Influence of composition fluctuations and strain on gap bowing in

$\text{In}_x\text{Ga}_{1-x}\text{N}$ . **Phys. Rev. B**, American Physical Society, v. 63, p. 085204, Feb 2001. Disponível em: <<http://link.aps.org/doi/10.1103/PhysRevB.63.085204>>.

TELES, L. K.; SCOLFARO, L. M. R.; LEITE, J. R.; FURTHMÜLLER, J.; BECHSTEDT, F. Phase diagram, chemical bonds, and gap bowing of cubic  $\text{In}_x\text{Al}_{1-x}\text{N}$  alloys: Ab-initio calculations. **Journal of Applied Physics**, v. 92, n. 12, p. 7109–7113, 2002. Disponível em: <<http://scitation.aip.org/content/aip/journal/jap/92/12/10.1063/1.1518136>>.

UDDIN, M. R.; LI, J.; LIN, J. Y.; JIANG, H. X. Carbon-rich hexagonal (BN)C alloys. **Journal of Applied Physics**, v. 117, n. 21, p. –, 2015. Disponível em: <<http://scitation.aip.org/content/aip/journal/jap/117/21/10.1063/1.4921931>>.

UDDIN, M. R.; MAJETY, S.; LI, J.; LIN, J. Y.; JIANG, H. X. Layer-structured hexagonal (BN)C semiconductor alloys with tunable optical and electrical properties. **Journal of Applied Physics**, v. 115, n. 9, p. –, 2014. Disponível em: <<http://scitation.aip.org/content/aip/journal/jap/115/9/10.1063/1.4867641>>.

VEGARD, L. Die konstitution der mischkristalle und die raumfüllung der atome. **Zeitschrift für Physik**, v. 5, n. 1, p. 17–26, 1921. ISSN 0044-3328. Disponível em: <<http://dx.doi.org/10.1007/BF01349680>>.

VOGT, P.; PADOVA, P. D.; QUARESIMA, C.; AVILA, J.; FRANTZESKAKIS, E.; ASENSIO, M. C.; RESTA, A.; EALET, B.; LAY, G. L. Silicene: Compelling experimental evidence for graphenelike two-dimensional silicon. **Phys. Rev. Lett.**, American Physical Society, v. 108, p. 155501, Apr 2012. Disponível em: <<http://link.aps.org/doi/10.1103/PhysRevLett.108.155501>>.

WANG, L.; SUN, Y. Y.; LEE, K.; WEST, D.; CHEN, Z. F.; ZHAO, J. J.; ZHANG, S. B. Stability of graphene oxide phases from first-principles calculations. **Phys. Rev. B**, American Physical Society, v. 82, p. 161406, Oct 2010. Disponível em: <<http://link.aps.org/doi/10.1103/PhysRevB.82.161406>>.

WANG, M.; HUANG, W.; CHAN-PARK, M. B.; LI, C. M. Magnetism in oxidized graphenes with hydroxyl groups. **Nanotechnology**, v. 22, n. 10, p. 105702, 2011. Disponível em: <<http://stacks.iop.org/0957-4484/22/i=10/a=105702>>.

WATANABE, M. O.; ITOH, S.; SASAKI, T.; MIZUSHIMA, K. Visible-Light-Emitting Layered  $\text{BC}_2\text{N}$  Semiconductor. **Phys. Rev. Lett.**, American Physical Society, v. 77, p. 187–189, Jul 1996. Disponível em: <<http://link.aps.org/doi/10.1103/PhysRevLett.77.187>>.

WATANABE, T. T. K.; KANDA, H. Direct-bandgap properties and evidence for ultraviolet lasing of hexagonal boron nitride single crystal. **Nature Materials**, v. 3, p. 404–409, 2004. ISSN 1476-1122. Disponível em: <<http://dx.doi.org/10.1038/nmat1134>>.

WATARI, A. F. e K. **Introdução à Teoria de Grupos aplicada em moléculas e sólidos**. [S.l.]: Editora UFSM, 2009.

WEI, X.-L.; ZHANG, H.; GUO, G.-C.; LI, X.-B.; LAU, W.-M.; LIU, L.-M. Modulating the atomic and electronic structures through alloying and heterostructure of single-layer  $\text{MoS}_2$ . **J. Mater. Chem. A**, The Royal Society of Chemistry, v. 2, p. 2101–2109, 2014. Disponível em: <<http://dx.doi.org/10.1039/C3TA13659K>>.

- WEI, Z.; WANG, D.; KIM, S.; KIM, S.-Y.; HU, Y.; YAKES, M. K.; LARACUENTE, A. R.; DAI, Z.; MARDER, S. R.; BERGER, C.; KING, W. P.; HEER, W. A. de; SHEEHAN, P. E.; RIEDO, E. Nanoscale tunable reduction of graphene oxide for graphene electronics. **Science**, v. 328, n. 5984, p. 1373–1376, 2010. Disponível em: <<http://science.sciencemag.org/content/328/5984/1373>>.
- WIRTZ, L.; MARINI, A.; RUBIO, A. Excitons in boron nitride nanotubes: Dimensionality effects. **Phys. Rev. Lett.**, American Physical Society, v. 96, p. 126104, Mar 2006. Disponível em: <<https://link.aps.org/doi/10.1103/PhysRevLett.96.126104>>.
- WU, X.; SPRINKLE, M.; LI, X.; MING, F.; BERGER, C.; HEER, W. A. de. Epitaxial-graphene/graphene-oxide junction: An essential step towards epitaxial graphene electronics. **Phys. Rev. Lett.**, American Physical Society, v. 101, p. 026801, Jul 2008. Disponível em: <<http://link.aps.org/doi/10.1103/PhysRevLett.101.026801>>.
- XU, M.; LIANG, T.; SHI, M.; CHEN, H. Graphene-like two-dimensional materials. **Chemical Reviews**, v. 113, n. 5, p. 3766–3798, 2013. PMID: 23286380. Disponível em: <<http://dx.doi.org/10.1021/cr300263a>>.
- YAN, J.-A.; CHOU, M. Y. Oxidation functional groups on graphene: Structural and electronic properties. **Phys. Rev. B**, American Physical Society, v. 82, p. 125403, Sep 2010. Disponível em: <<https://link.aps.org/doi/10.1103/PhysRevB.82.125403>>.
- YAN, J.-A.; XIAN, L.; CHOU, M. Y. Structural and electronic properties of oxidized graphene. **Phys. Rev. Lett.**, American Physical Society, v. 103, p. 086802, Aug 2009. Disponível em: <<http://link.aps.org/doi/10.1103/PhysRevLett.103.086802>>.
- YANG, L.; DESLIPPE, J.; PARK, C.-H.; COHEN, M. L.; LOUIE, S. G. Excitonic effects on the optical response of graphene and bilayer graphene. **Phys. Rev. Lett.**, American Physical Society, v. 103, p. 186802, Oct 2009. Disponível em: <<https://link.aps.org/doi/10.1103/PhysRevLett.103.186802>>.
- YEH, T.-F.; CHAN, F.-F.; HSIEH, C.-T.; TENG, H. Graphite oxide with different oxygenated levels for hydrogen and oxygen production from water under illumination: The band positions of graphite oxide. **The Journal of Physical Chemistry C**, v. 115, n. 45, p. 22587–22597, 2011. Disponível em: <<http://dx.doi.org/10.1021/jp204856c>>.
- YEH, T.-F.; SYU, J.-M.; CHENG, C.; CHANG, T.-H.; TENG, H. Graphite oxide as a photocatalyst for hydrogen production from water. **Advanced Functional Materials**, WILEY-VCH Verlag, v. 20, n. 14, p. 2255–2262, 2010. ISSN 1616-3028. Disponível em: <<http://dx.doi.org/10.1002/adfm.201000274>>.
- YI, M.; SHEN, Z. A review on mechanical exfoliation for the scalable production of graphene. **J. Mater. Chem. A**, The Royal Society of Chemistry, v. 3, p. 11700–11715, 2015. Disponível em: <<http://dx.doi.org/10.1039/C5TA00252D>>.
- YUGE, K. Phase stability of boron carbon nitride in a heterographene structure: A first-principles study. **Phys. Rev. B**, American Physical Society, v. 79, p. 144109, Apr 2009. Disponível em: <<http://link.aps.org/doi/10.1103/PhysRevB.79.144109>>.

ZHANG, J.; ZHAO, X. S. Conducting polymers directly coated on reduced graphene oxide sheets as high-performance supercapacitor electrodes. **The Journal of Physical Chemistry C**, v. 116, n. 9, p. 5420–5426, 2012. Disponível em: <<http://dx.doi.org/10.1021/jp211474e>>.

ZHANG, M.; WU, J.; ZHU, Y.; DUMCENCO, D. O.; HONG, J.; MAO, N.; DENG, S.; CHEN, Y.; YANG, Y.; JIN, C.; CHAKI, S. H.; HUANG, Y.-S.; ZHANG, J.; XIE, L. Two-dimensional molybdenum tungsten diselenide alloys: Photoluminescence, Raman scattering, and electrical transport. **ACS Nano**, v. 8, n. 7, p. 7130–7137, 2014. PMID: 24884059. Disponível em: <<http://dx.doi.org/10.1021/nn5020566>>.

ZHANG, Z.; YANG, Y.; PENEV, E. S.; YAKOBSON, B. I. Elasticity, flexibility, and ideal strength of borophenes. **Advanced Functional Materials**, v. 27, n. 9, p. 1605059–n/a, 2017. ISSN 1616-3028. 1605059. Disponível em: <<http://dx.doi.org/10.1002/adfm.201605059>>.

ZHOU, H.; ZHAO, M.; ZHANG, X.; DONG, W.; WANG, X.; BU, H.; WANG, A. First-principles prediction of a new Dirac-fermion material: silicon germanide monolayer. **J. of Physics: Condensed Matter**, v. 25, p. 395501, 2013.

ZHOU, S.; BONGIORNO, A. Origin of the chemical and kinetic stability of graphene oxide. **Scientific Reports**, v. 3, p. 2484, 2013.

# Appendix A - GQCA scaling with cluster size

In this annex, we discuss the representation of atomic geometries, symmetry operations and the problem of determining a reasonable supercell size for a disordered system cluster expansion using a GQCA statistical approach.

As described in chapters 3 and 4, the atomic sites of substitutional alloys can be numbered and each supercell arrangement can be associated with an symbol array, e.g. AABBBBBB in chapter 3. This representation was generalized for functionalized sheets and adsorption sites, as demonstrated to graphene oxide in chapter 5. Let  $P$  be the number of possibilities for each atomic site in a substitutional alloy, which must correspond to the number of symbols in the array representation of atomic geometries. In general, when there is no constraint to the atomic arrangements, the total number of possible configurations is given by  $P^{N_s}$ , where  $N_s$  is the number of sites in the supercell. Considering a  $N \times N$  supercell to perform the cluster expansion and a unit cell with  $k$  atoms, we have  $N_s = kN^2$ .

Each cluster configuration is associated with a periodic system generated by its periodic in-plane repetition. A set of physical properties  $P_j$  are calculated for each generated periodic system and associated with the respective cluster configuration. Atomic geometries that generate the same periodic systems belong to the same equivalence symmetry class  $j$ . The number of atomic arrangements that belongs to cluster class  $j$  is given by its degeneracy  $g_j$ . Since every configuration must belong to one, and only one, symmetry class, we know that

$$\sum_{j=1}^J g_j = P^{N_s}. \quad (\text{A.1})$$

The symmetry operations of crystalline systems may be algebraically represented as groups (WATARI, 2009). Crystalline systems present both translational and point symmetries, which must belong to one of 230 different space group possibilities for bulk materials (WATARI, 2009). When a symmetry operation  $T$  is applied on a cluster atomic geometry, a permutation  $\sigma_T$  is applied to its associated array. The number of cluster space

symmetry operations of a  $N \times N$  supercell is given by the product of the  $N^2$  possible Bravais vectors translations by the number of possible point symmetry operations. The maximum value of cluster class degeneracy is  $g_j^{max} \propto N^2 \propto N_s$ , considering a particular case where every symmetry class results in a distinct cluster configuration. Therefore, the number of configuration classes  $J$  scales faster than  $O(P^{N_s}/N_s)$ . Considering that the computer time demanded for each DFT calculation scales with  $N_s^3$ , one observes that the increase of computational cost demanded by GQCA statistical approach scales as  $O(N_s^2 \times P^{N_s})$ .

In order to illustrate this exponential scaling, we discuss the sensibility of the number of symmetry cluster classes with respect to  $N$  and  $P$ . We start our study from the 2x2 supercell of a honeycomb structure, considered in chapter 3 and depicted in Fig. 3.1. In our work we considered binary alloy, which implies  $P = 2$ . The correspondent number of equivalence cluster classes is  $J_{bin} = 22$ , which is an organization of initial  $2^8 = 256$ . We evaluated the number of cluster classes considering ternary alloys ( $P=3$ ), the set of  $3^8 = 6561$  configurations can be organized into 267 configuration classes. In this case, no significant enhancement of the computational cost for each calculation is expected and an extension to binary to ternary IV-A group honeycomb alloys is still feasible.

On the other hand, the number of configuration exhibits a dramatic dependence on the cluster size. As an example, we consider how the number of cluster configurations scales from a 2x2 honeycomb supercell ( $N_s = 8$ ) to a 3x3 supercell ( $N_s = 18$ ) for a binary alloy. The number of possible cluster configurations is given by  $2^{18} = 262144$ , three orders of magnitude larger than the 2x2 supercell case. Based on the described scaling of  $O(P^{N_s}/N_s)$ , we estimate a number of 10.000 cluster classes for a 3x3 honeycomb supercell. Considering that each individual 3x3 supercell calculation takes about 8 more times than a 2x2 similar calculation, this cluster size change affects the GQCA time consumption by 3 orders of magnitude at least.

We restricted ourselves in this work to 2x2 supercells, exploring different materials, atomic geometry constraints, and the generalization of this framework to atomic sheets functionalizations. As demonstrated, this cluster size provides dozens (hundreds) of configurations for binary (ternary) alloys, providing rich statistics with a reasonable computational cost.

# Appendix B - Grand Canonical Quasi Chemical Approximation (Grand-GQCA)

In a functionalization process of a 2D atomic sheet, one can say that our system of interest is exchanging not only energy but also matter with the environment. The adsorption or release of functional groups are determined by the difference between chemical potential parameters  $\mu$  from the system and the environment. These processes can be understood by considering grand canonical ensembles.

In an analogous approach as the cluster expansion of the standard GQCA formalism, the system equilibrium state can be determined at a temperature  $T$  and a chemical potential  $\mu$  by minimizing the Grand potential

$$\Phi_G = U - TS - \mu_\alpha N_\alpha, \quad (\text{B.1})$$

instead of the Helmholtz free energy, where  $N_\alpha$  is the number of atoms/groups adsorbed in the system. Consider a cluster expansion of the disordered system, as an ensemble of  $M$  statistically and energetically independent clusters, that belong to one of  $J$  symmetry classes, analogously to the standard GQCA approach.

Let  $\{x_j\}$  be the distribution of the occurrence probability among the possible  $J$  configuration classes. Since the quantity of matter is not fixed anymore, the only constraint to this probability distribution is the normalization of total probability given by equation 2.71.

For each cluster class  $j$ , one must determine the internal energy per cluster  $E_j$ , the number  $n_{\alpha,j}$  of adsorbed  $\alpha$  groups per cluster and configuration degeneracy  $g_j$ . The expected value of thermodynamic properties  $U$ ,  $S$  and  $N$  can be written as a function of

probability distribution  $\{x_j\}$  as

$$U = M \sum_{j=1}^J x_j E_j, \quad (\text{B.2})$$

$$S = M k_b \sum_{j=1}^J x_j (\ln g_j - \ln x_j), \quad (\text{B.3})$$

and

$$N_\alpha = M \sum_{j=1}^J x_j n_{\alpha,j}. \quad (\text{B.4})$$

Since these three thermodynamical quantities can be calculated in terms of the occurrence probability distribution  $x_j$ , we can determine the equilibrium state of a grand-canonical ensemble by a constrained minimization of  $\Phi_G$  with respect to probability distribution  $x_j$  among the  $J$  cluster classes. The formulation of this minimization as a Lagrange multiplier problem leads to the equation

$$\frac{\partial}{\partial x_j} \left[ \sum_{j=1}^J x_j E_j - k_b T \sum_{j=1}^J x_j (\ln g_j - \ln x_j) - \mu_\alpha \sum_{j=1}^J x_j n_{\alpha,j} - \lambda \left( \sum_{j=1}^J x_j - 1 \right) \right] = 0, \quad (\text{B.5})$$

which can be developed, obtaining the following result for the probability distribution among the clusters

$$x_j = \frac{g_j \exp[-\beta(E_j - \mu_\alpha n_{\alpha,j})]}{\sum_{i=1}^J g_i \exp[-\beta(E_i - \mu_\alpha n_{\alpha,i})]}. \quad (\text{B.6})$$

This result can be easily generalized for more than one possible adsorptive groups by considering the Einstein sum notation on  $\alpha$  index.

# Annex A - Published works

- I. Guilhon, L. K. Teles, M. Marques, R. R. Pela and F. Bechstedt. Influence of structure and thermodynamic stability on electronic properties of two-dimensional SiC, SiGe, and GeC alloys. **Physical Review B** **92**, 075435 (2015).
- I. Guilhon, F. Bechstedt, M. Marques and L. K. Teles. Optical absorbance and band gap engineering of  $(\text{BN})_{1-x}(\text{C}_2)_x$  2D alloy: phase separation and composition fluctuation effects. **Phys. Rev. B** **95**, 035407 (2017).
- I. Guilhon, F. Bechstedt, Silvana Botti, M. Marques and L. K. Teles. Thermodynamic, electronic, and optical properties of graphene oxide: A statistical ab initio approach. **Phys. Rev. B** **95**, 245427 (2017).
- I. Guilhon, F. Bechstedt, Silvana Botti, M. Marques and L. K. Teles. Chemically tunable properties of graphene covered simultaneously with hydroxyl and epoxy groups. **Accepted by Journal of Physical Chemistry C**.
- I. Guilhon, D. S. Koda, M. Marques and L. K. Teles. A new perspective for approximate quasiparticle correction for 2D materials energy gap calculations. **To be submitted**.

# Annex B - Participation in scientific congresses and conferences

- I.G.M. Rocha, L. K. Teles, A. J. Chaves, R.R. Pelá, M. Marques and F. Bechstedt. Structural, thermodynamic and electronic properties of 2D alloys (Poster presentation), **XXXVIII Encontro Nacional de Física da Matéria Condensada**, 24-29 May 2015, in Foz do Iguaçu, Brazil.
- I.G.M. Rocha, L. K. Teles, R.R. Pelá, M. Marques and F. Bechstedt. Application of Generalized Quasichemical Approximation on 2D alloys (Talk), **XXIV International Materials Research Congress**, 16-20 August 2015, in Cancun, Mexico.
- Ivan Guilhon, Friedhelm Bechstedt, Ronaldo Rodrigues Pela, Marcelo Marques and Lara Kühl Teles. Structural, thermodynamic and electronic properties of two-dimensional SiC, SiGe, and GeC alloys (Talk given by Ronaldo Rodrigues Pelá), **80th Annual Meeting of the DPG and Spring Meeting**, 6-11 March 2016, in Regensburg, Germany.
- Lara Kühl Teles F. Bechstedt, M. Marques, I. Guilhon, D.S. Koda, R. R. Pela and F. Matusalém, Deposition, alloying and stacking of 2D honeycomb materials: a view from first principles (Invited talk given by Lara Kühl Teles), **ICSFS 18: International Conference on Solid Films and Surfaces**, August 28 - September 02 2016, in Chemnitz, Germany.
- I. Guilhon, M. Marques, L. K. Teles, F. Bechstedt, J. Furthmueller, and S. Botti, Optical properties of 2D alloys:  $(\text{BN})_{1-x}(\text{C}_2)_x$  (Talk), **Deutsche Physikalische Gesellschaft Frühjahrstagung**, 19-24 March 2017, in Dresden, Germany.
- I. Guilhon, M. Marques, L. K. Teles, F. Bechstedt, and S. Botti, Thermodynamic stability, electronic, and optical properties of graphene oxide: dependence on oxidation level (Poster), **Deutsche Physikalische Gesellschaft Frühjahrstagung**, 19-24 March 2017, in Dresden, Germany.

## ANNEX B. PARTICIPATION IN SCIENTIFIC CONGRESSES AND CONFERENCES

---

- I. Guilhon, F. Bechstedt, J. Furthmueller, S. Botti, M. Marques, and L. K. Teles, Optical properties of  $(\text{BN})_{1-x}(\text{C}_2)_x$  2D alloys (Talk), **14th ETSF Young Researchers' Meeting**, 5-9 June 2017, in Tarragona, Spain.
- I. Guilhon, F. Bechstedt, J. Furthmueller, S. Botti, M. Marques, and L. K. Teles, Optical properties of  $(\text{BN})_{1-x}(\text{C}_2)_x$  2D alloys (Poster presented by Friedhelm Bechstedt), **OSI-12: Optics of Surfaces and Interfaces**, 25-30 June 2017, in Dublin, Ireland.

## FOLHA DE REGISTRO DO DOCUMENTO

1. CLASSIFICAÇÃO/TIPO  TD	2. DATA  27 de novembro de 2017	3. REGISTRO N°  DCTA/ITA/TD-036/2017	4. N° DE PÁGINAS  147
5. TÍTULO E SUBTÍTULO:  Thermodynamical, electronic, and optical properties of 2D hexagonal disordered systems.			
6. AUTOR(ES):  <b>Ivan Guilhon Mitoso Rocha</b>			
7. INSTITUIÇÃO(ÕES)/ÓRGÃO(S) INTERNO(S)/DIVISÃO(ÕES):  Instituto Tecnológico de Aeronáutica – ITA			
8. PALAVRAS-CHAVE SUGERIDAS PELO AUTOR:  Teoria do Funcional da Densidade; Semicondutores; Estruturas bidimensionais, Física.			
9. PALAVRAS-CHAVE RESULTANTES DE INDEXAÇÃO:  Teoria do Funcional da Densidade; Semicondutores; Estruturas bidimensionais, Grafeno; Física.			
10. APRESENTAÇÃO: <span style="float: right;"><input checked="" type="checkbox"/> Nacional    <input type="checkbox"/> Internacional</span>  ITA, São José dos Campos. Curso de Doutorado. Programa de Pós-Graduação em Física. Área de Física Atômica e Molecular. Orientadora: Lara Kühnl Teles. Defesa em 20/11/2017. Publicada em 2017.			
11. RESUMO:  O estudo de materiais bidimensionais (2D) tem atraído grande atenção tanto da academia como da indústria. Nos últimos anos, a comunidade científica investigou diversos materiais 2D, entre os quais podemos destacar o grupo de materiais semelhantes ao grafeno compostos por elementos da família IV-A, como siliceno e germaneno, ou estruturas de favo de mel feitas de átomos que pertencem a famílias III e V-A, como o nitreto de boro hexagonal, ou mesmo os dicalcogenetos de metais de transição. Uma grande diversidade de comportamentos eletrônicos pode ser observada nesses materiais e novos dispositivos baseados neles encontram-se em fase de desenvolvimento. Pode-se produzir materiais com propriedades ajustadas para otimizar o desempenho de novos dispositivos. As ligas semicondutoras tridimensionais (3D) foram amplamente aplicadas nesse sentido como forma de obter <i>bandgaps</i> de energia ajustáveis, o que é conhecido como engenharia de bandgap. Da mesma forma, o uso de ligas de materiais 2D poderia aumentar o potencial de aplicações destes materiais, oferecendo a possibilidade de modulação de suas propriedades eletrônicas. Contudo, sob certas condições as ligas podem sofrer efeitos de separação de fase, levando a diferentes propriedades eletrônicas e ópticas. Dessa forma, o estudo de ligas semicondutoras 2D e de sua estabilidade termodinâmica é de grande valia. Neste trabalho, realizamos importantes estudos pioneiros sobre as propriedades estruturais, eletrônicas, ópticas e termodinâmicas das ligas binárias com base em elementos da família IV-A, bem como da liga feita de grafeno e nitreto de boro hexagonal. Exploramos também a possibilidade de ajuste das propriedades de materiais 2D através de funcionalização parcial da folha de grafeno com grupos adsorventes, como no caso do óxido de grafeno. Para realizar essas investigações, combinamos os cálculos <i>ab initio</i> baseados na teoria funcional da densidade com uma abordagem estatística baseada em uma expansão de clusters, conhecida como aproximação quase-química generalizada (GQCA, do inglês <i>Generalized Quasi-Chemical Approximation</i> ), para levar em conta a desordem estrutural e química do sistema. Propomos ainda um método de cálculo da entropia que não requer argumentos combinatórios e permite que a aplicação da GQCA para camadas atômicas funcionalizadas. O comportamento das propriedades físicas dos materiais estudados, tais como <i>gaps</i> de energia, é descrito como uma função de suas composições químicas médias e das condições de crescimento. Quando disponível, comparamos as previsões do nosso modelo com os resultados experimentais disponíveis. Diferentes condições de estabilidade termodinâmica foram verificadas em cada um desses sistemas e suas consequências para as suas respectivas propriedades físicas são entendidas à luz de efeitos de flutuação da composição e separação de fases.			
12. GRAU DE SIGILO:  <div style="text-align: center;"> <input checked="" type="checkbox"/> OSTENSIVO      <input type="checkbox"/> RESERVADO      <input type="checkbox"/> SECRETO         </div>			